NUMERICAL METHODS WITH REDUCED GRID DEPENDENCY FOR ENHANCED OIL RECOVERY

A DISSERTATION
SUBMITTED TO THE PROGRAM IN INSTITUTE FOR COMPUTATIONAL
AND MATHEMATICAL ENGINEERING
AND THE COMMITTEE ON GRADUATE STUDIES
OF STANFORD UNIVERSITY
IN PARTIAL FULFILLMENT OF THE REQUIREMENTS
FOR THE DEGREE OF
DOCTOR OF PHILOSOPHY

Jeremy Edward Kozdon
March 2009

I certify that I have read this dissertation and that, in my opinion, it is fully adequate in scope and quality as a dissertation for the degree of Doctor of Philosophy.

(Margot G. Gerritsen) Principal Adviser

I certify that I have read this dissertation and that, in my opinion, it is fully adequate in scope and quality as a dissertation for the degree of Doctor of Philosophy.

(Franklin M. Orr Jr.)

I certify that I have read this dissertation and that, in my opinion, it is fully adequate in scope and quality as a dissertation for the degree of Doctor of Philosophy.

(Gianluca Iaccarino)

I certify that I have read this dissertation and that, in my opinion, it is fully adequate in scope and quality as a dissertation for the degree of Doctor of Philosophy.

(Michael A. Christie)

Approved for the University Committee on Graduate Studies.

Abstract

In recent years there has been a resurgence of interest in enhanced oil recovery techniques, such as gas injection and in-situ combustion, as the need to access a wider array of hydrocarbon resources increases. Along with this, CO_2 sequestration as a carbon storage mechanism is increasingly important. These subsurface flow problems can be physically unstable at the scale modeled. This means that the displacement front will generally exhibit an unstable growth pattern known as viscous fingering. When simulating these processes, numerical errors which can be strongly correlated with the underlying computational grid can trigger, or at least bias, the formation of these fingers in ways not dictated by the underlying rock properties. This can give rise to the so-called grid orientation effect, where varying the orientations of the computational grid results in convergence to fundamentally different solutions.

The interest of this thesis is the development of numerical techniques that reduce grid dependency for these processes. We do this in a manner that draws upon fundamental numerical analysis techniques in conjunction with a physical intuition about the underlying governing equations. The governing equations for subsurface flow are of a mixed elliptic-hyperbolic character; here we focus on the hyperbolic portion but seek methods compatible with general elliptic discretizations and computational grid topologies.

Some aspects of the grid dependency can be traced back directly to the handling of the injection wells. Perturbation created early in time and near the injection wells propagate into the interior of the domain setting up an initial biasing for the simulation. We demonstrate that the handling of injection wells drastically affects the final result. We propose two methods, a well-sponge method and a local embedding technique, which extends the well region based on near-well models. Both of these methods drastically increases the similarity between the solutions on different computational grids.

The numerical method used in the interior region can also have a significant impact on the computed solution. For multidimensional (multi-D) problems the structure of the numerical diffusion tensor creates preferential flow directions. These preferential flow directions can be strongly coupled to the grid, especially when a 1-D method is applied dimension by dimension. This motivates the development of truly multi-D transport discretizations that incorporate local flow information into

the flux calculation. We develop a family of compact, upstream biased multi-D finite volume methods for 2-D simulation. The methods control the structure of the diffusion tensor and incorporate characteristic flow information through the use of a local coupling methodology based on interaction regions. The family of schemes is positive for linear equations and monotone for a class of scalar nonlinear equations.

Two multi-D schemes, tight multi-D upstream weighting and smooth multi-D upstream weighting, are proposed and analyzed. Since transverse diffusion largely controls finger formation in linear problems, a third scheme is proposed called the Flat Scheme, which has constant transverse diffusion. All the multi-D methods are appropriate for both explicit and implicit time stepping. The methods are applied to both miscible and immiscible displacement problems and significantly reduce biasing due to the grid as compared with the commonly used single point upstream weighting method.

Acknowledgements

Though only my name is on the cover of this dissertation, it is certainly not the result of my efforts alone. There have been many who have motivated and helped me along the way.

I am grateful to my advisor Margot Gerritsen for putting up with me the past few years. She has been a great colleague and friend. (How many other advisors would put up their student's wedding party for three days?) A special thanks is also due to Bradley Mallison for being a great resource and mentor as well as serving on my oral examination committee. Additionally, I am thankful to Michael Christie for his encouragement and help in the initial stages of my research. As a reader Mike helped make the introduction and conclusion sections to my thesis a hundred times better. I am indebted to Lynn Orr and Gianluca Iaccarino for taking the time to serve on my reading committee and Jesse Lawrence for chairing my oral committee.

I will miss my fellow students of ICME, especially those who have had the misfortune of sharing an office with me (David Gleich, Paul Constantine, Michael Atkinson). I could not have asked for a better group of students to spend five years with. I almost certainly would not have finished without the support of the ICME student services advisor Indira Choudhury who continually put up with me turning in late forms and forgetting to sign up for classes.

My life would not be nearly as nice without my many non-academic friends from the Reformed University Fellowship and Grace Presbyterian Church. They helped to maintain my sanity when graduate work got me down. Special thanks go to Timothy Butler, David Jones, Jason Greene, Dirk Veenema, and the rest of the crew who raised many a drink with me.

Finally I must thank my family. My parents have loved me so dearly and always supported me as I have wandered through this world trying to figure out what to do. Without them my graduate work would never have begun. Last, and certainly not least, I thank my wife Jennifer who has loved me and put up with me as I have put together my dissertation. She has also probably read my thesis more closely than anyone, including myself, and for that I am very very grateful. Without her I would be a much more morose and boring person.

This work has been supported by the SUPRI-C Affiliates and DOE grant number DE-FC26-04NT15530. Much of this work was also completed while I was interning in the reservoir simulation research group at Chevron Energy Technology, where I spent three summers.

Contents

List of Tables

List of Figures

Chapter 1

Introduction

Computational tools and techniques are playing an increasingly important role in modern reservoir management. This is due in part to increased computational resources which have allowed simulation to move toward full field compositional models. Another contributing factor to this increased usage is the desire to access a wider array of hydrocarbon resources, which may be more physically and/or economically costly to produce. Some of these resources are more remote resources, such as deep sea resources, whereas others may not be producible by primary and secondary recovery techniques, such as water injection. This leads to an increased interest in using enhanced oil recovery (EOR) processes, such as gas injection and in-situ combustion, which increase the mobility of the less mobile oil allowing them to be more efficiently produced (Lake, 1989; Sarathi, 1999).

These processes face many computational challenges: the governing equations are tightly coupled and highly nonlinear, the physics happens at widely varying length scales, and the rock properties (porosity and permeability) can vary by several orders of magnitude at length scales that are short with respect to the simulation scale (Gerritsen and Durlofsky, 2005). As more physics is added to the problem, the governing equations can exhibit structures not found in traditional computational fluid dynamics problems. For instance, fully compositional models result in a weakly hyperbolic system of governing equations (**?**) requiring special computational techniques (Krishnamurthy, 2008).

Many EOR methods exhibit a physical instability at the modelling scale (Tan and Homsy, 1997; Riaz and Meiburg, 2004). This instability arises primarily in adverse mobility displacements, that is, when the viscosity of the injected fluid is much lower than the viscosity of the resident fluid. One of the challenges in simulating these displacements is that numerical errors can trigger, or at least bias the triggering, of these fluid instabilities in ways not dictated by the underlying rock properties (permeability and porosity). This can give rise to the so-called grid orientation effect (GOE) (Todd et al., 1972), where different orientations of the computational grid result in convergence to fundamentally different solutions. An example of this is given in Figure 1.1. Here we have used a two component miscible model, presented in chapter 2, with a standard two-point flux

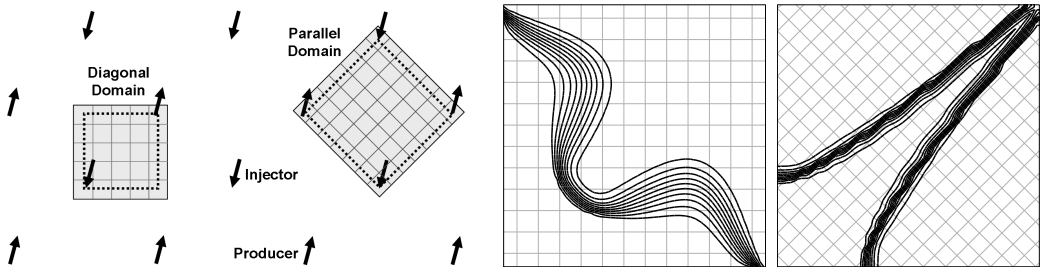

(a) Periodically repeating 5 spot pattern with two quarter five-spot domains

(b) Diagonal grid solution front

(c) Parallel grid solution front

Figure 1.1: A miscible adverse mobility ratio, $M = 30$, quarter five-spot displacement simulated on a 50×50 diagonal grid and 71×71 parallel grid. In both solution profiles, the injector is located in the lower left corner and the producer in the upper right corner.

discretization for the pressure equation (a five point finite difference stencil in 2-D) and dimensional, or donor cell, upwinding for transport (a hyperbolic equation). For the quarter five-spot pattern there are two principal axes of symmetry which allow different alignments of the simulation grid with respect to the mean flow direction (between the injector and producer). The solution on the two grids converge toward fundamentally different results as the grid resolution is increased even though consistent and stable discretizations are used. Since the reservoir knows nothing about the simulation grid, this lack of convergence to the same answer indicates that there is something more complex occurring.

Since the work of (Todd et al., 1972) there has been a significant research efforts to understand, reduce, and remove GOE. Fundamentally GOE arises because of an interaction of the above mentioned physical instability with numerical errors. These numerical errors, which can arise from a variety of sources, trigger unstable modes in the solution, as is demonstrated throughout this thesis. Amongst the most important errors contributing to GOE are the errors arising from the numerical methods used for transport. Generally speaking work to alleviate GOE has fallen into several broad categories: adaptation of the stencil to more fully capture the directionality of the flow, use higher order methods along with a rotationally invariant fluid stabilizing diffusion term, and modification of the grid to remove apparently preferred flow directions. These different approaches are more fully review below.

1.1 Related Directions within the Industry

Of course, there are many other types of errors and uncertainties that must be considered in any simulation project. Though much of this work is outside of the scope of this thesis it forms the wider

context of developing more robust and accurate methods for assessing reservoir performance, so we briefly review some related work here.

One of the first tasks in reservoir simulation is the building of a geocellular model. Unfortunately there tends to be very little hard data, core samples and well data, which by its very nature sparse (or non-existent in the initial reservoir characterization stage). Hence to a large extent the geological properties must be inferred from softer information, such as seismic data, analogous outcrops, and previous experience. The task of building these geological models is known as geostatistics (Caers, 2005). Various spatial statistic techniques, for instance Kriging, must be used to estimate the reservoir properties. Since many different reservoirs may match the known hard and soft data multiple realizations must be developed and evaluated.

Detailed geological models can have on the order of $10^7 - 10^8$ cells. Models with this level of detail cannot be simulated within a reasonable time frame, hours to days, so these models must be coarsened to $10^5 - 10^6$ cells depending on the type and detail of model needed. Furthermore, as mentioned above, many realizations of the model must be run to properly account for the variability in the problem, so even when massively parallel computers are available it may be more beneficial to run a large number realizations as opposed to a few high fidelity models. There are two broad classes of coarsening techniques used for reservoir simulation: upscaling (Wen and Gmez-Hernndez, 1996; Christie, 1996; Renard and de Marsily, 1997; Farmer, 2002) and multiscale methods (Hou and Wu, 1997; Chen and Hou, 2003; Aarnes, 2004). In upscaling, coarse-scale governing equations are prescribed based on fine-scale equations via a technique such as homogenization or volume averaging. In practice the upscaled equations are often taken to be the same form as the fine-scale except with updated parameters (absolute permeability, porosity, etc.). In this methodology both transport and flow/pressure are solved for on the coarse-scale. In multi-scale methods the coarse-scale equations are not expressed analytically but rather numerically as the fine-scale information is used throughout the simulation in solving the equations. With multiscale methods the pressure is solved on the coarse-scale whereas transport tends to be solved on the fine-scale, but this is not necessary.

Once the equations and model are developed comes the task of discretization. To a large degree the industry standard for the transport, or hyperbolic, discretization is a method called single point upstream weighting, which is closely related to donor cell upwinding (Aziz and Settari, 1979). More general techniques will be developed later in this thesis (see chapter 4). For the pressure equation there has been significant work within the literature to develop multi-point flux approximations (Aavatsmark, 2002; Edwards and Rogers, 1998). A two-point flux approximation defines the pressure difference, and therefore the velocity, across a grid face using the two neighboring cells to a face whereas multi-point methods take into consideration several neighborings cells depending on the local rock properties (permeability tensor) as well as the computational grid. When the simulation model involves tensor permeabilities and/or non-orthogonal grids these multi-point methods may

be necessary for a consistent pressure discretization. Closely related to this are multipoint transmissibility upscaling methods which take into account the stencil selection while upscaling from the geological model (Lambers et al., 2009).

The goal of reservoir simulation is not to run simulations, but to develop knowledge and understanding of the system. Hence the simulations must be matched to data, for instance production data and well log data; this is known as history matching. The hope is that a history matched model says something about future performance of the reservoir. Unfortunately, as alluded to above, we can never hope to full characterize the reservoir so uncertainty quantification is needed (Christie et al., 2005, 2006). Generally speaking, in the field of uncertainty quantification there are two main types of uncertainty: reducible (epistemic) and irreducible (aleatory) uncertainty. Irreducible uncertainty has to do with natural variability within a model, that is, uncertainty that even sampling cannot remove. Reducible uncertain has to do with parameters that have a single value but that is not known but that could (in theory) be measured, such as porosity, permeability, fluid viscosity, etc.. Of course in many applications measurement is not possible, so methods must be developed to handle this. One methodology of handling these types of uncertainties is by sampling from the probability distribution for each of the variables using some methodology, such as Monte Carlo techniques. Of course the parameter space that must be sampled from is of quite high dimension (tens to hundreds of parameters) so stochastic sampling algorithms can be used to more efficiently explore the space. Once this is done Bayesian techniques can be used to infer confidence estimates on the forecasts of the simulations. Hence when uncertainty is properly accounted for we are not searching for a single model which fits the observed data but a ensemble of models with varying levels of confidence.

In the above uncertainty was assumed to arise from unknown physical parameters and reservoir characterization. There is another contributing factor to uncertainty — modelling errors (O'Sullivan and Christie, 2005, 2006). Modeling error can arise from a variety of places including using simplified physics and numerical discretization errors. In order to form more reliable estimates on the confidence of our forecast these errors need to be accounted for during history matching process. To do this the errors must be approximated or modelled in some way, such as by comparing coarse grid solutions to fine grid or analytic solutions. One of the challenges for unstable flow problems is that fine grid solutions may be worse than coarse grid solutions. This is due to the fact that numerical errors trigger the underlying physical instability, as discussed above. This makes model calibration and the development of suitable error models more challenging.

1.2 Past Approaches to Alleviate Grid Dependency Effects

Past strategies suggested in the literature to alleviate the GOE and other grid dependency effects generally fit into one or more of the following three categories:

1. Adaptation of the solution method for the pressure equation that determines the fluid flow. Most approaches are based on extending the discretization stencil from the standard five points to nine points in 2D (7 to 27 points in 3D).

2. Improvement of the transport calculation through the use of higher order numerical methods, such as Essentially Non-Oscillatory (ENO) or Total-Variation Diminishing (TVD) schemes, which diminish numerical diffusion, or by design of rotationally invariant numerical diffusion terms that are added to existing transport schemes.

3. Modification of the grid so that there is no immediately obvious preferred direction of transport.

The paper by Todd et al. (1972) was the first to suggest using modified stencils. Their approach was to replace the standard single point upstream (SPU) discretization of transmissibility with an upstream discretization involving two points. A number of nine-point schemes were introduced for Cartesian grids by, amongst others, Yanosik and McCracken (1979), Shiralkar (1990) and Potempa (1983). These approaches are largely based on the concept of taking a linear combination of the five point nearest neighbor stencil and the five point next-nearest (diagonal) neighboring stencil in order to allow flow "between a block and the four blocks that are adjacent to its boundaries... as well as flow between the block and the four blocks located at its corners" (Yanosik and McCracken, 1979). Though approach showed promise the methods do not explicitly take into account local flow information or the grid dependent structure of a error terms. Shubin and Bell (1984) suggested using a first order numerical diffusion term that reduces the grid dependency of the second order central discretization of the transport equations. The formulation was motivated by analysis of the modified equations. We discuss their scheme in further detail in chapter 3. The ideas of Shubin and Bell form some of the motivation for the transport methods developed in chapter 4, but this discretization rely heavily on a tightly coupled transport and pressure discretization. This means that the discretization is not applicable for use with MPFA methods. The method is also not monotone, which is a desirable property for first order methods.

The use of higher order discretization methods, such as Total Variation Diminishing (TVD) or Essentially Non-Oscillatory (ENO) schemes, has been suggested by various authors, including Chen et al. (1993) and Wolcott et al. (1996). These schemes allow physically stabilizing diffusion models to be applied at reasonable grid densities due to the faster decay of higher order error terms under grid refinement. Unfortunately, a large amount of diffusion is required to stabilize these problems which can drastically degrade the quality of the simulation. Furthermore, higher order methods reduce to first order methods near discontinuities resulting in the same grid dependent first order error terms resulting in GOE. Part of the challenge is that is it very difficult to construct truly multidimensional higher order methods, hence higher order methods tend to be applied along each dimension of the grid. Though this has been quite successful in some applications, it ignores the cross derivative terms (LeVeque, 2003, 1997) so there remains a first order error which can trigger GOE.

Furthermore, higher order methods require special treatment of the wells, regions where there wide stencils cannot be formed, and as we show later in thesis well errors are important when considering GOE. Therefore, though we believe that higher order methods are beneficial and should continue to be explored for use in reservoir engineering, there is also a need to develop less grid sensitive first order discretization on top of which the higher order methods can be build. It should also be noted that through there have been some work on higher order schemes for reservoir simulation (Blunt and Rubin, 1990; Edwards, 2004; Jessen et al., 2008; Chen et al., 1993; Wolcott et al., 1996), by in large the industry standard approach is to use the first order SPU method (Aziz and Settari, 1979).

Another method for alleviating GOE is the adaptation of the underlying computational grid. This approach was first proposed by Robertson and Woo (1978) who suggested using an orthogonal curvilinear grid based on streamlines. Other gridding methods have been proposed with the express purpose of reducing GOE such as Pruess and Bodvarsson (1983) who suggested using (nearly) regular hexahedral grids and Heinemann et al. (1991) who suggested using unstructured perpendicular bisection (Voronoi) grids. Currently, non-Cartesian, whether structured or unstructured, grids are often suggested for handling GOE in the literature since they can seemingly reduce directionally preferred transport directions. A large part of this is due to the fact that the results suffer excessive smoothing due to diffusion, as can be observed in the simulated results of these papers. Unstructured grids can in themselves introduce grid dependency when the standard SPU discretization is used as in demonstrated in Lamine and Edwards (2008).

One of the guiding principles in our work is that we do not wish to be required to select our grids to alleviate grid orientation. The primary impetus for this principle is that a requirement to mitigate a numerical artifact through choice of grid alignment immediately makes our results strongly process dependent. For example, a change of wells will lead to a change of orientation of principal flow paths with respect to the grid and an unknown amount of potential GOE. Also, we prefer not to be locked in to a certain choice of grid since apart from GOE there may be other, and conflicting, considerations in choosing a grid that can significantly affect the quality of numerical solutions, such as upscaling methodology, handling of faults, or pressure equation discretization. For instance, is is difficult to do a large number of simulation runs where the grid must adapt to a physical feature, such as the location and geometry of a fault in an uncertainty quantification procedure, with highly unstructured grids.

1.3 Goals of the Thesis

In this thesis we develop methods primarily motivated by the goal of reducing grid dependence. We want to do this in a manner which keeps in mind the over overarching directions within the industry as briefly outlined above. Namely we want to understand the nature of the errors that are important for grid orientation so that they can be taken into account when developing error and

uncertainty quantification strategies. Another reason for the development of the methods in this thesis is that given a set of parameter ranges for the physical properties, e.g. porosity, fluid viscosity, permeability, fault locations, etc., it may be impossible to history match a given reservoir to the well data because the numerical errors are so strongly correlated with the underlying grid. As the industry has been moving towards more robust and accurate discretizations for the pressure equation the methods proposed in this work, which primarily concern the hyperbolic transport discretization, are not developed assuming a specific form of the pressure discretization. Finally, we want methods which are are at least as stable as the conventional techniques and which are applicable within range of simulation frameworks and methodologies. We seek to do this in two distinct but complementary ways: local near-well solution forcing and truly multi-D transport discretizations.

As is shown in Chapter 3, early-time and near-well perturbations contribute significantly to the grid depend solution behavior seen in Figure 1.1. Hence this motivates the development of techniques with which to force a near-well solution, resulting from either fine-scale simulation or an assume analytic form of the solution. Of course, in this forcing procedure we must be careful not to introduce perturbations into the solution which will results spurious simulation results. We therefore propose two forcing procedures to do this. The first is a well-sponge methodology inspired by sponge methods which have been proposed for enforcing boundary conditions in computational acoustics (Bodony, 2006). This is essentially a penalty method where deviations in the solution from the assumed near-well solution are penalized. The well-sponge method is not conservative, so we also propose a local embedding technique, which we call LETIS. This method motivated by immersed boundary methods (Mittal and Iaccarino, 2005), and in this strategy fluxes, as opposed to cell averages, are forced which ensures conservation.

Motivated by the methods proposed by Shubin and Bell (1984), Helzel et al. (2005), and Deconinck and Koren (1997) we also develop a family of multidimensional transport discretizations for 2-D problems. Incorporating local flow information into the computational stencil allows us to control the structure of the first order error term, therefore making the structure of the underlying computational grid less apparent. The family of schemes we develop is similar to a family proposed for constant velocity scalar advection by Roe and Sidilkover (1992) as well as Van Ransbeeck and Hirsch (1997). Unlike these methods, our methods are provably monotone for scalar advection in rough velocity fields as well as for a class of nonlinear equations. Furthermore, the developed monotone methods can be used even when in the presence of gravitational forces, something that has not been explored in the any of the above mentioned multi-D methods (see section 1.2. We also propose a relaxed volume methodology for multi-phase simulation. This methodology is not proposed to reduce grid dependence, but to increase the robustness of the simulated results as it results in provably physical discrete variables. Our methods are also applicable with general pressure discretizations and though Cartesian grids are used throughout this work the proofs as well as the framework assume nothing about the underlying grid topology.

1.4 Outline of the Thesis

In chapter 2, we present the governing equations used throughout this thesis. In general the flow is multicomponent, multi-phase but we will make the simplifying assumptions of two-component, two-phase flow without mass transfer between the phases. These simplification allow us to make rigorous numerical analysis statements while retaining the necessary physical instability. We also present a partially and fully miscible model which is used throughout this work along with the immiscible model.

In chapter 3, we discuss the near-well methods. It is first shown that near-well and early-time perturbations in the solution have a drastic effect on the solution front. We then propose two solution forcing methods, a well-sponge and LETIS, to force near-well solutions onto the computational grid in a manner which minimizes the introduction of perturbations into the solution. Shubin and Bell (1984) isotropic error transport method is also explained in this chapter.

Chapter 4 begins the multi-D transport section of the thesis. Analysis of a family of multidimensional finite difference schemes for constant, scalar advection is presented. These schemes are all first order, but using modified equations analysis are shown to all have different first order numerical diffusion tensors. We then develop a multidimensional, conservative finite volume framework for a class of nonlinear PDEs. Within this framework is the family of multi-D schemes as well as several other schemes — namely, a novel scheme with constant transverse diffusion, which we call the Flat Scheme, for scalar advection.

In chapter 5, we apply the multi-D transport methods to a miscible gas injection problem. We test the methods on two different domains, the previously mentioned quarter five-spot problem as well as a radial displacement for both homogeneous and heterogeneous permeability fields.

In chapter 6, we apply the multi-D transport methods to nonlinear problems. The two problems we consider are an immiscible water flood with and without gravity as well as partially miscible gas injection with gravity. To do this we develop a mass conservative, volume relaxed simulation framework. This framework results in physical masses and saturations even in the presence of numerical errors and inexact pressure solutions. This is important for general transport discretizations.

Directions for future work and general conclusions are presented in chapters 7 and 8, respectively.

Chapter 2

Governing Equations

Flow in porous media is governed by a set of coupled differential equations. At the pore scale, that is, the scale at which individual pores in the rock are resolved, the flow obeys the Navier-Stokes equations. Direct numerical simulation of the fluids at this scale is not practical for field scale simulation, so a set of empirical average equations are used. These equations attempt to track the average behavior of the fluid without resolving the complex physics happening at the pore scale. Note that Brinkman and Forchheimer extensions of Darcy's law are not relevant for reservoir simulation because we are not considering high porosity flow and do not have high velocities (the flow is creeping everywhere, even near the wells). These extensions are sometimes used for pore scale modelling, but not field scale modelling which we are considering here.

In this chapter we will outline the governing equations that are used in this work. We will also present the various assumptions that are used throughout the work which maintain the important physical behavior and mathematical structure needed but allow for more rigorous numerical analysis.

2.1 Multi-Phase, Multi-Component Flow Equations

In general, a porous media problem consists of n_c chemical components flowing together. We let c_i be the mass concentration of component i. The mass concentrations obey a conservation law of the form

$$\phi \frac{\partial c_i}{\partial t} + \nabla \cdot \boldsymbol{F}_i(c_1, c_2, \ldots, c_{n_c}) = q_i, \ i = 1, 2, \cdots, n_c \tag{2.1}$$

where, for each component i, $\boldsymbol{F}_i$ is the mass flux and q_i is the source/sink term (i.e. wells). The porosity of the medium is ϕ. These mass components flow together in n_p phases, where S_α is the saturation of phase α, that is, the volume fraction of the fluid in phase α. Since these are volume fractions, $\sum_{\alpha=1}^{n_p} S_\alpha = 1$. The fraction component i in phase α is $x_{i,\alpha}$, where $\sum_{\alpha=1}^{n_p} x_{i,\alpha} = 1$. If the

density of each phase is ρ_α, then the mass concentration of component i is

$$c_i = \sum_{\alpha=1}^{n_p} \rho_\alpha x_{i,\alpha} S_\alpha. \tag{2.2}$$

We assume that the average velocity of a fluid phase α in a porous media obeys the commonly used multi-phase extension of Darcy's law

$$\boldsymbol{u}_\alpha = -\frac{k_{r\alpha}}{\mu_\alpha} \boldsymbol{K} \nabla (p_\alpha - \rho_\alpha g h), \tag{2.3}$$

where p_α is the pressure of phase α, g the gravitational constant, h the height, $\boldsymbol{K}$ the absolute permeability tensor (a rock property which measures how easily fluid can flow in the rock), and μ_α the viscosity of phase α. Relative permeability, $k_{r,\alpha}$, is a dimensionless measure of how easily a phase can flow in the rock when other phases are present. The phase pressures are assumed to be related through capillary pressure relationships,

$$p_{c,\alpha,\beta} = p_\alpha - p_\beta.$$

The mass flux $\boldsymbol{F}_i$ can now be written in terms of the above defined quantities as (**?**)

$$\boldsymbol{F}_i = \sum_{\alpha=1}^{n_p} x_{i,\alpha} \rho_\alpha \boldsymbol{u}_\alpha. \tag{2.4}$$

Equations 2.1-2.4, along with thermodynamic phase equilibrium assumptions, govern the movement of fluids. We have omitted diffusive and dispersive effects from the governing equations because numerical errors will be larger than theses effects at the grid resolutions we will be using. For a discussion of the relevant physics and length scales of diffusion see Russell and Wheeler (1984).

2.2 Simplifying Assumptions

As discussed in chapter 1, the goal of this work is to develop numerical methods with reduced sensitivity to the computational grid. Though we could begin by developing methods for the full compositional problem, as the equations become more complex, the analysis of the methods becomes more challenging. Thus we instead introduce a set of simplifying assumptions which retains the essential physical behavior and fluid instabilities but allows for more rigorous statements about the numerical methods developed. In chapter 7 we will discuss some of the implications of removing these assumptions and ways that this can be explored in future work.

First, we assume that there are only two components — oil and gas (or water, depending on the context) $i = o, g$ — which are strictly aligned with two phases with the same names, $\alpha = o, g$. This

means that

$$x_{o,o} = 1, \qquad x_{o,g} = 0, \qquad x_{g,g} = 1, \qquad x_{g,o} = 0,$$

and thus $c_\alpha = \rho_\alpha S_\alpha$. Our governing equations, including the phase velocities, can now be written

$$\phi \frac{\partial c_\alpha}{\partial t} - \nabla \cdot \left(\rho_\alpha \frac{k_{r\alpha}}{\mu_\alpha} \boldsymbol{K} \nabla (p - \rho_\alpha g h) \right) = 0, \qquad \alpha = o, w, \tag{2.5}$$

where, for simplicity, we have neglected capillary effects so that the phases are all at the same pressure, that is, $p = p_o = p_g$. We focus exclusively on the limiting case of incompressible fluids so that the phase densities are constant in space and time. The viscosities are assumed to be functions of the saturations, $\mu_\alpha = \mu_\alpha(S_\alpha)$, with the property that when only phase α is present ($S_\alpha = 1$) then the viscosity is given by the single phase viscosity $\bar{\mu}_\alpha$, that is, $\mu_\alpha(1) = \bar{\mu}_\alpha$. The relative permeability functions are also assumed to be functions of the saturations, $k_{r\alpha} = k_{r\alpha}(S_\alpha)$, with the property that when phase α is not present $k_{r\alpha}(0) = 0$. In this work we will test our methods with Corey (1954) type relative permeabilities, where $k_{r\alpha} = S_\alpha^{a_\alpha}$ and a_α can be different for each phase.

2.3 Pressure Equation

A pressure equation can be derived from Equation 2.5, along with the above assumptions, by scaling by $1/\rho_\alpha$ and summing over both phases

$$\begin{aligned}
0 &= \sum_{\alpha=o,w} \frac{1}{\rho_\alpha} \left(\phi \frac{\partial c_\alpha}{\partial t} - \nabla \cdot \left(\rho_\alpha \frac{k_{r\alpha}(S_\alpha)}{\mu_\alpha(S_\alpha)} \boldsymbol{K} \nabla (p - \rho_\alpha g h) \right) \right) \\
&= \phi \frac{\partial (S_o + S_g)}{\partial t} - \sum_{\alpha=o,w} \left(\nabla \cdot \left(\frac{k_{r\alpha}}{\mu_\alpha} \boldsymbol{K} \nabla (p - \rho_\alpha g h) \right) \right) \\
&= \phi \frac{\partial 1}{\partial t} - \sum_{\alpha=o,w} \left(\nabla \cdot \left(\frac{k_{r\alpha}}{\mu_\alpha} \boldsymbol{K} \nabla (p - \rho_\alpha g h) \right) \right) \\
&= - \sum_{\alpha=o,w} \left(\nabla \cdot \left(\frac{k_{r\alpha}}{\mu_\alpha} \boldsymbol{K} \nabla (p - \rho_\alpha g h) \right) \right).
\end{aligned}$$

Putting these together gives the following hyperbolic-elliptic system of equations

$$- \sum_{\alpha=o,w} \left(\nabla \cdot \left(\lambda_\alpha \boldsymbol{K} \nabla (p - \rho_\alpha g h) \right) \right) = 0, \tag{2.6}$$

$$\phi \frac{\partial c_\alpha}{\partial t} - \nabla \cdot \left(\rho_\alpha \lambda_\alpha \boldsymbol{K} \nabla (p - \rho_\alpha g h) \right) = 0, \tag{2.7}$$

along with the closure relations

$$\begin{aligned} c_\alpha &= \rho_\alpha S_\alpha, & 1 &= S_g + S_o, \\ \mu_\alpha &= \mu_\alpha(S_\alpha), & k_{r\alpha} &= k_{r\alpha}(S_\alpha), \\ \lambda_\alpha &= \frac{k_{r\alpha}}{\mu_\alpha}, \end{aligned}$$

where λ_α is referred to as the mobility of phase α. We refer to this model as the nonlinear model throughout the thesis.

2.4 Fractional Flow Versus Darcy-Based Form

Equation 2.7 can also be written in terms of the total velocity. If we define total velocity as

$$u_T = -\sum_{\alpha=o,w} \left(\lambda_\alpha \boldsymbol{K} \nabla(p - \rho_\alpha g h)\right),$$

then Equation 2.7 can be written as

$$\phi \frac{\partial c_\alpha}{\partial t} + \nabla \cdot \left(\rho_\alpha f_\alpha \left(u_T - K \nabla \left(\left(\rho_\alpha - \rho_{\beta \neq \alpha}\right) g h\right) \lambda_{\beta \neq \alpha}\right)\right) = 0, \tag{2.8}$$

where the fractional flow function f_α is defined as

$$f_\alpha = \frac{\lambda_\alpha}{\lambda_o + \lambda_w}.$$

We refer to the transport equation written as Equation 2.7 as the Darcy form of the equation and when written as Equation 2.8 as the fractional flow form. For the methods developed in chapter 4 we will need our transport equations to be of the form

$$\frac{\partial c}{\partial t} + \nabla \cdot \left(\zeta(c) \begin{pmatrix} \sigma_x \\ \sigma_x \end{pmatrix}\right) = q(c), \tag{2.9}$$

where σ_x and σ_y are independent of c, or at least can be kept fixed during the transport solve. Hence the fluxes are linear in $\zeta(c)$. Both the Darcy and fractional flow forms can be written in this manner when there are no gravitational forces, but when gravitational effects are included this is not possible with the fractional flow formulation. To understand this, consider a vertical reservoir where the gravitational force acts in the y-direction and there is no gravitational force in the x-direction.

In Darcy form the transport equation becomes

$$C_{t,\alpha} + \nabla \cdot \left(\lambda_\alpha \begin{pmatrix} \frac{\partial}{\partial x}(p) \\ \frac{\partial}{\partial y}(p - \rho_\alpha g h) \end{pmatrix} \right) = q(c),$$

and in fractional flow form this would be

$$C_{t,\alpha} + \nabla \cdot \left(\rho_\alpha f_\alpha \begin{pmatrix} U_{T,1} \\ U_{T,2} - \gamma \end{pmatrix} \right) = q(c),$$

where $\gamma = K(\rho_\alpha - \rho_{\beta \neq \alpha}) g \frac{\partial h}{\partial y} \lambda_{\beta \neq \alpha}$. Since γ depends on C, through λ_β, the fractional flow form is not of the form of Equation 2.9 whereas the Darcy form is. In chapters 3 and 5 we will use the fractional flow form since we will be neglecting gravity and using a miscible model which will make the equations linear in concentration (see below). In chapter 6 we will use the Darcy form since we will consider gravitational effects as well as more general mobility functions.

2.5 (Partially) Miscible Model

An important model used in this work is the Todd and Longstaff (1972) model for partially miscible flow. In this model the relative permeabilities are linear in the saturations, $k_{r\alpha} = S_\alpha$, and the viscosities also depends on the saturations. The effective viscosity is

$$\mu_{e,\alpha} = \mu_\alpha^{1-\chi} \mu_m^\chi,$$
$$\mu_m = \left(\frac{S_g}{\mu_g^{1/4}} + \frac{S_o}{\mu_o^{1/4}} \right)^{-4},$$

where χ is a mixing parameter giving the level of miscibility and μ_α is the immiscible phase viscosity. When $\chi = 1$ the displacement is miscible, and we refer to it as the miscible model.

In chapters 3 and 5 we will use the miscible model without gravity written in the fractional flow form as

$$0 = -\nabla \cdot \frac{\boldsymbol{K}}{\mu_{e,g}(S_g)} \nabla p \equiv \nabla \cdot \boldsymbol{u}, \tag{2.10}$$

$$0 = \phi \frac{\partial c_g}{\partial t} + \nabla \cdot (c_g \boldsymbol{u}), \tag{2.11}$$

where the first equation is an incompressible flow constraint and the second a scalar advection equation.

In chapter 6 we will use the partially miscible model in Darcy form with Koval's (1963) value for

χ,

$$\chi = 1 - 4\frac{\ln(0.78 + 0.22M^{1/4})}{\ln(M^{1/4})}, \tag{2.12}$$

where $M = \mu_g/\mu_o$. One of the interesting features of this model is that the oil mobility function, $\lambda_o(S) = k_{ro}(S)/\mu_{e,o}(S)$, can have a stationary point, $\lambda_o'(S) = 0$, if $M > 625/256 \approx 2.44$ at

$$S_o = \frac{M^{1/4}}{5\left(M^{1/4} - 1\right)}.$$

For this region the gas mobility function is convex.

An important feature of this model is that it has a theoretical fluid instability. Hence perturbations in the displacement give rise to viscous fingering. It has been previously shown by Tan and Homsy (1997) that the strength of the instability is a function of both the mobility ratio and the amount of diffusion in the model. Riaz and Meiburg (2004) showed that if tensor diffusion is considered, the transverse, or crosswind, diffusion largely controls finger formation whereas longitudinal, or streamline, diffusion controls finger growth. The above mentioned work only considers physical diffusion models, but in this work we assume that the numerical diffusion is much larger than the physical diffusion so the structure of the numerical diffusion tensor will be an important consideration in future chapters.

2.6 Finite Volume Discretization

The methods developed in this dissertation largely deal with the hyperbolic transport discretization, though modification to the transport discretization also influences the elliptic pressure discretization. The discretization principle used throughout this work is the finite volume methodology. Here we discuss the integral form of a scalar hyperbolic equation and the implications for the discretization.

Consider the two-dimensional scalar hyperbolic equation,

$$c_t + \nabla \cdot \begin{pmatrix} f(c) \\ g(c) \end{pmatrix} = q(c),$$

where $f(c)$ and $g(c)$ are hyperbolic fluxes in the x and y directions, respectively, and $q(c)$ is the source term. The variable c is the independent scalar quantity of interest, which we will call mass. Assuming that we have a grid defined by control volumes Ω_i with volumes V_i we define the average mass in a control volume Ω_i at time t^n as

$$C_i^n = \frac{1}{V_i} \iiint_{\Omega_i} c(\boldsymbol{x}, t^n)\, dV. \tag{2.13}$$

We then introduce the conservative form by spatial integration over the grid cell, temporal integration

from time t^n to t^{n+1}, and scaling by $1/V_i$. This gives

$$\frac{1}{V_i}\int_{t^n}^{t^{n+1}}\iiint_{\Omega_i}\left[\frac{c}{\partial t}+\nabla\cdot\begin{pmatrix}f(c)\\g(c)\end{pmatrix}-q(c)\right]\,d\Omega\,dt=0.$$

Assuming that the control volumes do not change with time, we can use the Fundamental Theorem of Calculus along with the divergence theorem so that the average mass in a cell is now evolved by

$$C_i^{n+1}=C_i^n-\frac{\Delta t}{V_i}\sum_{j\in neigh\{i\}}\mathcal{F}_{i,j}^n+\frac{\Delta t}{V_i}Q_i^n, \tag{2.14}$$

where $neigh\{i\}$ is the set of neighboring cells to cell i and Q_i^n is the integrated source term

$$Q_i^n=\int_{t^n}^{t^{n+1}}\iiint_{\Omega_i}q_(c)\,dV\,dt.$$

The mass flux between Ω_i and Ω_j is

$$\mathcal{F}_{i,j}=\int_{t^n}^{t^{n+1}}\iint_{\partial\Omega_{i,j}}\begin{pmatrix}f(c)\\g(c)\end{pmatrix}\cdot\widehat{n}_{i,j}\,ds\,dt,$$

where $\partial\Omega_{i,j}$ is the face between Ω_i and Ω_j with the unit normal $\widehat{n}_{i,j}$ pointing from Ω_i to Ω_j. The crux of any finite volume method is the determination of the mass flux integral, called a numerical flux when approximated. Clearly a requirement for the scheme to be conservative is that

$$\mathcal{F}_{i,j}=-\mathcal{F}_{j,i}.$$

In most of this thesis the only gridding methodology used is Cartesian. For a Cartesian grid the control volumes generally have cell centers (x_i,y_j) with horizontal and vertical extents Δx and Δy, respectively. The control volumes are then labeled as $\Omega_{i,j}$ and a point (x,y) is in control volume $\Omega_{i,j}$ if $x\in x_i\pm\Delta x/2$ and $y\in y_j\pm\Delta y/2$. We generally refer to the horizontal (west-east) fluxes as $\mathcal{F}_{i\pm1/2,j}$ and vertical (south-north) fluxes as $\mathcal{G}_{i,j\pm1/2}$.

Chapter 3

Near-Well, Early-Time Effects and Solution Coupling Methods

As noted previously, in adverse mobility ratio flows, $\mu_o > \mu_g$, grid orientation effect (GOE) arises due to numerical errors triggering a physical instability. An important consideration is the implementation of the numerical scheme in the near-well region and the numerical treatment of the well. As we will show, this can have a significant effect on the evolution of these physically unstable flows.

A simple conceptual picture illustrates this concept. Figure 3.1 shows the initial conditions for two different Cartesian grids oriented at different angles with respect to the principle flow direction unfolded onto a radial grid (see section 3.1). The dotted curve in the figure shows the expected front near the injection well for a homogeneous system. In the radial grid system, it is clear that if the initial flow around the well is different for the two grids, hence the evolution of the instability will be different. Of course, at later times, the interaction of the flow paths will change the evolution of the instability from the simple picture shown here.

This concept leads us into the thrust of this chapter. We seek to create a method that reduces or removes the numerical perturbations caused by the inlet conditions and the rotational dependent terms in the numerical scheme to ensure that effects of the physical instability are not masked by numerical effects. Instead we expect in a real simulation that the details of the permeability field near the well will control the evolution of the instabilities rather than the numerical issues. The methods developed here, though motivated by the desire to alleviate the grid orientation effect, have wider applicability in many near-well and solution coupling problems.

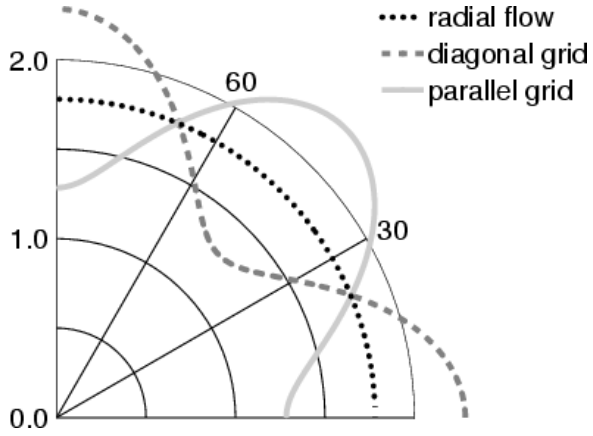

Figure 3.1: Effective initial conditions after two time steps for an explicit scheme on diagonal and parallel grids

In this chapter we will exclusively consider the miscible model in the fractional flow form,

$$0 = -\nabla \cdot \frac{\boldsymbol{K}}{\mu_{e,g}(S_g)} \nabla p \equiv \nabla \cdot \boldsymbol{u}, \tag{3.1}$$

$$0 = \phi \frac{\partial c_g}{\partial t} + \nabla \cdot (c_g \boldsymbol{u}), \tag{3.2}$$

as was derived in Equations 2.10 and 2.11. Since there are no gravitational effects, the equations do not change character if we assume that $\rho_g = \rho_o = 1$ and thus let $c_g = S_g$. Since $S_o = 1 - S_g = c_o$ we let $c \equiv c_g$ and can recover $c_o = 1 - c = 1 - c_g$ when needed.

3.1 Quarter Five-spot Problem

We briefly present the quarter five-spot model which will be used throughout this work as a test problem for GOE. There are two principle domains of symmetry for this problem: the diagonal domain in which the mean flow (between the wells) is diagonal to the grid lines, and the parallel domain in which the mean flow is parallel to the grid lines.

By symmetry, the domain boundary, indicated by the dotted line in Figure 3.2, is a no-flow boundary. Care must be taken when handling this boundary condition, as improper handling can mask the effects of the numerics. For the diagonal domain the wells are in cells $(1,1)$ and (N,N) and for the parallel domain the wells are in cells $(1,1)$, $(1,N)$, $(N,1)$, and (N,N), as shown in Figure 3.2. With this placement of the wells, the problem is symmetric around the center of the border cells. Therefore, the no-flow boundary is not in fact the outer edge of the domain but rather the line passing through the cell centers. This implies that the proper way to handle the boundary is with ghost cells $C_{0,j} = C_{2,j}$, $C_{N+1,j} = C_{N-1,j}$, $C_{i,0} = C_{i,2}$, and $C_{i,N+1} = C_{i,N-1}$. The same ghost

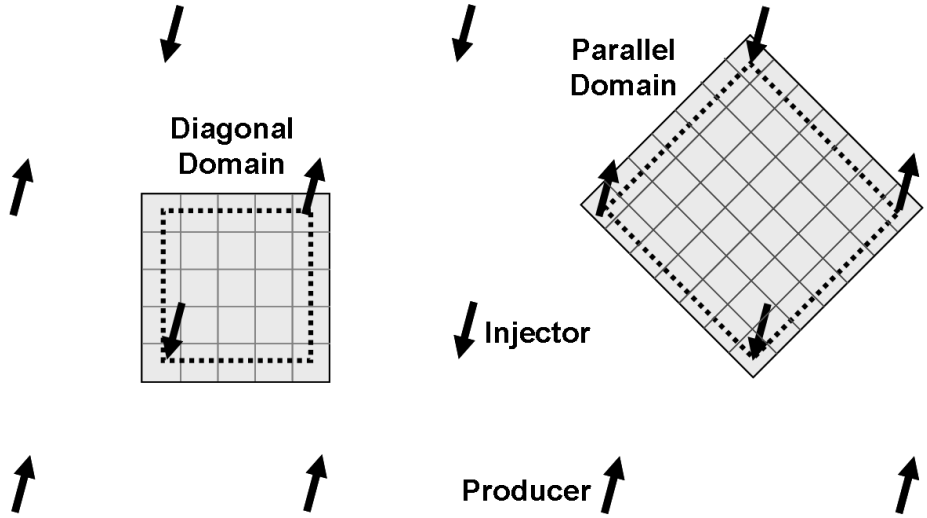

Figure 3.2: Periodically repeating 5 spot pattern with two quarter five-spot domains

cell framework is used for solving the pressure equation.

3.2 Shubin and Bell Family of Discretizations

The discretization method for transport and pressure that we adopt in this chapter is the variable nine-point sequential method developed and discussed in Shubin and Bell (1984). Defining the velocities on the grid as

$$u^n_{i+1/2,j} = \left(\frac{K}{\mu}\right)^n_{i+1/2,j} \frac{p^n_{i+1,j} - p_{i,j}}{\Delta x},$$
$$v^n_{i,j+1/2} = \left(\frac{K}{\mu}\right)^n_{i,j+1/2} \frac{p^n_{i,j+1} - p_{i,j}}{\Delta x}.$$

Equation 3.1 is discretized as

$$(I + \beta\delta_y^2)\frac{\delta_x}{\Delta x}u_{i,j} + (I + \beta\delta_x^2)\frac{\delta_y}{\Delta y}v_{i,j} = q_{i,j},$$

where $\delta_x f_{i,j} = f_{i+1/2,j} - f_{i-1/2,j}$ and $\delta_x^2 f_{i,j} = f_{i+1,j} - 2f_{i,j} - f_{i-1,j}$, and similarly for δ_y and δ_y^2. The parameter $\beta \in [0, 1/2]$ controls the influence of the cross flow in the scheme. With $\beta = 0$ this is the standard five-point Laplacian discretization. In the homogeneous case, $\beta = 1/12$ leads to the standard fourth order, nine-point discretization of the Laplacian (Strikwerda, 2004).

These velocities are then used to solve Equation 3.2 via the implicit discretization

$$
\begin{aligned}
&\hat{c}_{i,j}^{n+1} q_{i,j} = \\
&\frac{c_{i,j}^{n+1} - c_{i,j}^{n}}{\Delta t} + \left\{ (I + 2\beta\bar{\delta}_y^2)\frac{\delta_x}{\Delta x}(u_{i,j}c_{i,j}^*) + (I + 2\beta\bar{\delta}_x^2)\frac{\delta_y}{\Delta y}(v_{i,j}c_{i,j}^*) \right\} \\
&- \frac{\delta_x}{\Delta x}\left(2\beta d_{i,j+1/2}^{11}\frac{\delta_x}{\Delta x}c_{i,j+1/2}^* + (1-2\beta)d_{i,j}^{11}\frac{\delta_x}{\Delta x}c_{i,j}^* + 2\beta d_{i,j-1/2}^{11}\frac{\delta_x}{\Delta x}c_{i,j-1/2}^* \right) \\
&- \frac{\delta_y}{\Delta y}\left(2\beta d_{i+1/2,j}^{22}\frac{\delta_y}{\Delta y}c_{i+1/2,j}^* + (1-2\beta)d_{i,j}^{22}\frac{\delta_y}{\Delta y}c_{i,j}^* + 2\beta d_{i-1/2,j}^{22}\frac{\delta_y}{\Delta y}c_{i-1/2,j}^* \right) \\
&- \frac{\delta_x}{\Delta x}\left(d_{i,j}^{12}\frac{\delta_y}{\Delta y}c_{i,j}^* \right) \\
&- \frac{\delta_y}{\Delta y}\left(d_{i,j}^{21}\frac{\delta_x}{\Delta x}c_{i,j}^* \right),
\end{aligned}
\tag{3.3}
$$

where $C_{i,j}^*$ can either be taken explicitly or implicitly and for smoothness, a numerical diffusion tensor has been added,

$$
D_{i,j} = \begin{bmatrix} d_{i,j}^{11} & d_{i,j}^{12} \\ d_{i,j}^{21} & d_{i,j}^{22} \end{bmatrix},
$$

reducing the order of the scheme from second to first order. In Equation 3.3 $\bar{\delta}_x^2 f_{i,j} = f_{i+1/2,j} - 2f_{i,j} + f_{i-1/2,j}$, similarly for $\bar{\delta}_y^2$. Averaging is used to interpolate the concentrations and velocities where not already defined,

$$
\begin{aligned}
c_{i+1/2,j} &= \frac{1}{2}(c_{i,j} + c_{i+1,j}), \\
c_{i,j+1/2} &= \frac{1}{2}(c_{i,j} + c_{i,j+1}), \\
c_{i+1/2,j+1/2} &= \frac{1}{4}(c_{i,j} + c_{i+1,j} + c_{i,j+1} + c_{i+1,j+1}), \\
u_{i+1/2,j+1/2} &= \frac{1}{2}(u_{i+1/2,j} + u_{i+1/2,j+1}), \\
u_{i,j+1/2} &= \frac{1}{4}(u_{i+1/2,j} + u_{i+1/2,j+1} + u_{i-1/2,j} + u_{i-1/2,j+1}), \\
v_{i+1/2,j+1/2} &= \frac{1}{2}(v_{i,j+1/2} + v_{i+1,j+1/2}), \\
v_{i+1/2,j} &= \frac{1}{4}(v_{i,j+1/2} + v_{i+1,j+1/2} + v_{i,j-1/2} + v_{i+1,j-1/2}).
\end{aligned}
$$

We control the time step with

$$
dt = \alpha \Delta x / \max(\max_{i,j}(|u_{i+1/2,j}|), \max_{i,j}(|v_{i,j+1/2}|)),
$$

where α is the CFL restriction. When the method is used implicitly there is no restriction on α, though we use $\alpha = 1$ so as to control the amount of longitudinal diffusion. For explicit simulation

we chose $\alpha = 1/2$, which is the stability constraint for single point upstream weighting.

We remark that this Shubin and Bell scheme does not generate a divergence free velocity field for $\beta \neq 0$. Therefore we use $\beta = 0$ in our development of the forcing method so that the methods can be applied to more general transport discretizations based on divergence free velocity fields.

Various schemes with different truncation errors, stability properties, and levels of grid dependence can be obtained through the use of different numerical diffusion terms. Particularly if we take $\beta = 0$ and

$$D^{uw} = \begin{bmatrix} \frac{1}{2}\Delta x|u| & 0 \\ 0 & \frac{1}{2}\Delta y|v| \end{bmatrix}, \tag{3.4}$$

the scheme becomes the standard single point upstream (SPU) scheme, or donor cell upwinding.

Shubin and Bell (1984) propose a numerical diffusion term inspired by the modified equations. The modified equations are formed using Taylor expansion around the point $c(x_i, y_j, t^n)$. We retain the leading error terms and convert temporal derivatives to spatial derivatives using the original governing equation (Equation 3.2). The modified equations can be interpreted as the nearby problem that a scheme is solving to higher order. The modified equation for the transport discretization is

$$\phi\frac{\partial c}{\partial t} + \nabla\cdot(\mathbf{u}c) = \nabla\cdot\left(\begin{bmatrix} d^{11} & d^{12} \\ d^{21} & d^{22} \end{bmatrix} + \frac{1}{2}\Delta t \begin{bmatrix} u^2 & uv \\ uv & v^2 \end{bmatrix}\right)\nabla c + \mathcal{O}(\Delta t^2, \Delta x^2, \Delta y^2), \tag{3.5}$$

where we must assume to do this analysis that $(u, v)^T = \gamma(\cos\theta, \sin\theta)^T$, that is, that the velocity field is constant at an angle θ with respect to the grid and has a constant magnitude γ.

To interpret the numerically introduced diffusion tensor, it is more natural to transform Equation 3.5 to the streamline coordinate system which is aligned with the velocity field (Van Ransbeeck and Hirsch, 1997; Roe and Sidilkover, 1992). Let this coordinate system be denoted by (s, n), where s is the streamline coordinate aligned with the velocity field and n is the coordinate normal to the velocity field. The transformation from Cartesian coordinates to streamline coordinates is accomplished with the rotation matrix

$$\mathbf{Q} = \begin{bmatrix} \cos\theta & \sin\theta \\ -\sin\theta & \cos\theta \end{bmatrix},$$

so that

$$\begin{bmatrix} s \\ n \end{bmatrix} = \mathbf{Q}\begin{bmatrix} x \\ y \end{bmatrix}, \qquad \text{and} \qquad \begin{bmatrix} x \\ y \end{bmatrix} = \mathbf{Q}^T\begin{bmatrix} s \\ n \end{bmatrix}.$$

Applying this transform to Equation 3.5 the leading error term (Shubin and Bell, 1984; Roe and

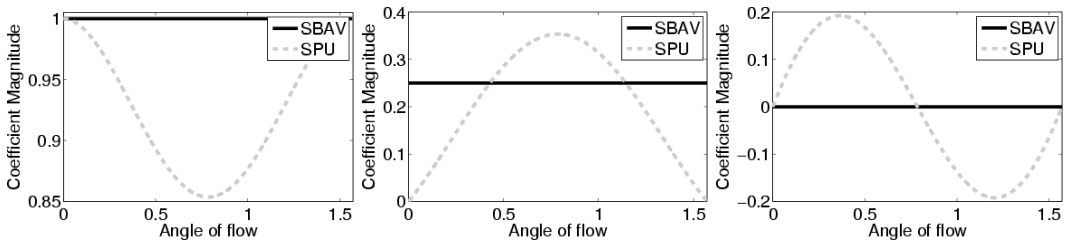

(a) Longitudinal diffusion (b) Transverse diffusion (c) Cross-term diffusion

Figure 3.3: Plots of the magnitude of the various diffusion coefficients scaled by $1/h$ (assuming that $\Delta x = \Delta y = h$) against angle of flow to the original grid coordinates. The ratio of $\Delta t/h$ is set to unity.

Sidilkover, 1992) becomes

$$\begin{aligned}\phi c_t + \gamma c_s = &\underbrace{\left(d^{11}u_\alpha^2 + (d^{12}+d^{21})u_\alpha v_\alpha + d^{22}v_\alpha + \frac{1}{2}\Delta t\right)}_{d_{ss}} c_{ss} \\ &+ \underbrace{\left(2(d^{22}-d^{11})u_\alpha v_\alpha + (d^{12}+d^{21})(u_\alpha^2+v_\alpha^2)\right)}_{d_{sn}} c_{sn} \\ &+ \underbrace{\left(d^{11}v_\alpha^2 - (d^{12}+d^{21})u_\alpha v_\alpha + d^{22}u_\alpha\right)}_{d_{nn}} c_{nn}.\end{aligned} \tag{3.6}$$

The coefficients d_{ss}, d_{nn} can be interpreted as longitudinal and transverse diffusion, respectively, and a nonzero mixed-term d_{sn} indicates that there is some rotation of the tensor relative to the streamline coordinates (Roe and Sidilkover, 1992; Van Ransbeeck and Hirsch, 1997).

From this analysis Shubin and Bell proposed a numerical diffusion that makes the discretization rotationally invariant to second order regardless of the choice of β. It is given by

$$\mathbf{D}^{SBAV} = \frac{\max\{\Delta x, \Delta y\}}{2\sqrt{u^2+v^2}} \begin{bmatrix} u^2 + \frac{1}{2}v^2 & \frac{1}{2}uv \\ \frac{1}{2}uv & v^2 + \frac{1}{2}u^2 \end{bmatrix}. \tag{3.7}$$

We refer to this scheme as the Shubin and Bell artificial viscosity (SBAV). In Figure 3.3 we plot the diffusion coefficients for SBAV and SPU. The plots show that for SBAV the numerical diffusion is isotropic to first order. Also, Equation 3.6 reveals that as long as the numerical diffusion tensor is chosen independent of the time step size, the time stepping error only affects the longitudinal diffusion. Furthermore, Equation 3.6 is independent of β, which implies that SBAV is rotationally invariant to first order for all values of β. Different β values affect the higher order error terms

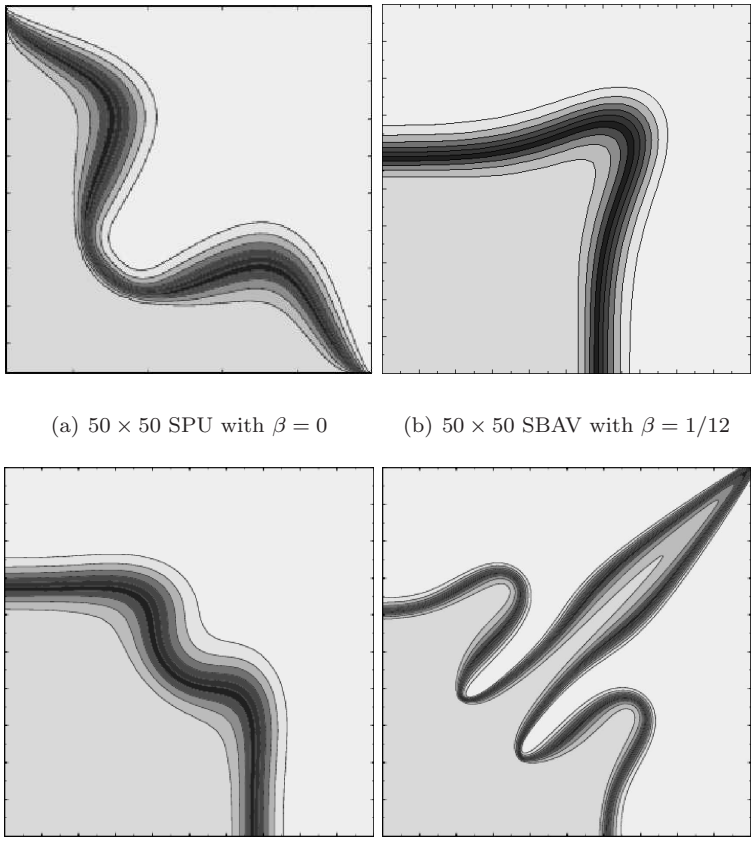

(a) 50×50 SPU with $\beta = 0$ (b) 50×50 SBAV with $\beta = 1/12$

(c) 50×50 SBAV with $\beta = 0$ (d) 200×200 SBAV with $\beta = 1/12$

Figure 3.4: SPU and SBAV comparison along with break down of SBAV under sufficient refinement. $M = 30$ and CFL $\alpha = 1$.

differently, with $\beta = 1/12$ resulting in a more isotropic second order error term than $\beta = 0$ (Shubin and Bell, 1984).

Consider again the quarter five-spot problem discussed in the introduction. SBAV reduces the grid orientation effect significantly as compared to SPU for both $\beta = 0$ and $\beta = 1/12$. However, SBAV still breaks down under sufficient refinement as shown in Figure 3.4 and introduces grid and scheme dependent numerical fingers despite having rotationally invariant first order error terms.

Since the transport equation is linear and the discretizations are stable and consistent, the manifestation of the grid orientation effect must be attributed to the ill-posedness of the underlying physical model for high Peclet number flows (Tan and Homsy, 1997). By this we naturally do not mean that grid orientation effects are physical phenomena: the flow knows nothing of the computational grid. Rather, grid dependent errors provide a trigger for the physical instability,

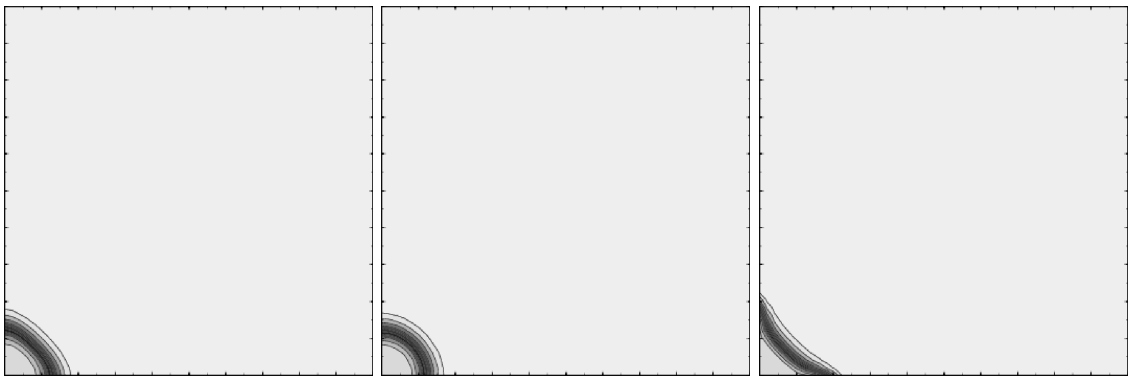

(a) SBAV with $\beta = 0$ (b) SBAV with $\beta = 1/12$ (c) SPU

Figure 3.5: Early-time simulation shown at 0.025 PVI on a 50×50 diagonal domain grid.

which is then amplified by the ill-posedness of the problem into the grid dependent behavior we see in the grid orientation effect.

3.3 Early-Time and Near-Well

Since perturbations and errors made in early-time and near-well flow are amplified as the simulation continues (Tan and Homsy, 1997; Brand et al., 1991), we seek to improve the robustness of numerical schemes by alleviating or reducing the numerical disturbances introduced near the injection well during the early stages of the injection process.

Evidence of the importance of early-time and near-well flow is given in Figures 3.5(a) and 3.5(b). The figures show the simulated flow at 0.025 pore volumes injected (PVI) with SBAV for $\beta = 0$ and $\beta = 1/12$, respectively. The simulations for $\beta = 0$ show a flattened fluid front and a bias of the flow along the principal grid directions. However, the scheme for $\beta = 1/12$ preserves the expected radial nature of the front around the well. We also show early-time and near-well solutions for SPU in Figure 3.5(c). Both SBAV with $\beta = 0$ and SPU lead to the formation of numerical fingers in the early stages of the injection process near the injection well.

3.3.1 Near-Well Results

To investigate the impact of the near-well region, we apply the SBAV scheme with $\beta = 1/12$ to the 10×10 grid cell square around the injection well and transition to the less grid dependent SBAV with $\beta = 0$ or the SPU scheme away from the well. The simulations are run to 0.4 PVI with a mobility ratio of $M = 30$ on the diagonal quarter five-spot problem. The results for switching to

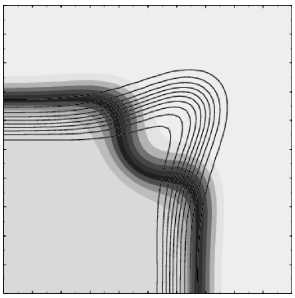

(a) SBAV with $\beta = 0$ reference solution

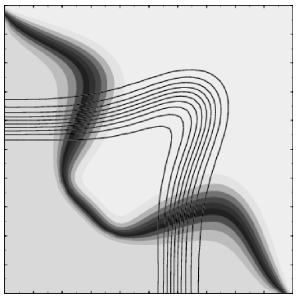

(b) SPU reference solution

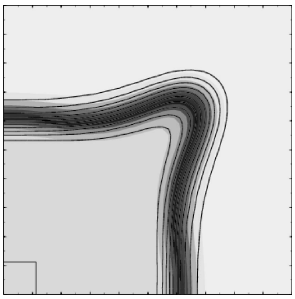

(c) SBAV with $\beta = 0$ in the interior

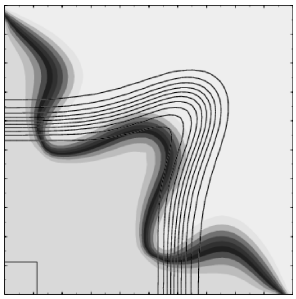

(d) SPU in the interior

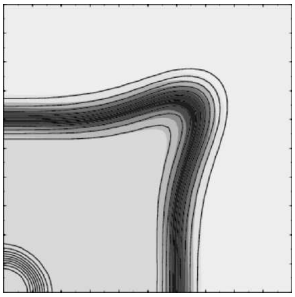

(e) SBAV with $\beta = 0$ after early-time

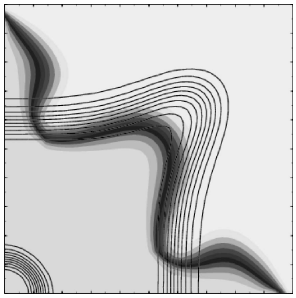

(f) SPU after early-time

Figure 3.6: Reference solutions for the simulations are given as black contour lines. All run to 0.4 PVI on a 50×50 diagonal domain grid.

SBAV are shown in Figure 3.6(c) and SPU in Figure 3.6(d). The reference solution, computed with SBAV and $\beta = 1/12$ in the entire domain, is given in the background of each figure as black contour lines. Figures 3.6(a) and 3.6(b) provide reference solutions generated with SBAV with $\beta = 0$ and SPU, respectively, with no special handling near the injection well.

As can be seen in these figures, a change in the handling of flow around the injection well greatly affect the shape of the resulting front regardless of the interior scheme used. SPU still introduces two non-physical grid aligned numerical fingers, but the magnitude of these fingers is reduced. Also, a third finger is introduced in the solution front, which is not aligned with the grid, but rather points in the direction of the producing well. The results are considerably better when SBAV is used. Then, only a few grid blocks around the well are needed to essentially match the $\beta = 1/12$ SBAV reference solution. Similar results can be observed on the parallel domain.

3.3.2 Early-Time

To explore the early-time effects, we use SBAV with $\beta = 1/12$ to initialize the flow up to time $t_c = 0.025$ PVI, and switch to $\beta = 0$ for the remainder of the simulation. This is equivalent to starting the computation with a different initial condition. Again we take as final time 0.4 PVI, and a mobility ratio of $M = 30$. Results for SBAV and SPU are provided in Figures 3.6(e) and 3.6(f) respectively. The SBAV with $\beta = 1/12$ reference solution is shown as black contours as is the modified initial condition.

Once again the results suggest that the handling of the injection well boundary conditions is crucial to properly capture the front. SPU still displays some grid dependencies, but the solutions are greatly improved. SBAV captures the proper shape of the front with only a slightly modified initial condition. These results strongly suggest that the early-time perturbations have a stronger effect on the solution than the later time flow and that boundary conditions need to be treated with great care in adverse mobility simulation. Again similar results were seen on the parallel domain.

3.4 Forcing Methods

The strong effects of early-time and near-well flow on the simulation results motivate the idea of forcing a near-well solution that is derived from an analytical solution or fine scale simulation. This should be done in a manner that minimizes grid dependent errors in the transfer. It is also desirable that this process adds little to the computational complexity of the problem and is easily implemented into existing simulators. The methods developed in the remainder of this chapter, though motivated by the desire to alleviate the grid orientation effect, have wider applicability in many near-well and solution coupling problems.

From a mathematical standpoint we desire to modify the original system of equations,

$$-\nabla \cdot \frac{K(x,y)}{\mu(c)}\nabla p = \nabla \cdot \mathbf{u} = q, (x,y,t) \in \Omega \times (0,T),$$
$$\phi \frac{\partial c}{\partial t} + \nabla \cdot (\mathbf{u}c) = \hat{c}q, (x,y,t) \in \Omega \times (0,T),$$

and instead solve

$$\begin{aligned} &-\nabla \cdot \frac{K(x,y)}{\mu(c)}\nabla p = \nabla \cdot \mathbf{u} = q, && (x,y,t) \in \Omega \times (0,T), \\ &\phi \frac{\partial c}{\partial t} + \nabla \cdot (\mathbf{u}c) = \hat{c}q, && (x,y,t) \in \Omega \times (0,T), \\ &\text{subject to } \mathbf{u} \equiv \tilde{\mathbf{u}}, && (x,y,t) \in \Gamma \times (0,T), \\ &\text{subject to } c \equiv \tilde{c}, && (x,y,t) \in \Gamma \times (0,T), \end{aligned} \tag{3.8}$$

where Γ defines the near-well region, and $\tilde{c}$ and $\tilde{u}$ are the analytic solutions for the near-well region. We also note here that this special treatment is only applied to the injection well.

We assume that the near-well solution is a radial flow solution governed by

$$\begin{aligned} \frac{\partial}{\partial r}(ru_r) + \frac{\partial v_\theta}{\partial \theta} &= 0, \\ \frac{\partial c}{\partial t} + \frac{\partial}{\partial r}(u_r r c) + \frac{1}{r}\frac{\partial}{\partial \theta}(v_\theta c) &= \frac{1}{Pe}\left[\frac{1}{r}\frac{\partial}{\partial}\left(r\frac{\partial c}{\partial r}\right) + \frac{1}{r^2}\frac{\partial^2 c}{\partial \theta^2}\right], \end{aligned} \tag{3.9}$$

where $Pe = q/D$, q is the injection rate, and D is the scalar diffusion coefficient. Exploiting the necessary radial symmetry, this admits the following base state axisymmetric solution (Tan and Homsy, 1997)

$$\begin{aligned} u_r &= \frac{1}{2\pi r}, \\ v_\theta &= 0, \\ c &= \frac{1 - \int_0^\eta s^{(Pe/2\pi - 1)} \exp(-s^2/2)\, ds}{\int_0^\infty s^{(Pe/2\pi - 1)} \exp(-s^2/2)\, ds}, \end{aligned} \tag{3.10}$$

where

$$\eta = r\left(\frac{Pe}{2t}\right)^{1/2}.$$

The above concentration equation can be integrated and restated as

$$c(r,t) = \frac{\Gamma\left[\frac{Pe}{4\pi}, r^2\frac{Pe}{4t}\right]}{\Gamma\left[\frac{Pe}{4\pi}\right]},$$

where

$$\Gamma(a,x) = \int_x^\infty s^{a-1}\exp(-s)\,ds,$$

and

$$\Gamma(a) = \int_0^\infty s^{a-1}\exp(-s)\,ds.$$

In the original Cartesian coordinate system Equation 3.10 becomes

$$\begin{aligned}\tilde{u} &= \frac{x}{2\pi(x^2+y^2)},\\ \tilde{v} &= \frac{y}{2\pi(x^2+y^2)},\\ \tilde{c} &= \frac{\Gamma\left[\frac{Pe}{4\pi},(x^2+y^2)\frac{Pe}{4t}\right]}{\Gamma\left[\frac{Pe}{4\pi}\right]}.\end{aligned} \tag{3.11}$$

We have left the Peclet number in these solutions, even though we do not explicitly model physical diffusion in our simulations, for two reasons. First, if we set the Peclet number to ∞ (the zero diffusion limit) the displacement is piston-like which is not realistic since the physical solution will have diffusion. Second, and more importantly, for most applications near-well solutions result from fine-scale numerical simulations which will exhibit some numerical diffusion. The numerical Peclet number of the fine-scale model will be larger than the numerical Peclet number of the coarser background grid, hence we choose the Peclet number such that $Pe_{num} < Pe = 400 < \infty$.

3.4.1 Well-Sponge

The first method we discuss is the well-sponge, which is based on sponge methods developed in computational acoustics for enforcing boundary conditions (Bodony, 2006). In the well-sponge formulation Equations 3.8 become

$$\begin{aligned}-\nabla\cdot\frac{K(x,y)}{\mu(c)}\nabla p = \nabla\cdot\mathbf{u} &= -\sigma(r)(p-\tilde{p})+q, && (x,y,t)\in\Omega\times(0,T),\\ \phi\frac{\partial c}{\partial t}+\nabla\cdot(\mathbf{u}c) &= -\sigma(r)(c-\tilde{c})+\hat{c}q, && (x,y,t)\in\Omega\times(0,T),\end{aligned}$$

where $\sigma(r)$ is a penalty function, which is large near the well and decays away from the well. This forces $p=\tilde{p}$ and $c=\tilde{c}$ in the near-well region. Bodony (2006) suggests using an exponential penalty function

$$\sigma(r) = \begin{cases}\sigma_{\max} & \text{if } 0\le r\le r_0\\ \sigma_{\max}\exp(-\gamma(r-r_0)^2) & \text{if } r_0\le r\end{cases}, \tag{3.12}$$

where $\sigma_{\max}$ and γ are parameters controlling the strength of the sponge and the size of the transition zone, respectively, and r_0 is the size of the radial region in which we desire to enforce radial flow. In

our study we have used $\sigma_{\max} = 10^5$ and $\gamma = 10^4$. We have also tested a hard transition where

$$\sigma(r) = \begin{cases} \sigma_{\max} & \text{if } r \le r_0 \\ 0 & \text{if } r > r_0 \end{cases},$$

and a transition involving the tanh function. All these well-sponge functions show similar results and all are non-conservative as discussed below.

We can write these equations in finite volume form (see section 2.6) as

$$C_{ij}^{n+1} = C_{ij}^n - \frac{\Delta t}{\Delta x}\left[F_{i+1/2,j} - F_{i-1/2,j}\right] - \frac{\Delta t}{\Delta y}\left[G_{i,j+1/2} - G_{i,j-1/2}\right] - \frac{1}{\Delta x \Delta y}\int_{t^n}^{t^{n+1}} \left(\iint_{\Omega_{ij}} \sigma(r)(c - \tilde{c}) dV \right) dt,$$

where

$$C_{i,j}^n = \frac{1}{\Delta x \Delta y} \iint_{\Omega_{ij}} c(x, y, t^n)\, dV,$$

$$F_{i+1/2,j} = \frac{1}{\Delta t \Delta y} \int_{t^n}^{t^{n+1}} \int_{y_{j-1/2}}^{y_{j+1/2}} u(x_{i+1/2}, y, t) c(x_{i+1/2}, y, t)\, dy\, dt,$$

$$G_{i,j+1/2} = \frac{1}{\Delta t \Delta x} \int_{t^n}^{t^{n+1}} \int_{x_{i-1/2}}^{x_{i+1/2}} v(x, y_{j+1/2}, t) c(x, y_{j+1/2}, t)\, dx\, dt.$$

Numerically we approximate $F_{i+1/2,j} \approx \mathcal{F}_{i+1/2,j}$ and $G_{i,j+1/2} \approx \mathcal{G}_{i,j+1/2}$, where $\mathcal{F}$ and $\mathcal{G}$ are the numerical fluxes from the scheme used.

We write the pressure equation as

$$\frac{1}{\Delta x}\left[\tilde{F}_{i+1/2,j} - \tilde{F}_{i-1/2,j}\right] - \frac{1}{\Delta y}\left[\tilde{G}_{i,j+1/2} - \tilde{G}_{i,j-1/2}\right] = \frac{1}{\Delta x \Delta y} \iint_{\Omega_{ij}} \sigma(r)(p - \tilde{p})\, ds, \tag{3.13}$$

where

$$\tilde{F}_{i+1/2,j} = \frac{1}{\Delta y} \int_{y_{j-1/2}}^{y_{j+1/2}} u\, ds,$$

$$\tilde{G}_{i,j+1/2} = \frac{1}{\Delta y} \int_{x_{i-1/2}}^{x_{i+1/2}} v\, ds,$$

and u and v are the numerically determined velocities. This method requires the velocity field to be divergence free, and hence necessitates $\beta = 0$ in Equation 3.3.

To evaluate the volume integrals, we assume that the unknown variables are piecewise constant across the cells. Then,

$$\frac{1}{\Delta x \Delta y} \int_{t^n}^{t^{n+1}} \iint_{\Omega_{ij}} \sigma(r) c \, dV dt \approx \frac{\Delta t}{\Delta x \Delta y} C_{i,j}^{n+1} \iint_{\Omega_{ij}} \sigma(r) \, dV,$$

and similarly

$$\frac{1}{\Delta x \Delta y} \iint_{\Omega_{ij}} \sigma(r) p \, dV \approx \frac{1}{\Delta x \Delta y} P_{i,j} \iint_{\Omega_{ij}} \sigma(r) \, dV.$$

The remaining volume integrals need to be evaluated only once at the beginning of the simulation. We evaluate the exact solution $\tilde{c}$ and $\tilde{p}$ implicitly. For $\tilde{c}$, this gives

$$\frac{1}{\Delta x \Delta y} \int_{t^n}^{t^{n+1}} \iint_{\Omega_{ij}} \sigma(r) \tilde{c} \, dV dt \approx \frac{\Delta t}{\Delta x \Delta y} \iint_{\Omega_{ij}} \sigma(r) \tilde{c}(r, t^{n+1}) \, dV dt,$$

where we use five-point Gaussian quadrature in both spatial directions. This integral must be evaluated at each time step, but only in the few grid blocks around the injection well where the well-sponge is non-zero. Once the front has passed completely through the sponge, the integral is constant in time so no additional computations are necessary. A similar approach is used for the integral containing $\tilde{p}$.

3.4.2 Local Embedding Through Immersed Structures (LETIS)

The well-sponge method is not fully conservative: numerical experiments show that as the sponge passes through the transition region, extra fluid is added to the system; the scheme is conservative before the front has reached the edge of the sponge and after it has completely passed through the sponge. The non-conservative behavior can be understood by considering two cells, (i, j) and $(i+1, j)$, where cell (i, j) is completely inside the sponge and cell $(i+1, j)$ is in the transition region of the sponge. If the numerical flux, $\mathcal{F}_{i+1/2,j}$, is greater than the flux of the forced solution for this face more volume will enter cell $(i + 1, j)$ than will have left cell (i, j) after the correction of the sponge is applied, thus adding volume to the system. The effect is reduced if the Peclet number of the forced solution and the numerical scheme are similar, because then the numerical and near-well fluxes are in closer agreement for the transition cells.

When near-well solutions are provided by fine-scale simulations, it cannot be guaranteed that the Peclet numbers are similar. We therefore seek to formulate a fully conservative method. We can achieve this by forcing the fluxes rather than the solutions in the near-well region. This approach is motivated by the Immersed Boundary Method (IBM) commonly used in the area of computational fluid dynamics (Mittal and Iaccarino, 2005). In the context of our simulations, we refer to it as Local Embedding Through Immersed Structures (LETIS).

Without loss of generality we will assume, for simplicity, that the near-well region is defined by a circle of radius r_{nw} around the injection well. Consider the grid shown in Figure 3.7 in which the

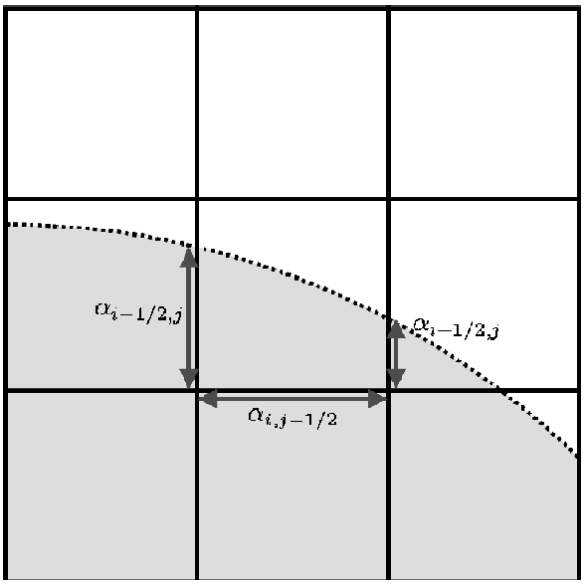

Figure 3.7: Example of a near-well region LETIS grid

gray region is the near-well region, Γ in Equation 3.8. Consider the center cell, (i, j), with faces $(i+1/2, j)$, $(i-1/2, j)$, $(i, j+1/2)$, and $(i, j-1/2)$. We define parameters $\alpha_{i+1/2,j}$, $\alpha_{i-1/2,j}$, $\alpha_{i,j+1/2}$, and $\alpha_{i,j-1/2}$ as the fraction of the face within the near-well region. In the case shown this gives

$$\alpha_{i+1/2,j} = 0.38, \qquad \alpha_{i-1/2,j} = 0.75,$$
$$\alpha_{i,j+1/2} = 0, \qquad \alpha_{i,j-1/2} = 1.$$

Note that since this approach we are forcing fluxes and do not have solid boundaries we do not end up with the small cell problem as is common Immersed Boundary Methods. We can have α values which are close to 0 or 1, though not necessary for stability we found it lead to slightly improved results to correct the α so that

$$\alpha = \begin{cases} 0, & \text{if } \alpha < \alpha_{\min} \\ 1, & \text{if } \alpha > 1 - \alpha_{\min} \\ \alpha, & \text{otherwise} \end{cases},$$

where $\alpha_{\min} = 0.85$. Computationally we have found that the LETIS method has no impact on the stability or the time step selection, though this is a results which warrants further exploration in future work (see chapter 7).

To ensure that the velocity field is divergence free, which is important for consistency and stability

of most of the numerical transport schemes, we require that in each cell

$$u_{i+1/2,j} - u_{i-1/2,j} + v_{i,j+1/2} - v_{i,j-1/2} = 0,$$

assuming the faces have the same length. We denote the face averaged, near-well normal velocities as $\tilde{u}$ and $\tilde{v}$. Assuming radial flow in the near-well region, these are given by

$$\begin{aligned}\tilde{u}_{i+1/2,j} &= \frac{1}{\Delta y}\int_{y_{j-1/2}}^{y_{j+1/2}} \frac{x_{i+1/2}}{2\pi(x_{i+1/2}^2 + y^2)})\, dy \\ &= \frac{1}{2\pi h}\left(\arctan\left(\frac{y_j + 1/2}{x_i + 1/2}\right) - \arctan\left(\frac{y_j - 1/2}{x_i + 1/2}\right)\right),\end{aligned}$$

and

$$\tilde{v}_{i,j+1/2} = \frac{1}{2\pi h}\left(\arctan\left(\frac{x_i + 1/2}{y_j + 1/2}\right) - \arctan\left(\frac{x_i - 1/2}{y_j + 1/2}\right)\right).$$

For simplicity we define the numerical face averaged normal velocities, $\bar{u}_{i+1/2,j}$ and $\bar{v}_{i,j+1/2}$, by a two-sided pressure difference with Darcy's law, so that

$$\bar{u}_{i+1/2,j} = -\left(\frac{k}{\mu}\right)_{i+1/2,j}(p_{i+1,j} - p_{i,j}),$$

and

$$\bar{v}_{i,j+1/2} = -\left(\frac{k}{\mu}\right)_{i,j+1/2}(p_{i,j+1} - p_{i,j}).$$

There are other ways to define the velocities, but our tests have shown that this choice works well for the problems considered. The divergence free velocity constraint becomes

$$\begin{aligned}&\alpha_{i+1/2,j}\tilde{u}_{i+1/2,j} + (1 - \alpha_{i+1/2,j})\bar{u}_{i+1/2,j} \\ &- \alpha_{i-1/2,j}\tilde{u}_{i-1/2,j} - (1 - \alpha_{i-1/2,j})\bar{u}_{i+1/2,j} \\ &+ \alpha_{i,j+1/2}\tilde{v}_{i,j+1/2} + (1 - \alpha_{i,j+1/2})\bar{v}_{i,j+1/2} \\ &- \alpha_{i,j-1/2}\tilde{v}_{i,j-1/2} - (1 - \alpha_{i,j-1/2})\bar{v}_{i,j+1/2} \\ &= 0.\end{aligned}$$

The above linear system of equations determines pressure in all cells that have one or more faces that are partially or completely within the near-well region. The divergence free face velocities are given by

$$\begin{aligned}u_{i+1/2,j} &= \alpha_{i+1/2,j}\tilde{u}_{i+1/2,j} + (1 - \alpha_{i+1/2,j})\bar{u}_{i+1/2,j}, \\ v_{i,j+1/2} &= \alpha_{i,j+1/2}\tilde{v}_{i,j+1/2} + (1 - \alpha_{i,j+1/2})\bar{v}_{i,j+1/2}.\end{aligned}$$

If $\alpha = 0$ for a given face, i.e. a face is completely within the near-well region, there will not be a numerical velocity for this face, and the face velocity is just the forced velocity.

For the transport equation we use the same α values and modify the standard finite volume formulation,

$$C_{ij}^{n+1} = C_{i,j}^{n} - \frac{\Delta t}{h}[F_{i+1/2,j} - F_{i-1/2,j} + G_{i,j+1/2} - G_{i,j-1/2}],$$

as

$$\begin{aligned} C_{ij}^{n+1} = C_{i,j}^{n} - \frac{\Delta t}{h}[&\alpha_{i+1/2,j}\tilde{F}_{i+1/2,j} + (1-\alpha_{i+1/2,j})\mathcal{F}_{i+1/2,j} \\ &-\alpha_{i-1/2,j}\tilde{F}_{i-1/2,j} - (1-\alpha_{i-1/2,j})\mathcal{F}_{i-1/2,j} \\ &+\alpha_{i,j+1/2}\tilde{G}_{i,j+1/2} + (1-\alpha_{i,j+1/2})\mathcal{G}_{i,j+1/2} \\ &-\alpha_{i,j-1/2}\tilde{G}_{i,j-1/2} - (1-\alpha_{i,j-1/2})\mathcal{G}_{i,j-1/2}], \end{aligned}$$

where $\tilde{F}$ and $\tilde{G}$ are the near-well solution fluxes and $\mathcal{F}$ and $\mathcal{G}$ are the numerical fluxes.

Assuming radial flow governed by Equation 3.9 with analytic solution Equation 3.11, the near-well fluxes are given by

$$\tilde{F}_{i+1/2,j} = \frac{1}{h^2}\int_{t^n}^{t^{n+1}}\int_{y_{j-1/2}}^{y_{j+1/2}} \left(\frac{x_{i+1/2}}{2\pi(x_{i+1/2}^2 + y^2)}\tilde{c}(x_{i+1/2}, y, t) - \frac{1}{Pe}\frac{\partial \tilde{c}}{\partial x}\bigg|_{x=x_{i+1/2}} \right) dydt,$$

$$\tilde{G}_{i,j+1/2} = \frac{1}{h^2}\int_{t^n}^{t^{n+1}}\int_{x_{i-1/2}}^{x_{i+1/2}} \left(\frac{y_{j+1/2}}{2\pi(x^2 + y_{j+1/2}^2)}\tilde{c}(x, y_{j+1/2}, t) - \frac{1}{Pe}\frac{\partial \tilde{c}}{\partial y}\bigg|_{y=y_{j+1/2}} \right) dxdt.$$

We integrate the diffusive portion of the flux exactly over time. For the remainder of the integral we use numerical quadrature in MATLAB, which is a low order method using an adaptive recursive Simpson's rule (similar results have been observed using the higher order adaptive Gauss/Lobatto quadrature rule). We also note here that we use a fully explicit version of Equation 3.3 with the LETIS method. An implicit version does not change the above formulation, except that a linear system solve is required and hence the computation is more expensive.

We set $\beta = 0$ to ensure that the method renders a divergence free velocity field, as is necessary for LETIS. Our finite volume interpretation of Equation 3.3 for $\beta = 0$ is

$$\begin{aligned} \mathcal{F}_{i+1/2,j} &= u_{i+1/2,j}\left(\frac{c_{i+1,j} + c_{i,j}}{2}\right) \\ &\quad - \frac{1}{h}\left[d_{i+1/2,j}^{11}(c_{i+1,j} - c_{i,j}) + \frac{1}{4}d_{i+1/2,j}^{12}(c_{i+1,j+1} + c_{i,j+1} - c_{i+1,j-1} - c_{i,j-1})\right], \\ \mathcal{G}_{i,j+1/2} &= v_{i,j+1/2}\left(\frac{c_{i,j+1} + c_{i,j}}{2}\right) \\ &\quad - \frac{1}{h}\left[d_{i,j+1/2}^{22}(c_{i,j+1} - c_{i,j}) + \frac{1}{4}d_{i,j+1/2}^{21}(c_{i+1,j+1} + c_{i+1,j} - c_{i-1,j+1} - c_{i-1,j})\right]. \end{aligned}$$

3.5 Assessing Grid Orientation Effects

Throughout this thesis various measures are used to assess the reduction in GOE by the developed methods. The first measure is a qualitative look at the front shape. This is the measure used in Figure 1.1. Unfortunately we have no analytic solution for these adverse mobility ratio flow problems. We can use physical reasoning to say qualitatively what the shape of the front should be, namely in the case of the quarter five-spot problem, we know that there should only be a single finger forming between in the injector and producer. Furthermore, a grid insensitive numerical method should produce the same solution regardless of the grid used. These sorts of qualitative statements hold for the homogeneous test problems in this work, but for heterogeneous problems, the rock properties determine preferential flow paths which may or may not be aligned with the grid. Heterogeneity also has the effect of reducing some of the bias in the numerical methods, especially as the flow paths become stronger. Hence for these problems in order to see the effects of the numerical errors, we will need to consider an ensemble average of many solution realizations. If a sufficiently large number of realizations is used, then the methods which are less grid sensitive will reveal this in the averaged solution front.

The next class of comparisons used to assess GOE is production well data, that is, data about the fluid present at the production wells at various times doing the simulation. The reason for considering this is that for a real reservoir, this is one of the types of data that we can measure and hence history match against. It is (almost) impossible, or at least prohibitively expensive, to actually measure the shape of the displacement front in a real reservoir. We will consider two different types of well data. The first type is for problems involving a single well (or set of identical wells). For these problems we use production curves, which is simply the time integrated amount of fluid that has been produced. For a grid insensitive method these curves should agree regardless of the type of grid used. Going back to Figure 1.1 the diagonal grid will result in a much larger production curve because oil will continue to be produced until the two fingers have broken through, whereas for the parallel grid once the single finger breaks through production will largely flatten off since the injected fluid will begin to be cycled (see Figure 3.10(b) for an example of this). The second class of well data we use is for problems which have multiple wells which are the same distance to the injector but not aligned with the same angles to the grid. For these tests we will instead look at data which pertains to each of the wells separately, namely we will look at the type of fluid being produced by each well. This type of data is called the water cut or gas to oil ratio depending on whether the injected fluid is water or gas. For a problem that has two production wells which are equidistant from the injection, these plots of the data for each of the wells should coincide if the method is grid independent. We only use the well data as a measure of GOE for homogeneous test problems.

3.6 Numerical Results

Figure 3.8 shows results for the well-sponge and LETIS methods for a mobility ratio of 30 and a grid density of 50×50 on the Cartesian grid and 71×71 on the parallel grid. The near-well radius is 0.1. The boundary of the near-well region is indicated by the quarter circle around the injection point. All simulations are shown at 0.4 pore volumes injected.

First we note, once again, that the unforced solutions in Figures 3.8(a) and 3.8(b) show strong grid dependencies. The parallel grid solution breaks through much earlier than the diagonal grid solution. The diagonal grid solution has split into two separate viscous fingers.

The well-sponge is very effective in reducing the grid orientation effect for SBAV with $\beta = 0$, as evident from Figure 3.8(c). However, the results for SPU, given in Figure 3.8(d), are not desirable. As shown before, SPU has much stronger directional diffusion and transport bias than SBAV, and hence it is to be expected that due to the underlying physical instability there will still be some grid orientation effects present. However, the extra two fingers on the diagonal SPU solution have decreased in size and the parallel SPU solution has widened slightly.

We see similar results to the well-sponge for the LETIS method. The results for SBAV with $\beta = 0$ are shown in Figure 3.8(e) and for SPU in Figure 3.8(f). The level of grid independence seen in the LETIS method is comparable with that of the well-sponge method; the LETIS method has the additional advantage of being conservative, which can be seen in Figure 3.9 which shows the volume of injected fluid versus the pore volumes injected.

We compare the production curves for the different methods in Figure 3.10. The curves for the well-sponge and LETIS are comparable with SBAV using $\beta = 0$. The physical instability of the problem is still very pronounced for SPU.

Figure 3.11 compares how for a mobility ratio of 20, SBAV results vary with refinement for both no forcing and the well-sponge. It is seen that the well-sponge method reduces the tendency of the numerical errors to trigger the instability. Since the instability is not removed by the forcing methods, the instability is triggered by numerical inaccuracies that appear at higher grid resolutions outside of the near-well region.

As a final test, we consider a three well problem that has been used in a number of papers as an alternative benchmark problem (Heinemann et al., 1991; Liu et al., 2007). The geometry consists of one injection well and two equidistant production wells. One production well is placed along one of the sets of grid lines, and the other is at 60° to it. Running simulations on this configuration with SPU results in significantly earlier breakthrough along the grid direction (Liu et al., 2007). Figures 3.12(a) and 3.12(b) show the saturation map and breakthrough curves for the LETIS scheme compared with no forcing; both simulations use SBAV with $\beta = 0$. The saturation fronts show significantly less grid bias for LETIS, and the breakthrough curves are much closer. In the simulation shown, there are 34 horizontal grid blocks from the injector to well 1 and 17 horizontal and 29 vertical grid blocks from the injector to well 2. Similar results are seen with the well-sponge

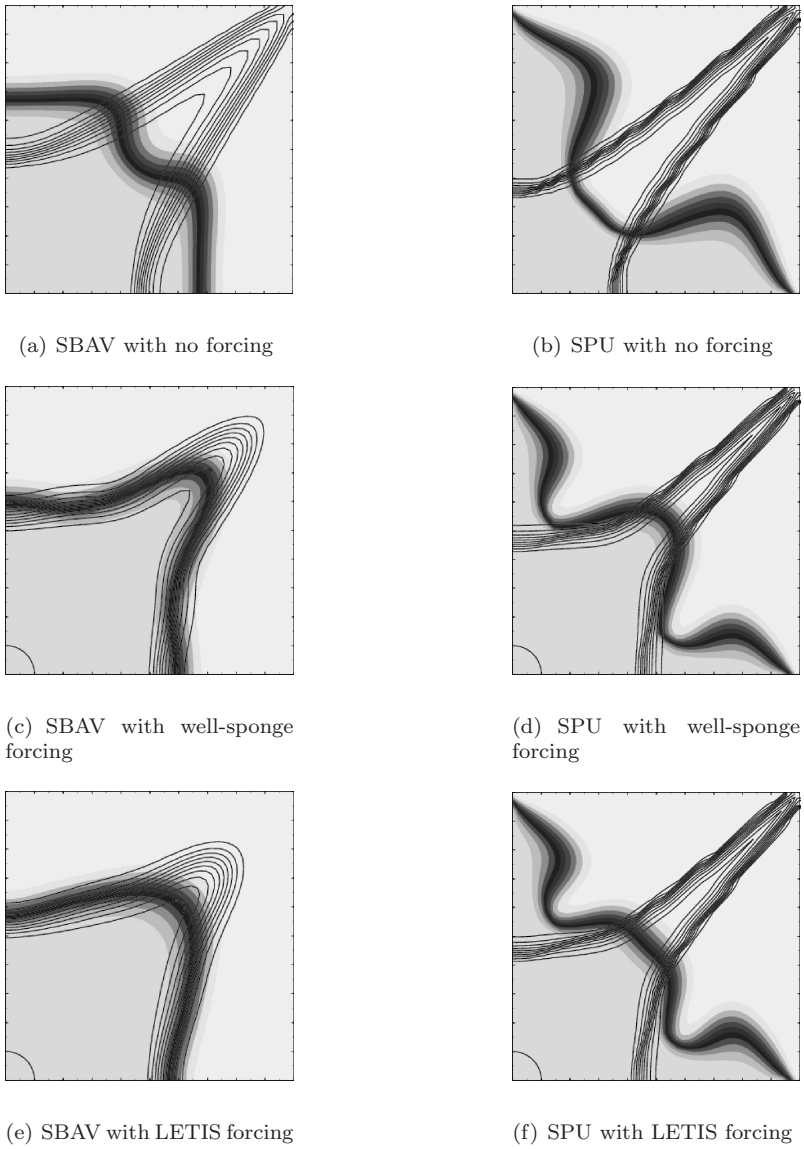

(a) SBAV with no forcing

(b) SPU with no forcing

(c) SBAV with well-sponge forcing

(d) SPU with well-sponge forcing

(e) SBAV with LETIS forcing

(f) SPU with LETIS forcing

Figure 3.8: Comparison of different forcing methods. All the simulations are run with a 50×50 diagonal grid (filled contours) and a 71×71 parallel grid (black contour lines). Mobility ratio is 30 and the near-well Peclet number of 400. The near-well region is $r_{nw} = 0.1$.

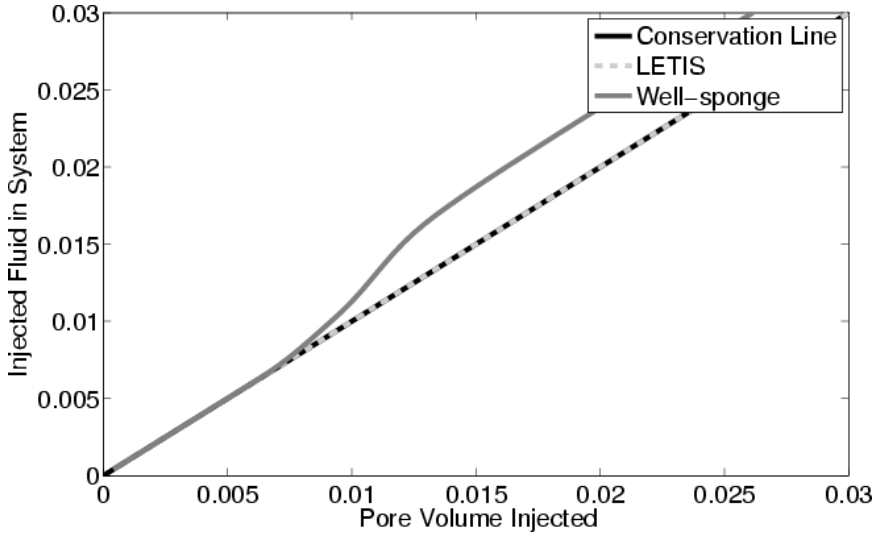

Figure 3.9: Volume of injected fluid in the reservoir versus pore volume injected. Exact conservation corresponds to the black line, which is a line of slope one. These reservoir volumes are from SBAV with a diagonal grid. Similar results are seen for all methods and grids.

method.

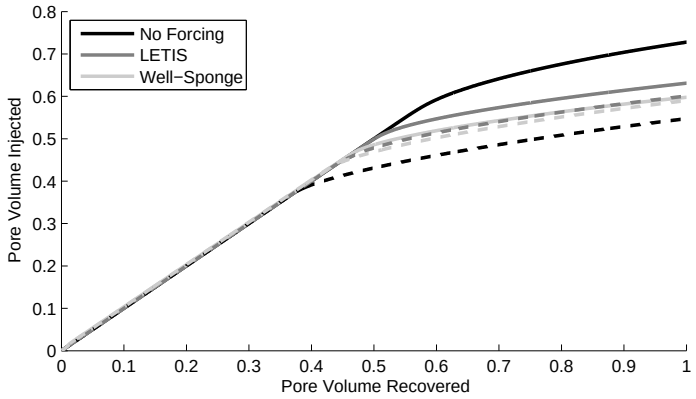

(a) Comparison of recovery for different well handling methods using SBAV transport method.

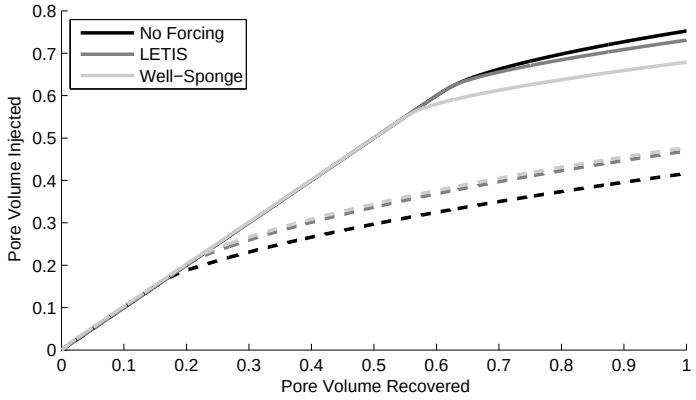

(b) Comparison of recovery for different well handling methods using SPU transport method.

Figure 3.10: Oil recovery of the various methods. The solid line of a given color is the diagonal grid solution and the dashed line the parallel grid solution.

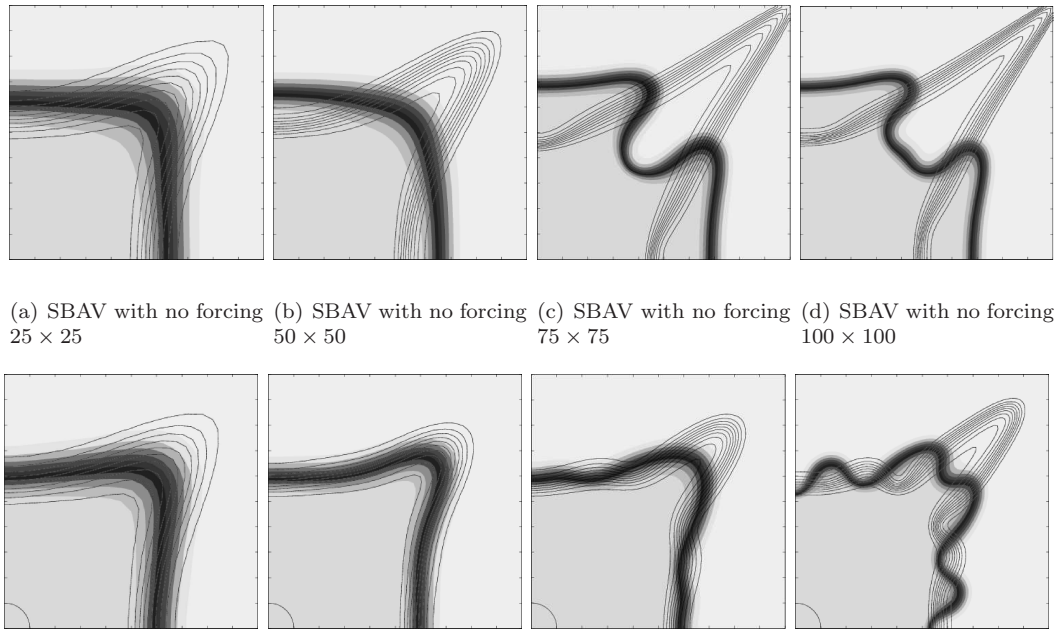

(a) SBAV with no forcing 25×25

(b) SBAV with no forcing 50×50

(c) SBAV with no forcing 75×75

(d) SBAV with no forcing 100×100

(e) SBAV with well-sponge forcing 25×25

(f) SBAV with well-sponge forcing 50×50

(g) SBAV with well-sponge forcing 75×75

(h) SBAV with well-sponge forcing 100×100

Figure 3.11: Mobility ratio of 20 grid refinement study for no forcing and well-sponge. As can be seen in these results, the well-sponge improves the stability region by extending the near-well region. Break down is still seen since the instability has not been remove completely but lessened in intensity.

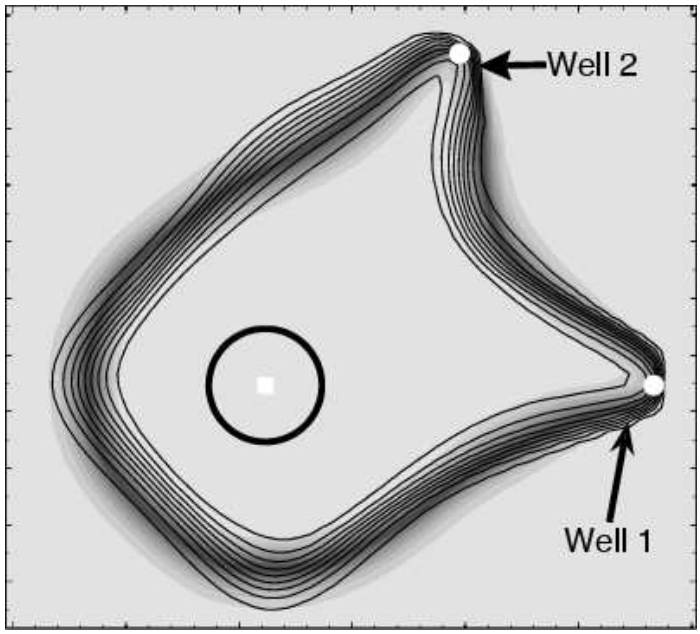

(a) saturation map

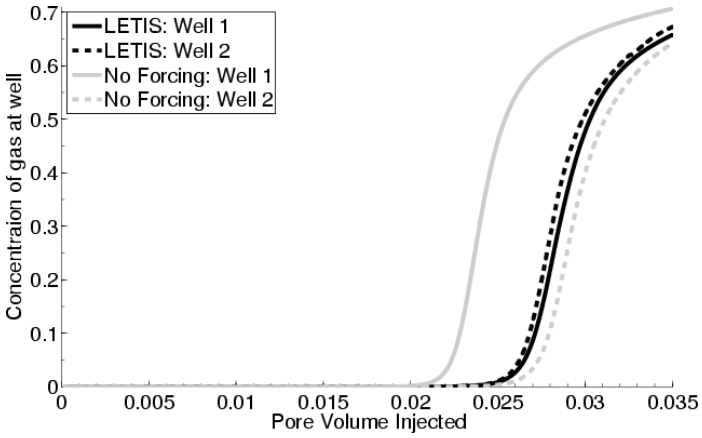

(b) breakthrough

Figure 3.12: Three well configuration test problem

Chapter 4

Multi-D Upstream Weighting

One of the advantages of SBAV, presented in chapter 3, is that it has an isotropic first order error term. This results in drastic reductions in GOE over SPU even without the forcing. There are however at least four drawbacks to SBAV which prevent it from being used in general purpose simulation. First, the pressure and transport discretizations are tightly coupled through the β factor, meaning that the method in its current form is not applicable to general pressure discretizations, such as multi-point flux approximations (Aavatsmark, 2002; Edwards and Rogers, 1998). Second, it is not clear how the method can be extended to general grids as the isotropic error term was developed for Cartesian grids. Thirdly, the benefit of SBAV over SPU is drastically reduced when generalized to heterogeneous permeability fields. For highly heterogeneous flow problems the averaging procedure used in the method must be changed from arithmetic to harmonic averaging so as to not result in diffusion into low permeability grid cells. This generalization reduces the impact of the diffusive correction and causes the scheme to closely resemble SPU. Finally, the method is not positive (meaning the updated solution is not a convex combination of the current solution). This property is desirable when using first order discretization methods for scalar transport problems because it guarantees a non-oscillatory concentration field. These shortcomings in SBAV lead to the next set of work, the development of more robust multi-D methods for transport.

4.1 Modified Equations Analysis

We begin by analyzing upwind finite difference discretizations for the constant velocity scalar transport equation

$$\frac{\partial c(x,y,t)}{\partial t} + \mathbf{u} \cdot \nabla c(x,y,t) = 0, \tag{4.1}$$

where $\mathbf{u} = (u,v)^T$ is constant in space and time. The exact solution to this equation is given by $c(x,y,t) = c_0(x-tu, y-tv)$, where $c_0(x,y) = c(x,y,t=0)$ is the initial condition. We define

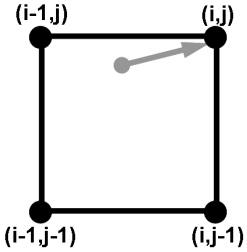

Figure 4.1: The four most physically relevant points for an upwind scheme for $u, v \geq 0$. The point of interpolation is found by tracing back along the velocity directions for a time step Δt.

the magnitude of the velocity as $\gamma \equiv \sqrt{u^2 + v^2}$, and the angle of the velocity with respect to the x-coordinate as $\theta \equiv \arctan(u/v)$. With these definitions, the velocity field can be expressed as

$$\mathbf{u} = \begin{bmatrix} u \\ v \end{bmatrix} = \gamma \begin{bmatrix} \cos\theta \\ \sin\theta \end{bmatrix}. \tag{4.2}$$

For simplicity, we assume a uniform Cartesian grid with step size h in both spatial directions and nodal grid values $C^n_{i,j} \approx c(x_i \equiv ih, y_j \equiv jh, t^n \equiv n\Delta t)$. An explicit finite difference update for $C^{n+1}_{i,j}$ can be written in the general form as

$$C^{n+1}_{i,j} = \sum_{k,l} \beta_{k,l} C^n_{i+k,j+l}, \tag{4.3}$$

with $\sum_{k,l} \beta_{k,l} = 1$. A sufficient condition for stability is to require that the updated solution be a convex combination of the previous solution (Roe and Sidilkover, 1992), that is,

$$\beta_{k,l} \geq 0. \tag{4.4}$$

This, known as the positivity requirement, ensures that no new extrema are introduced in the solution. It has been shown that such a linear, positive scheme can be at most first order accurate (LeVeque, 2003; Deconinck and Koren, 1997). For convergence, the scheme must also be a consistent discretization of 4.1, which positivity alone does not guarantee.

Assuming $u, v \geq 0$ the four most physically relevant concentrations surrounding cell (i, j) are $\{C^n_{i,j}, C^n_{i-1,j}, C^n_{i,j-1}, C^n_{i-1,j-1}\}$ (see Figure 4.1). Following Roe and Sidilkover (1992), it can be shown that there exists a single parameter family of consistent upwind schemes using these four points in

Common Name	κ	Interpolation	Time Step
Single Point Upstream (SPU) Weighting	$u+v$	Linear interpolation on $\{C^n_{i,j}, C^n_{i-1,j}, C^n_{i,j-1}\}$	$\Delta t \leq \frac{h}{u+v}$
Narrow Scheme (N-Scheme) (Roe and Sidilkover, 1992)	$\lvert u-v\rvert$	Linear interpolation on $\{C^n_{i,j}, C^n_{i-1,j}, C^n_{i-1,j-1}\}$ if $u \geq v$ or $\{C^n_{i,j}, C^n_{i,j-1}, C^n_{i-1,j-1}\}$ if $v \geq u$	$\Delta t \leq \frac{h}{\max(u,v)}$
Corner Transport Upwinding (CTU) (Colella, 1990)	$u+v-2\frac{\Delta t}{h}uv$	Bilinear interpolation on $\{C^n_{i,j}, C^n_{i-1,j}, C^n_{i,j-1}, C^n_{i-1,j-1}\}$	$\Delta t \leq \frac{h}{\max(u,v)}$
Koren's Scheme (1991)	$(u^2+v^2)/(u+v)$	Other first order interpolation	$\Delta t \leq \frac{h(u+v)}{u^2+uv+v^2}$

Table 4.1: Comparison of single parameter κ for four well known numerical methods (Roe and Sidilkover, 1992).

the form

$$C^{n+1}_{i,j} = C^n_{i,j} + \frac{\Delta t}{2h}\Big[(-u-v-\kappa)C^n_{i,j} + (u-v+\kappa)C^n_{i-1,j} + (u+v-\kappa)C^n_{i-1,j-1} + (v-u+\kappa)C^n_{i,j-1}\Big], \tag{4.5}$$

where the variable κ is a function of $\mathbf{u}$ and can be understood as defining an interpolation scheme on the four upwind points at the location $(x_i - \Delta t\, u, y_j - \Delta t\, v)$. In section 4.6 we will see that these schemes can be represented in conservative form, though there is no unique conservative formulation for a given κ (Roe and Sidilkover, 1992). For these schemes, the nonzero $\beta_{k,l}$ in Equation 4.3 are

$$\beta_{0,0} = 1 + \frac{\Delta t}{2h}(-u-v-\kappa), \qquad \beta_{-1,0} = \frac{\Delta t}{2h}(u-v+\kappa),$$
$$\beta_{-1,-1} = \frac{\Delta t}{2h}(u+v-\kappa), \qquad \beta_{0,-1} = \frac{\Delta t}{2h}(-u+v+\kappa).$$

Positivity then requires that

$$|u-v| \leq \kappa \leq u+v, \tag{4.6}$$
$$\Delta t \leq \frac{2h}{u+v+\kappa}. \tag{4.7}$$

The expression for κ for four common numerical discretizations and the corresponding time step restrictions are given in Table 4.1. The Narrow scheme (N-scheme), so called because it depends only on the "narrow" three points stencil $C_{i,j}$, $C_{i-1,j-1}$ and $C_{i-1,j}$ if $u \geq v$ or $C_{i,j-1}$ if $v \geq u$, has the least restrictive time step according to Equation 4.7 and Single Point Upstream (SPU) weighting,

also known as dimensional upwinding, the most restrictive. Although CTU is a popular scheme we will not consider it further in this work since for this scheme, κ depends on Δt Since κ depends on Δt for CTU it can reproduce the behavior of the other schemes for different time step sizes. However, in practical porous media problems time step sizes are dictated by global considerations and cannot be controlled locally. For this reason, CTU is not effective in eliminating GOE. For the miscible five-spot problem show in Figure 3.2 CTU gives results very similar to SPU.

As in section 3.2 we use modified equation analysis to understand how the errors introduced by the discretization affect the solution. For the family of schemes given by Equation 4.5, the modified equations are given by

$$c_t + uc_x + vc_y = \frac{h}{2}\left((u - \lambda\cos^2\theta)c_{xx} + (v - \lambda\sin^2\theta)c_{yy} + (u + v - \kappa - 2\lambda\cos\theta\sin\theta)c_{xy}\right) + \mathcal{O}(h^2), \tag{4.8}$$

where $\lambda = \Delta t\gamma/h$. Rotating the equations into the flow aligned coordinate system (s, n) gives the modified equation

$$\begin{aligned} c_t + \gamma c_s = &\underbrace{\gamma\frac{h}{2}\left[\sin\theta + \cos\theta - \tilde{\kappa}\sin\theta\cos\theta - \lambda\right]}_{d_{ss}} c_{ss} \\ &+ \underbrace{\gamma\frac{h}{2}\left[\tilde{\kappa}\sin\theta\cos\theta\right]}_{d_{nn}} c_{nn} \\ &+ \underbrace{\gamma\frac{h}{2}\left[\cos\theta - \sin\theta + \tilde{\kappa}(\sin^2\theta - \cos^2\theta)\right]}_{d_{sn}} c_{sn}, \end{aligned} \tag{4.9}$$

where $\tilde{\kappa} = \kappa/\gamma$. The coefficients d_{ss}, d_{nn} can be interpreted as longitudinal and transverse diffusion, respectively, and a nonzero mixed-term d_{sn} indicates that there is some rotation of the tensor relative to the streamline coordinates (Roe and Sidilkover, 1992; Van Ransbeeck and Hirsch, 1997). Equation 4.9 implies that if κ is independent of Δt then the time stepping error only affects the longitudinal diffusion. $\kappa(u, v) = 0$ results in a non-positive scheme with no transverse diffusion.

From Equations 4.6 and 4.9 it can be seen that the N-scheme has minimal transverse diffusion for the family of positive schemes, and SPU has maximal transverse diffusion. Plotting the magnitude of the diffusion coefficients versus the angle of the flow vector with respect to the grid helps to further assess the impact of the choice of κ. This is shown for SPU, the N-Scheme, and Koren's scheme in Figure 4.2. The plots clearly show that all three schemes have zero transverse diffusion for flow that is aligned with the grid, and in addition, the N-scheme has zero transverse diffusion at $\theta = \pi/4$. The diffusion tensor of Koren's scheme is flow aligned since $d_{sn} = 0$ for all θ. For a fixed time step SPU has the lowest longitudinal diffusion.

To further illustrate this behavior, a constant advection test is performed for SPU, the N-scheme, and Koren's scheme. Figure 4.3 displays the numerical results. Two time step criteria are tested: a

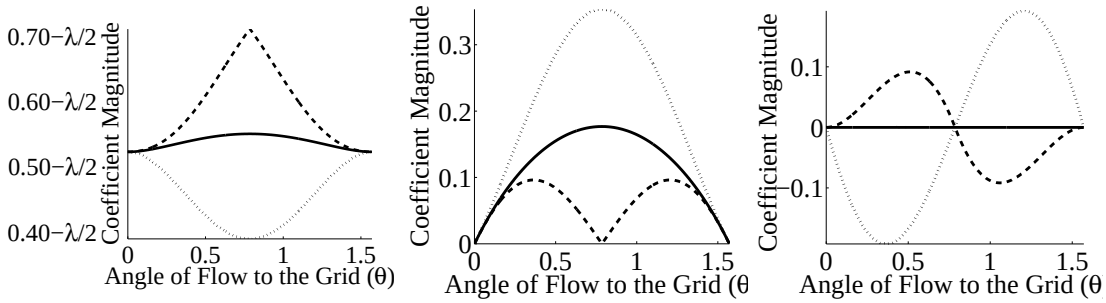

(a) Longitudinal (b) Transverse (c) Cross-term

Figure 4.2: The magnitude of diffusion coefficients in Equation 4.9 versus the angle of flow θ with respect to the x-coordinate for SPU, the N-scheme, and Koren's scheme. In these plots $h = 1$, $\gamma = 1$. The longitudinal coefficient depends on $\lambda/2$. The dotted line is SPU, the solid line is Koren's scheme, and the dashed line is the N-scheme.

fixed time step of $\Delta t = 0.75\sqrt{2}h/2$ (three quarters of the minimum maximal time step for SPU) and three quarters the maximum time step for each angle, $\Delta t = 0.75(2h/(u+v+\kappa))$. The domain is $\Omega = (-1,1)\times(-1,1)$ with 201×201 grid points, and the initial condition is $c_0(x,y) = \exp(-150(x^2+y^2))$. The solution is computed until $t_{\max} = 0.8$ using velocity field $\mathbf{u} = (\cos\theta, \sin\theta)^T$ for each $\theta = \{0, \pi/10, \pi/4, 7\pi/20, 9\pi/20\}$. The exact solution is $c(x,y,t_{\max}) = c_0(x - t_{\max}\cos\theta, y - t_{\max}\sin\theta)$, the translation of the initial condition along the characteristic.

The results in Figure 4.3 confirm the findings of the modified equation analysis: SPU has the smallest amount of longitudinal smearing for a fixed time step, the N-scheme the smallest amount of transverse smearing regardless of the time step, and Koren's scheme is always flow aligned. Comparing the fixed time step plots, Figures 4.3(a) - 4.3(c), with the maximal time step plots, Figures 4.3(d) - 4.3(f), shows that the change in time step mostly affects the longitudinal spreading. The transverse smearing remains relatively unchanged as predicted by Equation 4.9. Additional effects can be observed due to rotation and higher order terms which have been neglected in this analysis.

The above analysis can be extended to general structured grids. For unstructured grids a local analysis can be performed also, but global behavior is likely not predictable due to the changing nature of the error from one grid cell to the next.

4.2 Monotonicity and Framework Considerations

The analysis to this point has been limited to the constant velocity scalar transport problem. The schemes in the previous section can also be interpreted as finite volume methods. To robustly

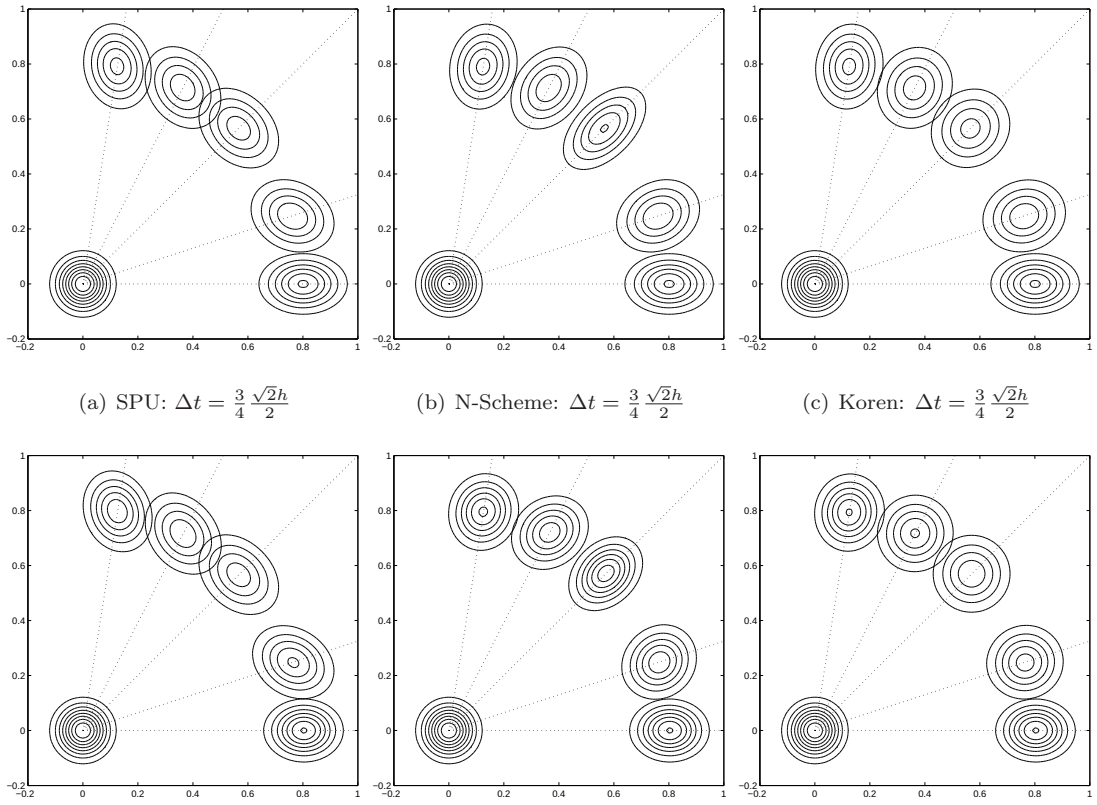

(a) SPU: $\Delta t = \frac{3}{4}\frac{\sqrt{2}h}{2}$ (b) N-Scheme: $\Delta t = \frac{3}{4}\frac{\sqrt{2}h}{2}$ (c) Koren: $\Delta t = \frac{3}{4}\frac{\sqrt{2}h}{2}$

(d) SPU: $\Delta t = \frac{3}{4}\frac{h}{u+v}$ (e) N-Scheme: $\Delta t = \frac{3}{4}\frac{h}{\max u,v}$ (f) Koren: $\Delta t = \frac{3}{4}\frac{h(u+v)}{u^2+uv+v^2}$

Figure 4.3: Constant advection tests for a Gaussian blob advected at different angles to the grid for SPU, the N-scheme, and Koren's scheme. Results for all angles are superimposed on the same plot. The time step criterion is given under each plot and $t_{\max} = 0.8$. Contours are shown for $c = 0.0, 0.1, \ldots, 1.0$.

and more easily extend these methods to general divergence free velocity fields and to nonlinear equations, we will utilize a finite volume framework. In this section we show how a general family of first order, truly multi-D finite volume schemes can be derived based on interaction regions. This family of schemes contains both the single parameter family from section 4.1, as will be seen in the next section, and also a wider class of schemes based on the full nine-point nearest neighbors stencil.

We develop the framework for a class of hyperbolic equations,

$$c_t + \nabla \cdot (\zeta(c)\boldsymbol{\sigma}) = q(c) \tag{4.10}$$

where $\zeta'(c) \geq 0$ (an extension to more general $\zeta(c)$ is given in section 4.7) and we assume that σ is

fixed during the transport solve. Both the miscible model in fractional flow form and the nonlinear model with gravity in the Darcy form can be represented in this manner. Namely, for the miscible model

$$\zeta(C) = C, \qquad \boldsymbol{\sigma} = -\frac{\boldsymbol{K}}{\mu(C)}\nabla p = \boldsymbol{u}_T,$$

hence the equation is a scalar transport equation. Though $\boldsymbol{\sigma}$ is not independent of C the total velocity field will be held fixed during the transport solve so $\boldsymbol{\sigma}$ can be thought of as independent of the transport solve. For the two phase model there will be a $\zeta_\alpha(C)$ and σ_α for each phase,

$$\zeta_\alpha(C) = \lambda(C) = \frac{k_{r,\alpha}(C)}{\mu_\alpha(C)},$$
$$\sigma_\alpha = -\boldsymbol{K}\nabla(p - \rho_\alpha g h).$$

Since we will require the discretization to be monotone only with respect to the phase being updated, the monotone methods developed here for Equation 4.10 will still be applicable. This will be discussed further in chapter 6. As noted in section 2.4 the fractional flow formulation could also be represented in this manner if gravitational forces are not present, but with gravitational forces this is not possible since $\boldsymbol{\sigma}$ would have to depend on C (see section 2.4). Throughout this chapter we will call $\zeta(c)$ the mobility function, even though it may not be, and c will be referred to as the mass variable.

Assume that we have a consistent discretization of Equation 4.10 of the form

$$C_i^{n+1} = \Phi_i^n(C_1^n, C_2^n, \ldots, C_N^n).$$

The discretization is called monotone if (Crandall and Majda, 1980)

$$\frac{\partial C_i^{n+1}}{\partial C_j^n} = \frac{\partial \Phi_i^n(C_1, C_2, \ldots, C_N)}{\partial C_j} \geq 0, \qquad \forall j. \tag{4.11}$$

where the arguments are taken in the range $C_k \in (a, b)$ for all k with a and b being the lower and upper bounds on the values that the mass variables can take. The schemes that we will consider actually take a simpler form, in that they will be of the form

$$C_i^{n+1} = C_i^n - \frac{\Delta t}{V_i}\sum_j \Phi_{ij}^n \zeta(C)_j^n,$$

where V_i is the volume or area of cell i. Hence our methods will be monotone if

$$\begin{aligned} \Phi^n_{i,j}\zeta'(C_j) &\le 0, \qquad \text{for } j \neq i, \\ \zeta'(C_i)\frac{\Delta t}{V_i}\Phi^n_{i,i} &\le 1, \end{aligned}$$

hence we have the time step constraint

$$\Delta t \le \frac{V_i}{\Phi^n_{i,i}\max_{c\in(a,b)}\zeta'(c)}, \qquad \forall\ i.$$

In the case of scalar transport, where $\zeta(C) = C$, then

$$\begin{aligned} C^{n+1}_i &= C^n_i - \frac{\Delta t}{V_i}\sum_j \Phi^n_{ij}C = \sum_j \beta_{i,j}C, \\ \beta_{i,j} &= -\Phi_{i,j}, \qquad j \neq i, \\ \beta_{i,i} &= 1 - \Phi_{i,i}, \end{aligned}$$

and one of the constraints imposed by consistency is that $\sum_j \beta_{i,j} = 1$. The monotonicity constraints become

$$\begin{aligned} \Phi^n_{i,j} &\le 0, \qquad \text{for } j \neq i, \\ \frac{\Delta t}{V_i}\Phi^n_{i,i} &\ge 1, \end{aligned}$$

hence we have that $\beta_{i,j} \ge 0$ as in Equation 4.4. This shows that for scalar problems within this methodology, monotonicity implies positivity.

We now define the general finite volume framework used for transport. Let $\boldsymbol{C}^n$ be the vector of all the grid mass variables at time t^n and $\boldsymbol{\sigma}$ be the vector of all the face based σ variables. The numerical fluxes can be written as the vector

$$\boldsymbol{\mathcal{F}} = \boldsymbol{\sigma} \bullet [\boldsymbol{R}\zeta(\boldsymbol{C})] = \boldsymbol{\sigma} \bullet \bar{\boldsymbol{\zeta}}, \tag{4.12}$$

where $\boldsymbol{R}$ is a yet to be defined stencil matrix that defines face based mobility values $\bar{\boldsymbol{\zeta}}$ from the cell-based mobilities $\zeta(\boldsymbol{C})$. Component by component vector multiplication is denoted by $\bullet$. If $\boldsymbol{Div}$ is a divergence matrix, then our finite volume discretization can be written as

$$\boldsymbol{C}^{n+1} = \boldsymbol{C}^n - \Delta t \boldsymbol{V}^{-1}\left(\boldsymbol{Div}\left(\boldsymbol{\sigma} \bullet \bar{\boldsymbol{\zeta}}\right) - \boldsymbol{Q}^n\right)$$

where $\boldsymbol{V}$ is a diagonal matrix of cell volumes and $\boldsymbol{Q}^n$ is the vector of source terms.

To maintain monotonicity, the coefficients that determine the fluxes are required to satisfy constraints. These constraints introduce a coupling in the flux calculations. This can be understood by considering a 1-D example. Assume that we have a finite volume update for C_i^{n+1} given as

$$C_i^{n+1} = C_i^n - \frac{\Delta t}{h}\left(\mathcal{F}_{i+1/2} - \mathcal{F}_{i-1/2}\right).$$

We assume that $\mathcal{F}_{i+1/2}$ and $\mathcal{F}_{i-1/2}$ both have some dependence on C_j^n, for example $\mathcal{F}_{i+1/2}$ is an increasing function of C_j^n and $\mathcal{F}_{i-1/2}$ a decreasing function. For monotonicity we need

$$\frac{\partial C_i^{n+1}}{\partial C_j^n} = -\frac{\Delta t}{h}\left(\frac{\partial \mathcal{F}_{i+1/2}}{\partial C_j^n} - \frac{\partial \mathcal{F}_{i-1/2}}{\partial C_j^n}\right) \geq 0.$$

Since $\frac{\partial \mathcal{F}_{i+1/2}}{\partial C_j^n} > 0$ and $\frac{\partial \mathcal{F}_{i-1/2}}{\partial C_j^n} < 0$, it follows that the calculation of the fluxes is coupled. A similar coupling would occur between $\mathcal{F}_{i+3/2}$ and $\mathcal{F}_{i+1/2}$ and so on. Hence, there is a potential global coupling in the calculation of all the fluxes: modifying one flux can affect the monotonicity of other cell updates. For SPU this coupling is also present but is manifest as a time step constraint, which is the case for all schemes that only depend on direct neighbors. For multi-D schemes there are more fluxes to consider, but the general concept is the same.

Resolving a global coupling is possible, but solving a large system of equations at each time step is not desirable for explicit discretization of hyperbolic equations as they often require small time steps for stability and/or accurate transient behavior and have a finite domain of dependence. The flux dependence can be localized by a limiting strategy (Lamine and Edwards, 2008), but in order to preserve the multi-D nature of the schemes, especially in rough velocity fields, it is more convenient to introduce a local coupling through interaction regions, which have been extensively used in multi-point flux approximation methods (Aavatsmark, 2002; Edwards and Rogers, 1998).

4.3 Interaction Region Definitions

Here we discuss how interaction regions are defined for Cartesian grids, though it should be noted that much of the work that follows applies to general grid topologies. In particular, the scheme definitions and the proof of monotonicity presented in the next section are grid topology independent. As illustrated in Figure 4.4, interaction regions form a dual grid whose grid lines connect cell centers and face centers, the dotted lines in the figure.

Each Cartesian interior grid cell (i, j) is part of four interaction regions. We label the local interaction regions with superscript $m = 1, 2, 3, 4$, counterclockwise from the bottom left corner of cell (i, j), as illustrated in Figure 4.4(b). We denote the four grid cell segments (subcells) that make up each interaction region, with subscript $p = 1, 2, 3, 4$, counterclockwise starting in the lower left

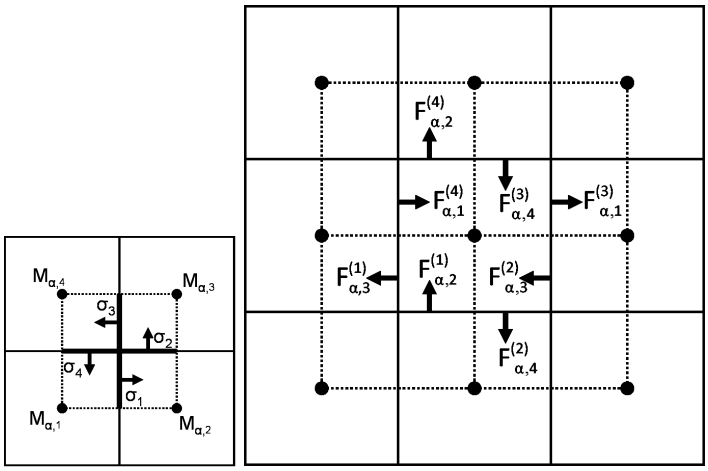

(a) Single interaction region (b) All interaction regions for cell (i, j)

Figure 4.4: Pictorial view of an interaction region. The vectors represent the direction defined to be positive.

subcell (Figure 4.4(a)). Similarly, the half-faces in each interaction region are numbered counter-clockwise from $p = 1, 2, 3, 4$ starting with the bottom most half-face. Then, $C_p^{(m)}$ denotes the average mass in subcell p of interaction region m. The cell averaged quantities are

$$C_{i,j} = C_3^{(1)} = C_4^{(2)} = C_1^{(3)} = C_2^{(4)},$$

and face-based values are

$$\sigma_{i-1/2,j} = -\sigma_3^{(1)} + \sigma_1^{(4)}, \qquad \sigma_{i+1/2,j} = -\sigma_3^{(2)} + \sigma_1^{(3)},$$
$$\sigma_{i,j-1/2} = \sigma_2^{(1)} - \sigma_4^{(2)}, \qquad \sigma_{i,j+1/2} = \sigma_2^{(4)} - \sigma_4^{(3)},$$

where $(i+1/2, j)$ denotes the face between cell (i, j) and $(i+1, j)$, and similarly for the other faces. For our work $\boldsymbol{\sigma}$ is determined by a two-point flux approximation and therefore

$$\frac{\sigma_{i-1/2,j}}{2} = \sigma_1^{(4)} = -\sigma_3^{(1)}.$$

For more general MPFA methods this would not necessarily be the case.

In general, depending on the local grid topology, there may be more or fewer subcells and half-faces per interaction region, but the setup is the same. One of the properties of interaction regions

is that no matter the grid topology, the number of subcells and half-faces in an interaction region is always the same. We denote this number for interaction region (m) as $n_{ir}^{(m)}$. Also, each grid cell always belongs to as many interaction regions as it has faces. If the positive direction of the vectors in an interaction region are defined in the counterclockwise direction, all the results that follow also hold for general grid topologies.

4.4 Local Monotonicity Constraints for Interaction Regions

For a Cartesian grid, the mass in cell (i, j) is updated according to

$$C_{i,j}^{n+1} = C_{i,j}^{n} - \frac{\Delta t}{h}\left(\mathcal{F}_3^{(1)} - \mathcal{F}_2^{(1)} + \mathcal{F}_4^{(2)} - \mathcal{F}_3^{(2)} + \mathcal{F}_1^{(3)} - \mathcal{F}_4^{(3)} + \mathcal{F}_2^{(4)} - \mathcal{F}_1^{(4)}\right).$$

By defining the subcell accumulation term $\varphi_k^{(m)} = \mathcal{F}_k^{(m)} - \mathcal{F}_{k-1}^{(m)}$, the update can be written as

$$C_{i,j}^{n+1} = C_{i,j}^{n} - \sum_{k=1}^{4} \frac{\Delta t}{h^2} \varphi_k^{(k-2)}, \tag{4.13}$$

where plus and minus for interaction region superscripts and subscripts are defined cyclically on the set $\{1, 2, 3, 4\}$. For monotonicity, Equation 4.11, it is sufficient to require that

$$0 \leq \frac{\partial \varphi_k^{(k-2)}}{\partial C_{l\neq k}^{(k-2)}}, \tag{4.14}$$

$$1 \leq \frac{\Delta t}{h^2}\left[\sum_{k=1}^{4} \frac{\partial \varphi_k^{(k-2)}}{\partial C_k^{(k-2)}}\right]. \tag{4.15}$$

The constraint given by Equation 4.14 only includes subcells of interaction region $(k-2)$, that is, it is only a local coupling. This demonstrates the attraction of interaction regions because a potential global coupling has been reduced to a local interaction region coupling. Equation 4.15, on the other hand, involves all interaction regions that cell (i, j) belongs to and imposes a global time step constraint on the problem, as would be present in any explicit transport method. Hence we can calculate all the fluxes $\mathcal{F}_p^{(m)}$ for a cell such that they satisfy the local constraint of Equation 4.14 and then choose a time step Δt that satisfies Equation 4.15 for all the cells (i, j) of the grid. For general grid topologies the same equations hold with appropriate adjustments of the number of terms in the update and constraints.

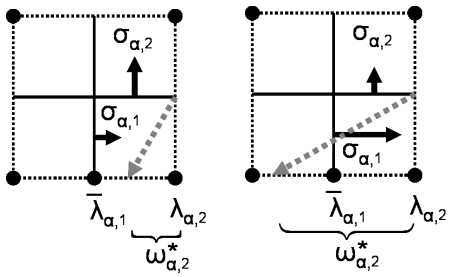

(a) (b)

Figure 4.5: Pictorial view of the traceback ω_2^* and $\bar{\zeta}_2$ assuming that $\sigma_1 > 0$ and $\sigma_2 > 0$

4.5 Multi-D Mobility Weighting

Since we have shown that we only need a local coupling, we drop the superscript notation (m) denoting interaction region number. Stencil matrix $\boldsymbol{R}$ now only applies to a single interaction region. The vector $\boldsymbol{\zeta}$ also refers to the subcell values of the interaction region. As noted in the previous section, we are searching for methods of the form

$$\boldsymbol{\mathcal{F}} = \bar{\boldsymbol{\zeta}} \bullet \boldsymbol{\sigma}, \tag{4.16}$$

where

$$\bar{\boldsymbol{\zeta}} = \boldsymbol{R}\boldsymbol{\zeta}.$$

Again, we assume that $\zeta(C)$ is non-decreasing in C. By making this assumption we can define the upwind direction from the sign of σ for a face without considering the derivative of $\zeta(C)$. The face-based mobilities are defined as

$$\bar{\zeta}_k = \begin{cases} (1-\omega_k)\zeta_k \quad + \omega_k \bar{\zeta}_{k-1}, & \text{if } \sigma_k \geq 0 \\ (1-\omega_k)\zeta_{k+1} + \omega_k \bar{\zeta}_{k+1}, & \text{otherwise} \end{cases}, \tag{4.17}$$

where ω_k is a yet to be defined interpolation parameter. In other words, we take a face mobility to be a combination of the upwind subcell mobility and the upwind face mobility. Physically this means that some of the fluid flowing through an interaction region half-face came from the upwind subcell and some came from the other the half-face of the subcell, see Figure 4.5. The multi-D character of the scheme is dictated by the interpolation parameter ω_k. If we let $\omega_k = 0$, we get single point upstream weighting. We require the interpolation parameter to satisfy $0 \leq \omega_k \leq 1$, and it will also

be constrained by the amount of fluid flowing in and out of the subcell. The traceback defined by σ_k and the upwind phase flux, Figure 4.5, as

$$\omega_k^* = \begin{cases} \max(0, \sigma_{k-1}/\sigma_k), & \text{if } \sigma_k > 0 \\ \max(0, \sigma_{k+1}/\sigma_k), & \text{if } \sigma_k < 0 \\ 0, & \text{if } \sigma_j = 0 \end{cases}. \tag{4.18}$$

We defined the interpolation parameter by the limiting function $\omega_k = \omega(\omega_k^*)$, where the limiting function has the property $0 \leq \omega(\omega_k^*) \leq \min(1, \omega_k^*)$. As we will see, this property is necessary for the scheme to be monotone.

Finally, we arrive at the following linear system of equations derived from Equation 4.17

$$\boldsymbol{A}\bar{\boldsymbol{\zeta}} = \boldsymbol{B}\boldsymbol{\zeta}, \tag{4.19}$$

and hence

$$\boldsymbol{R} = \boldsymbol{A}^{-1}\boldsymbol{B}.$$

The matrix $\boldsymbol{A}$ represents the local coupling over the interaction region and is an M-matrix with diagonal elements $a_{i,i} = 1$ and off-diagonals

$$a_{i,i+1} = \begin{cases} -\omega_i, & \text{if } \sigma_i < 0 \\ 0, & \text{if } \sigma_j \geq 0 \end{cases},$$

$$a_{i,i-1} = \begin{cases} 0, & \text{if } \sigma_i < 0 \\ -\omega_i, & \text{if } \sigma_i \geq 0 \end{cases},$$

$$a_{i,j} = 0, \qquad j \neq i,\ i+1,\ i-1.$$

In the above, $i \pm 1$ is defined cyclically on the set $\{1, 2, \ldots, n_{ir}\}$. For A to be nonsingular we must have $\omega_j < 1$ for at least one $j \in \{1, 2, \ldots, n_{ir}\}$. In practice this is not a large restriction because if $\omega_j = 1$ for all $j \in \{1, 2, \ldots, n_{ir}\}$ then $\sigma_1 = \sigma_2 = \cdots = \sigma_{n_{ir}}$ which is unlikely. The matrix $\boldsymbol{B}$ is

nonnegative,

$$b_{i,i+1} = \begin{cases} 1-\omega_i, & \text{if } \sigma_i < 0 \\ 0, & \text{if } \sigma_j \geq 0 \end{cases},$$
$$b_{i,i} = \begin{cases} 0, & \text{if } \sigma_i < 0 \\ 1-\omega_i, & \text{if } \sigma_i \geq 0 \end{cases},$$
$$b_{i,j} = 0, \qquad j \neq i \pm 1,$$

where $i+1$ is again defined in a cyclic manner. This means that $\boldsymbol{R} = \boldsymbol{A}^{-1}\boldsymbol{B}$ is a nonnegative matrix, and $\bar{\zeta}_k = \sum_{j=1}^{n_{ir}} r_{k,j}\zeta_j$ where $r_{k,j} \geq 0$ are the elements of $\boldsymbol{R}$.

Theorem 1. *Given the following assumptions:*

- *non-negative discrete masses,* $C^n \geq 0$
- *flux expressions for the interaction regions satisfying Equation 4.16,* $\mathcal{F} = \bar{\zeta} \bullet \sigma$
- $\bar{\zeta}$ *defined by Equations 4.17*
- $\zeta'(C) \geq 0$ *(a non-decreasing function of* C*)*
- *an interpolation parameter* $\omega = \omega(\omega^*)$ *with* ω^* *defined by 4.18 and* $0 \leq \omega(\omega^*) \leq \min(1, \omega^*)$
- $\omega_l < 1$ *for at least one* $l \in \{1, 2, \ldots, n_{ir}\}$

then the defined scheme satisfies monotonicity constraint of Equation 4.14,

$$0 \geq \frac{\partial \varphi_k}{\partial C_{j \neq k}},$$

where $\varphi_k = \mathcal{F}_k - \mathcal{F}_{k-1}$.

Proof. We will prove the theorem for subcell k and need to consider three cases: (1) $\sigma_k \leq 0$ and $\sigma_{k-1} \geq 0$, (2)$\sigma_k \geq 0$ and $\sigma_{k-1} \leq 0$ and (3) $\sigma_k \geq 0$ and $\sigma_{k-1} \geq 0$. (The case $\sigma_k \leq 0$ and $\sigma_{k-1} \leq 0$ is handled by symmetry.) To satisfy Equation 4.14 we need to show that for each of these cases $\frac{\partial \varphi_k}{\partial C_j} \leq 0$.

1. $\sigma_k \leq 0$ and $\sigma_{k-1} \geq 0$:
   The accumulation term is

$$\begin{aligned} \varphi_k &= \mathcal{F}_k - \mathcal{F}_{k-1} \\ &= \sigma_k \bar{\zeta}_k - \sigma_{k-1}\bar{\zeta}_{k-1} \\ &= \sum_{j=1}^{n_{ir}} \left(\sigma_k r_{k,j} - \sigma_{k-1} r_{k,j}\right) \zeta_j. \end{aligned}$$

The derivative of this with respect to $C_{j\neq k}$ is

$$\frac{\partial \varphi_k}{\partial C_j} = \left(\sigma_k r_{k,j} - \sigma_{k-1} r_{k-1,j}\right) \zeta'(C_j),$$

where $(\sigma_k r_{k,j} - \sigma_{k-1} r_{k,j}) \leq 0$ by the properties of the stencil matrix and sign assumptions on σ_k and σ_{k-1}, and $\zeta'(C_j) > 0$ by assumption. Hence overall $\frac{\partial \varphi_k}{\partial C_j} \leq 0$.

2. $\sigma_k \geq 0$ and $\sigma_{k-1} \leq 0$:
   The accumulation term is

$$\begin{aligned}
\varphi_k &= \mathcal{F}_k - \mathcal{F}_{k-1} \\
&= \sigma_k \bar{\zeta}_k - \sigma_{k-1} \bar{\zeta}_{k-1} \\
&= \sigma_k \zeta_k - \sigma_{k-1} \zeta_k,
\end{aligned}$$

   so $\frac{\partial \varphi_k}{\partial C_j} = 0$ for $C_{j\neq k}$.

3. $\sigma_k \geq 0$ and $\sigma_{k-1} \geq 0$:
   The upstream subcell of face k is subcell k and the upstream half-face is $k-1$ (similar to Figure 4.5) so the accumulation term for subcell k is

$$\begin{aligned}
\varphi_k &= \mathcal{F}_k - \mathcal{F}_{k-1} \\
&= \sigma_k \bar{\zeta}_k - \sigma_{k-1} \bar{\zeta}_{k-1} \\
&= \sigma_k \left((1-\omega_k)\zeta_k + \omega_k \bar{\zeta}_{k-1}\right) - \sigma_{k-1} \bar{\zeta}_{k-1} \\
&= \sigma_k (1-\omega_k)\zeta_k - \left(\sigma_{k-1} - \sigma_k \omega_k\right) \bar{\zeta}_{k-1} \\
&= \sigma_k (1-\omega_k)\zeta_k - \left(\sigma_{k-1} - \sigma_k \omega_k\right) \sum_{j=1}^{n_{ir}} r_{k-1,j} \zeta_j.
\end{aligned}$$

   We have

$$\sigma_{k-1} - \sigma_k \omega_k \geq \sigma_{k-1} - \sigma_k \frac{\sigma_{k-1}}{\sigma_k} = 0,$$

   by the properties of the limiter function $\omega_k = \omega(\omega_k^*)$ and the definition of ω_k^* in Equation 4.18. Taking the derivative of φ_k with respect to $C_{j\neq k}$ gives

$$\frac{\partial \varphi_k}{\partial C_j} = -\left(\sigma_{k-1} - \sigma_k \omega_k\right) r_{k-1,j} \zeta'(C_j)$$

   where all the terms are positive, so overall $\frac{\partial \varphi_k}{\partial C_j} \leq 0$.

□

The above theorem is for subcell values, but due to Equations 4.14, it applies to the underlying

global computation grid. We have shown that a grid cell (i,j) is monotone with respect to all the other cells $(k,l) \neq (i,j)$. For the update, or discretization, to be monotone we also need it to be monotone with respect to its own cell (i,j). This comes in the form of the time step constraint, Equation 4.15,

$$1 \geq \frac{\Delta t}{h^2}\left[\sum_{k=1}^{4} \frac{\partial \varphi_k^{(k-2)}}{\partial C_k^{(k-2)}}\right], \tag{4.20}$$

where $\varphi_k^{(k-2)} = \mathcal{F}_k^{(k-1)} - \mathcal{F}_{k-1}^{(k-1)}$. We can write

$$\begin{aligned}\frac{\partial \varphi_k^{(k-2)}}{\partial C_k^{(k-2)}} &= \frac{\partial}{\partial C_k^{(k-2)}}\left(\sum_{i=1}^{n_{ir}}\left(c_{k,i}^{(k-2)}\sigma_k^{(k-2)} - c_{k-1,i}^{(k-2)}\sigma_{k-1}^{(k-2)}\right)\zeta\left(C^{(k-2)}\right)\right) \\ &= (c_{k,k}^{(k-2)}\sigma_k^{(k-2)} - c_{k,k-1}^{(k-2)}\sigma_{k-1}^{(k-2)})\zeta'\left(C_k^{(k-2)}\right).\end{aligned}$$

4.5.1 Derivative of Mobility Weighting

In chapter 6, subsection 6.1.4, we will need the derivative of $\bar{\boldsymbol{\zeta}}$ with respect to the pressure variables. We can efficiently construct these values over the interaction region using the matrices and factors that have already been computed. Taking the derivative of $\bar{\zeta}_k$, Equation 4.17, with respect to p_j, the pressure of subcell j, we get

$$\begin{aligned}\frac{\partial \bar{\zeta}_k}{\partial p_j} &= -\frac{\partial \omega_k}{\partial p_j}\zeta(S_k) + \frac{\partial \omega_k}{\partial p_j}\bar{\zeta}_{k-1} + \omega_k\frac{\partial \bar{\zeta}_{k-1}}{\partial p_j}, \\ \frac{\partial \omega(\omega_k^*)}{\partial p_j} &= \omega'(\omega_k^*)\frac{\partial \omega_k^*}{\partial p_j}, \\ \frac{\partial \omega_k^*}{\partial p_j} &= \begin{cases}\left(\sigma_k t_{k-1,j} - t_{k,j}\sigma_{k-1}\right)/\sigma_k^2 & \text{if } \omega_k^* > 0 \\ 0 & \text{otherwise}\end{cases},\end{aligned} \tag{4.21}$$

where t_{ij} is element (i,j) of the interaction region transmissibility matrix $\boldsymbol{T}$ ($\boldsymbol{\sigma} = \tan T(\boldsymbol{p} - g\rho\boldsymbol{H})$, see chapter 6), and we have assumed that $\sigma_k > 0$; the other case is similar. Equation 4.21 can be written as

$$\boldsymbol{A}\frac{\partial \bar{\boldsymbol{\zeta}}}{\partial \boldsymbol{p}} = \boldsymbol{D}_{\zeta}\boldsymbol{\zeta} + \boldsymbol{D}_{\bar{\zeta}}\bar{\boldsymbol{\zeta}},$$

where $\boldsymbol{A}$ is the same matrix as was computed in Equation 4.19. Thus the same linear system needs to be solved with a new right hand side.

4.6 Definition of Select Interaction Region Based Schemes

The final matter that we must consider is how to construct the limiter $\omega(x)$. In section 4.1 we analyzed three constant velocity scalar advection methods: SPU, Narrow Scheme (N-scheme) (Roe

and Sidilkover, 1992), and Koren's (1991) Scheme. These methods inspire three limiters

$$\omega_{\text{SPU}}(x) = 0, \qquad \omega'_{\text{SPU}}(x) = 0 \tag{4.22}$$

$$\omega_{\text{TMU}}(x) = min(1, x), \qquad \omega'_{\text{TMU}}(x) = \begin{cases} 1, & 0 \le x \le 1 \\ 0, & otherwise \end{cases} \tag{4.23}$$

$$\omega_{\text{SMU}}(x) = \frac{x}{1+x}, \qquad \omega'_{\text{SMU}}(x) = \frac{1}{(1+x)^2} \tag{4.24}$$

where TMU, or tight multi-D upstream limiting, corresponds to the N-scheme when applied to the constant velocity scalar advection problem and SMU, or smooth multi-D upstream limiting, corresponds to Koren's scheme.

Here we note that SPU and TMU are limiting members of this family of schemes. SPU being the lower limit and TMU the upper limit. SMU, on the other hand, is an interior method which results in smoother interpolation parameters. Other methods are possible within this family, namely any method for scalar advection that is of the single parameter family described in section 4.1, Equation 4.5 is expressible, where κ is

$$\kappa = u\left(1 - \omega\left(\frac{u}{v}\right)\right) + v\left(1 - \omega\left(\frac{v}{u}\right)\right).$$

4.7 Handling General Mobility Functions

Here we will generalize the design of multi-D upwind schemes to more general flux functions. This will allow us to consider partially miscible flows in addition to immiscible flows covered by the formulation previously presented. Still working within the interaction region framework we define $f_i(C) = \sigma_i \zeta(C)$ and the upwind state C_i^* to be such that

$$\mathcal{F}_i^* = f_i(C_i^*) = \begin{cases} \max_{C_i \le c \le C_{i+1}} f_i(c), & \text{if } C_i \le C_{i+1} \\ \max_{C_{i+1} \le c \le C_i} f_i(c), & \text{if } C_i > C_{i+1} \end{cases},$$

where this upwind state has the property that

$$C_i^* = \begin{cases} C_i, & \text{if } f_i'(C_i^*) \ge 0 \\ C_{i+1}, & \text{if } f_i'(C_i^*) \le 0 \\ C_s, & \text{if } f_i'(C_i^*) = 0 \end{cases}.$$

The point C_s is such that $f_i'(C_s) = 0$ (there may be more than one such value). The mobility functions considered in previous sections were such that $\zeta'(C) \ge 0$. This meant that the flux function $f(C) = \sigma\zeta(C)$ was a nondecreasing function of C if $\sigma \ge 0$ and non-increasing if $\sigma < 0$, so

we were able to determine the upwind state by only considering the sign of σ.

The multi-D mobility weighting is then defined as

$$\bar{\zeta}_i = \begin{cases} (1-\omega_i)\zeta_i - \omega_i\bar{\zeta}_{i-1}, & \text{if } f_i'(C_i^*) > 0,\ f_{i+1}'(C_{i-1}^*) > 0 \\ (1-\omega_i)\zeta_{i+1} - \omega_i\bar{\zeta}_{i+1}, & \text{if } f_i'(C_i^*) < 0,\ f_{i+1}'(C_{i+1}^*) < 0 \\ \zeta(C_i^*), & \text{otherwise} \end{cases},$$

where ω_i^* is now defined as

$$\omega_i^* = \begin{cases} \max\left(0, \frac{\sigma_{i-1}}{\sigma_i}\right), & \text{if } f_i'(C_i^*) > 0,\ f_{i+1}'(C_{i-1}^*) > 0 \\ \max\left(0, \frac{\sigma_{i+1}}{\sigma_i}\right), & \text{if } f_i'(C_i^*) < 0,\ f_{i+1}'(C_{i+1}^*) < 0 \\ 0, & \text{otherwise} \end{cases}.$$

The proof to show that this method is monotone is a straightforward extension of the proof of Theorem 1 and is shown in Appendix B.

The method can be applied to any nonlinear partial differential equation of the form

$$C_t + \nabla \cdot \begin{bmatrix} f(C) \\ g(C) \end{bmatrix} = 0,$$

if $f'(C)/g'(C) = \beta$, where β is independent of C. For the nonlinear problems in this thesis, $(f(C), g(C))^T = \zeta(C)(\sigma_x, \sigma_y)^T$ so then $\beta = \sigma_x/\sigma_y$.

4.8 Constant Transverse Diffusion Scheme

As we will see in chapter 5 the N-scheme, or TMU, drastically reduces GOE as compared with SPU for miscible gas injection. This can be attributed to the fact that the N-scheme has minimal transverse diffusion over all linear positive schemes for scalar advection. An optimal first order scheme might be defined as having zero transverse diffusion for all flow angles however to achieve this it would be necessary to give up the desired positivity of the scheme. Nonetheless, we can construct a scheme with a minimal amount of constant transverse diffusion. Starting with the N-scheme as a base method, we add a first order diffusive correction so that the resultant scheme has constant transverse diffusion at the same level as the maximum transverse diffusion value of the N-scheme. This constant amount of transverse diffusion is the minimal amount necessary to construct a positive scheme. This method is only developed and used for scalar advection.

The N-scheme corresponds to $\kappa = |u - v| = \gamma|\cos\theta - \sin\theta|$ in Equation 4.9), which gives a

transverse diffusion of

$$d_{nn}^{ns} = \gamma \frac{h}{2} |\cos\theta - \sin\theta| \sin\theta \cos\theta, \qquad 0 \le \theta \le \pi/2. \tag{4.25}$$

We add a correction d_{nn}^{cor} so that

$$d_{nn}^{ns} + d_{nn}^{cor} = \gamma \frac{h}{2} \max_{0 \le \theta \le \pi/2} (|\cos\theta - \sin\theta| \sin\theta \cos\theta) \equiv h\gamma\psi, \tag{4.26}$$

which occurs at θ^* equal to

$$\theta^* = \arctan\left(\frac{3-\sqrt{5}}{2}\right) \approx 0.365. \tag{4.27}$$

Thus,

$$d_{nn}^{cor} = \gamma \frac{h}{2} (\psi - |\cos\theta - \sin\theta| \sin\theta \cos\theta) \tag{4.28}$$

with $\psi \approx 0.1925$.

We will begin by defining the correction in the finite difference framework for

$$c_t + \nabla \cdot (\boldsymbol{u} c) = 0,$$

where $\boldsymbol{u} = (\cos\theta, \sin\theta)^T$. Consider the case that $u \ge v \ge 0$ or $0 \le \theta \le \pi/4$ (as in section 4.1). The other seven ranges are handled similarly. For this range, the N-scheme depends on the concentrations $C_{i,j}$, $C_{i-1,j}$, and $C_{i,j-1}$. To control the magnitude of the transverse diffusion, we must add at least one point to the stencil. When $\theta^* \le \theta \le \pi/4$ this can be done within the single parameter family of schemes, Equation 4.6, by setting $\kappa = \psi/uv$, which has the effect of modifying the zero weight on the point $C_{i,j-1}$ of the N-scheme stencil (see Equation 4.5). However, as $v \to 0$ ($\theta \to 0$) this κ does not satisfy the positivity constraint $|u - v| \le \kappa \le u + v$ (Equation 4.6) since $\kappa \to \infty$. For positivity the stencil must be modified to include at least one more grid point for the range of parameters that violate positivity. For this range, $0 \le \theta \le \theta^*$, we chose to modify the stencil to include the point $C_{i-1,j+1}$ and remove point $C_{i,j-1}$, thus keeping 4 points. This results in a consistent, positive scheme with constant transverse diffusion given by

$$\begin{aligned} C_{i,j}^{n+1} = C_{i,j}^n &+ \frac{\Delta t}{h}(-uC_{i,j}^n + (u-v)C_{i-1,j}^n + vC_{i-1,j-1}^n) \\ &+ \frac{\Delta t}{2h}\left(\frac{\gamma^3\psi - uv|u-v|}{u^2}\right)(C_{i-1,j+1}^n - 2C_{i-1,j}^n + C_{i-1,j-1}^n), \end{aligned}$$

where $\gamma = \sqrt{u^2 + v^2}$. The modifications to the N-scheme stencil are shown in Figure 4.6 for the entire parameter range $0 \le \theta \le \pi/2$. In this figure, the black square represents the grid point that is updated, the black points are in the original N-scheme stencil, and the black empty circle is the extra point added to the stencil to control the transverse diffusion. We call this scheme the Flat

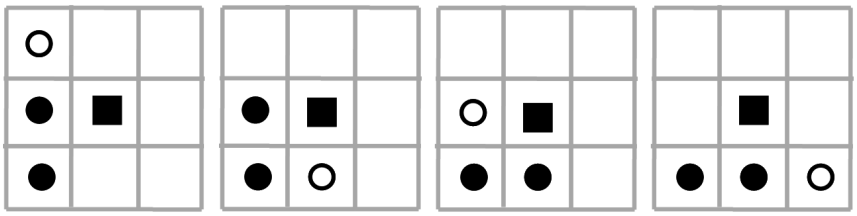

(a) $0 \leq \theta \leq \theta^*$ (b) $\theta^* \leq \theta \leq \pi/4$ (c) $\pi/4 \leq \theta \leq \pi/2 - \theta^*$ (d) $\pi/2 - \theta^* \leq \theta \leq \pi/2$

Figure 4.6: Stencils to be used for $0 \leq \theta \leq \pi/2$ for a constant positive velocity field. In each subfigure, the black square is the point to be updated, the black points are the original N-scheme stencil, and black empty circle is the extra point added to control transverse diffusion.

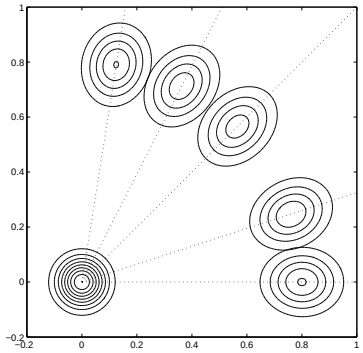

Figure 4.7: A Gaussian blob advected at different angles to the grid for the Flat scheme. Results for all angles are shown in one plot. $\Delta t = 0.75\sqrt{2}/2$ and $t_{\max} = 0.8$. Contours are shown at $c = 0.0, 0.1, \ldots, 1.0$.

scheme because the plot of the transverse diffusion coefficient with respect to θ is a flat line.

The constant velocity test for the Flat scheme is shown in Figure 4.7 using the time step, $\Delta t = 0.75\sqrt{2}h/2$. As can be seen, the scheme has closer to constant transverse spreading of the blob than SPU, the N-scheme, and Koren's scheme as shown in Figure 4.3. The longitudinal spreading and the rotation effects are comparable with the N-scheme, though these terms have been changed slightly by the modification of the stencil.

In the extension of this scheme to an interaction region framework, care be must taken to maintain positivity of the scheme and to not introduce diffusion across faces of cells with low permeability. The resultant scheme is, however, a straightforward extension within the previously defined framework. We will continue to use $\boldsymbol{\sigma}$ to represent the velocity field and change $\zeta(C)$ to C since this scheme is developed for scalar advection. The Flat Scheme can be extended to the more general hyperbolic equation given in Equation 4.10, but as the N-scheme (TMU) is not the best performing scheme for

Range of $\tilde{\theta}$	Pair of (a_p, b_p) values
$0 \le \tilde{\theta} \le \theta^*$	$\left(\frac{\tilde{\gamma}^3\psi - \tilde{\sigma_1}\tilde{\sigma_2}\lvert\tilde{\sigma_2}-\tilde{\sigma_1}\rvert}{\tilde{\sigma_1}(\tilde{\sigma_1}-\tilde{\sigma_2})}, 0\right)$
$\theta^* \le \tilde{\theta} \le \frac{\pi}{2} - \theta^*$	$\left(0, \frac{\tilde{\gamma}^3\psi - \tilde{\sigma_1}\tilde{\sigma_2}\lvert\tilde{\sigma_1}-\tilde{\sigma_2}\rvert}{2\tilde{\sigma_1}\tilde{\sigma_2}}\right)$
$\frac{\pi}{2} - \theta^* \le \tilde{\theta} \le \frac{\pi}{2}$	$\Big(0, 0\Big)$

Table 4.2: (a_p, b_p) pairs for half-face p. If $\sigma_{p-1} < 0$ or $\sigma_{p+1} \ge 0$ then $(a_p, b_p) = (0, 0)$. Parameters for the coefficients calculation are defined as $\tilde{\theta} = \arctan(\sigma_{uw}/\sigma_p)$, $\tilde{\sigma_1} = 2/(1/\sigma_{p-1} - 1/\sigma_{p+1})$, $\tilde{\sigma_2} = \tilde{\sigma_1}\tan\tilde{\theta}$, and $\tilde{\gamma} = \sqrt{\tilde{\sigma_1}^2 + \tilde{\sigma_2}^2}$.

the nonlinear problems we have not implemented this. Consider half-face p in an interaction region. The numerical flux expression for this half-face is

$$\mathcal{F}_p^{adv} = \sigma_p \bar{C}_p = \sigma_p \sum_{q=1}^{4} A_{p,q} C_q, \tag{4.29}$$

with $A_{p,q}$ defined by the N-scheme. If $\sigma_{p-1} \ge 0$ and $\sigma_{p+1} \le 0$, we add to this half-face a first order diffusive flux of the form

$$\mathcal{F}_p^{diff} = \begin{cases} a_p(\bar{C}_{p-1} - \bar{C}_{p+1}) + b_p(C_p \quad - \bar{C}_{p-1}) & \sigma_p \ge 0,\ \sigma_{p-1} \ge 0 \text{ and } \sigma_{p+1} < 0 \\ a_p(\bar{C}_{p-1} - \bar{C}_{p+1}) - b_p(C_{p+1} - \bar{C}_{p+1}) & \sigma_p < 0,\ \sigma_{p-1} \ge 0 \text{ and } \sigma_{p+1} < 0 \\ 0 & \sigma_{p-1} < 0 \text{ or } \sigma_{p+1} \ge 0 \end{cases}. \tag{4.30}$$

The values of $a_p \ge 0$ and $b_p \ge 0$ will depend on σ_{p-1}, σ_p, and σ_{p+1}. Including the half-face concentrations $\bar{C}_{p+1}$ and $\bar{C}_{p-1}$ in the flux expression rather than C_{p-1} and C_{p+2} leads to simpler expressions for (a_p, b_p) that maintain positivity.

In Table 4.2 we give the values for (a_p, b_p) pairs for half-face p. These values have been chosen so that the scheme is consistent with the finite difference formulation when the velocity field is constant and so that the flux expressions depend on as few cells as possible. Using a harmonic average in the definition of $\tilde{\sigma_1}$ introduces less diffusion in cases where the velocity field is rough and avoids smearing across low permeability cells. Positivity of the scheme for these pairs of (a_p, b_p) is shown in Appendix A. Allowing the scheme to have both parameters non-zero at the same time would introduce one more degree of freedom in the scheme and thus the ability to control the other diffusion terms (longitudinal and the mixed-term) but, this would complicate the positivity proofs.

Chapter 5

Miscible Results

We present two different types of test problems to highlight the benefit of multi-D flux calculations. The first is the quarter five-spot problem, which is used throughout the literature to test for grid orientation because it has two natural symmetries and grid-preferred flow directions. The second is a radial displacement in homogeneous and heterogeneous domains. In a homogeneous domain, this displacement does not have a preferred flow direction and hence directly reveals biasing of the numerical solutions. In heterogeneous domains, we consider ensemble averages to help understand the effects of permeability variations on grid dependency, and the relative importance of these effects compared to grid dependent numerical errors.

As in chapter 3, we use the miscible model in fractional flow formulation, that is,

$$0 = -\nabla \cdot \frac{\boldsymbol{K}}{\mu_{e,g}(S_g)} \nabla p \equiv \nabla \cdot \boldsymbol{u}, \tag{5.1}$$

$$0 = \phi \frac{\partial c_g}{\partial t} + \nabla \cdot (c_g \boldsymbol{u}), \tag{5.2}$$

as was derived in section 2.5. In the next chapter we will consider the nonlinear Darcy form. Since there are no gravitational effects the equations do not change if we assume that $\rho_g = \rho_o = 1$ and thus let $c_g = S_g$. Since $S_o = 1 - S_g = c_o$ we let $c \equiv c_g$ since we can always recover $c_o = 1 - c = 1 - c_g$ when needed.

We solve the coupled system, Equations 5.1 and 5.2, with an IMPEC strategy (implicit pressure, explicit concentration). At each time step, a two-point flux approximation is used to solve for the pressures, Equation 5.1. In the x-direction, we set

$$U_{i+1/2,j} = \frac{hK_{i+1/2,j}}{\mu(C^*_{i+1/2,j})} \frac{(P_{i+1,j} - P_{i,j})}{h}, \tag{5.3}$$

where $K_{i+1/2,j} = 2/(1/K_{i+1,j} + 1/K_{i,j})$ is the harmonic average of the permeability on either side

of the face. The fluid mobility is upwinded in a manner consistent with the transport discretization using the previous flux field and current concentrations, which gives $C^*_{i+1/2,j} = \frac{1}{2}\left(\bar{C}_3^{(2),n} + \bar{C}_1^{(3),n}\right)$. We assume that the fluxes do not change too rapidly between time steps. If this were indeed the case, the IMPEC procedure could instead be iterated until $C^*_{i+1/2,j}$ was consistent with fluxes at the new time level. The fluxes in the y-direction $U_{i,j+1/2}$ are defined in an analogous manner. With these definitions, the linear system of equations

$$U_{i+1/2,j} - U_{i-1/2,j} + U_{i,j+1/2} - U_{i,j-1/2} = \frac{q_{i,j}}{h^2},$$

is solved first for pressure, and then the fluxes are calculated locally from Equation 5.3. Here, $q_{i,j} < 0$ for a production well, and $q_{i,j} > 0$ for an injection well. After solving for pressure and the flux field, we advance concentrations to the next time level using one of the transport methods described in sections 4.6 and 4.8.

The time step size is constrained to ensure that we do not extract more fluid from a production well block than is available, that is, $\Delta t \leq 1/(h^2 q_{\max})$ where $q_{\max} = \max_{\{i,j\}}(-q_{i,j})$, i.e. the largest production well rate. The time step size is also constrained by the CFL condition for the hyperbolic transport solve.

As previously noted, our monotone methods are positive when applied to scalar advection problems. This means that as long as the well source terms are consistent with the divergence of the pressure field in the well blocks, the mass concentrations will satisfy $C^n_{i,j} \in [0, \rho_g]$ throughout the entire simulation. As we will see in chapter 6 we will need a complex framework for simulation of nonlinear equations.

5.1 Homogeneous Quarter Five-Spot

Here we consider the quarter five-spot problem as discussed in section 3.1. In Figure 5.1 the results for a 50×50 diagonal grid are compared with those for a 71×71 parallel grid with a mobility ratio of $M = 30$. The recovery curves are shown for 1 PVI (pore volume injected) for SPU and the Flat scheme. The displacement fronts are compared at 0.4 PVI for all four schemes. The displacement fronts show that both SPU and Koren's scheme have strongly different solutions on the two grids. On the diagonal grid, the fingers in the SPU solution correspond to the grid directions (0 and $\pi/2$), which are also the zero points of the transverse diffusion. The zero points for Koren's scheme are also at 0 and $\pi/2$, and as expected we see fingers in these directions. We also notice a finger at $\pi/4$ which is expected based on the boundary and well conditions. The level of transverse diffusion at $\pi/4$ is about half that of SPU, as shown in Figure 4.2(b). The N-scheme and the Flat scheme have more similar solutions on the two grids, with both exhibiting a three-finger structure. These three fingers correspond to the three zero points of the N-scheme at 0, $\pi/4$, and $\pi/2$. The fingers in the displacement fronts for the Flat scheme are slightly smaller than for the N-scheme, though finger

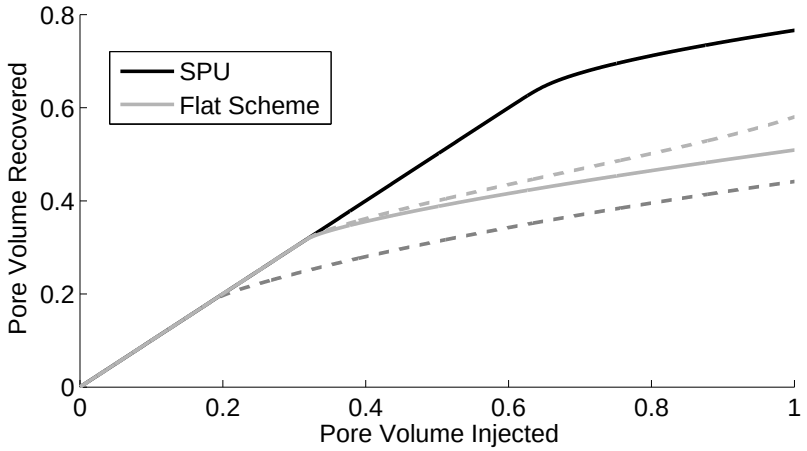

(a) Recovery curves for SPU and the Flat scheme on the diagonal (solid) and parallel (dashed) grids.

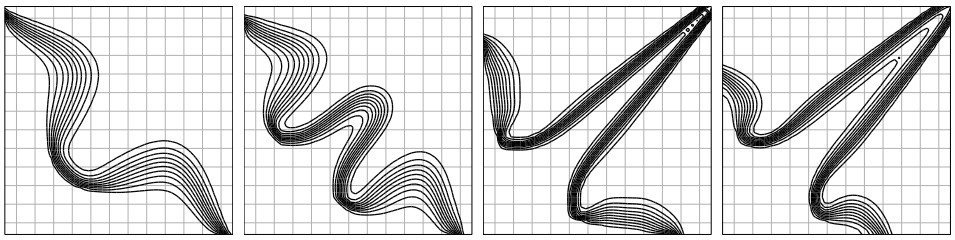

(b) SPU (c) Koren's Scheme (d) N-Scheme (e) Flat Scheme

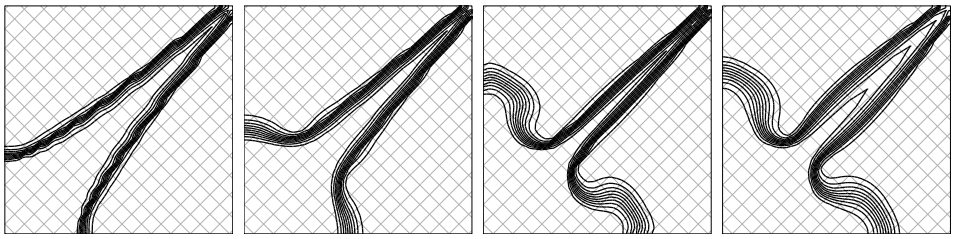

(f) SPU (g) Koren's Scheme (h) N-Scheme (i) Flat Scheme

Figure 5.1: A miscible adverse mobility ratio, $M = 30$, quarter five-spot displacement simulated on a 50×50 diagonal grid and 71×71 parallel grid. SPU, Koren's scheme, the N-scheme, and the Flat scheme are compared for displacement fronts shown at 0.4 PVI. Solutions (b)-(e) were computed on the diagonal grid and the contours in (f)-(i) used the parallel grid.

growth still occurs along the same directions. This is likely due to the fact that the Flat scheme is a modification of the N-scheme, and the diffusion added is purposely kept low so as not to diffuse into no-flow grid blocks. The breakthrough times are much closer for the N-scheme and the Flat scheme than for SPU and Koren's scheme.

Our results clearly show that these problems are highly sensitive to numerical errors. Therefore, numerical solutions may change significantly as a result of grid refinement or changes in grid orientation. The sensitivity is lower for large physical diffusion, but in realistic reservoir models of these adverse mobility flows, the physical diffusion will be overwhelmed by numerical diffusion. Consequently, it is not possible to derive "correct" solutions. However, in order to reliably calibrate the model at the simulation scale, it is crucial that the solution at that scale does not exhibit strong sensitivity to grid orientation. The truly multi-D schemes do much better than SPU, and overall the Flat scheme and N-scheme show the least grid dependency.

In Figure 5.2 displacement fronts for SPU and the Flat scheme are compared for increasing mobility ratios $M = 1,\ 5,\ 10,\ 30$ using the same grids as above. For $M = 1$ the problem is stable, hence the solutions are very close on the two grids. But as the mobility ratio increases and unstable physical modes become present in the problem, the SPU solutions on the two grids diverge whereas the Flat scheme solutions remain similar.

5.2 Radial Flow

As a second test we consider a radial displacement on a 99×99 grid with an injector in the center grid block $(0, 0)$, $q_{0,0} = 1$, and Dirichlet pressure boundary conditions on $(i, \pm 49)$ and $(\pm 49, j)$. At these boundaries the pressure is forced to the solution for homogeneous radial flow, given by $p(x, y) = -\frac{1}{2\pi} \ln \sqrt{x^2 + y^2}$. The integral of the pressure over the grid block (i, j) is approximated with the trapezoidal rule. For this test problem the homogeneous results for SPU, the N-scheme, and the Flat scheme are shown in Figure 5.3. They clearly show strong preferential transport along the grid directions for SPU. The N-scheme and Flat scheme results also show preferential transport along the grid directions with additional preferred transport at $\pi/4$, $3\pi/4$, $5\pi/4$, and $7\pi/4$. However, the deviation from radial flow is much smaller than for SPU, with the Flat scheme giving the best results.

To understand how the numerical errors affect the solutions in the presence of heterogeneity, we simulate this same displacement on random permeability fields and compute an ensemble average of the results. We use sequential Gaussian simulation (Deutsch and Journel, 1998) to generate log-normally distributed permeability fields of dimensions 99×99 on a unit square. The dimensionless correlation lengths are set at $\lambda = 3/99$ and $\lambda = 10/99$, corresponding to correlation lengths of 3 and 10 grid blocks, respectively. The standard deviation σ of $\ln K$ is set to either $\sigma = 0.25$ or $\sigma = 1.00$, and the mean of $\ln K$ is fixed at 3.0.

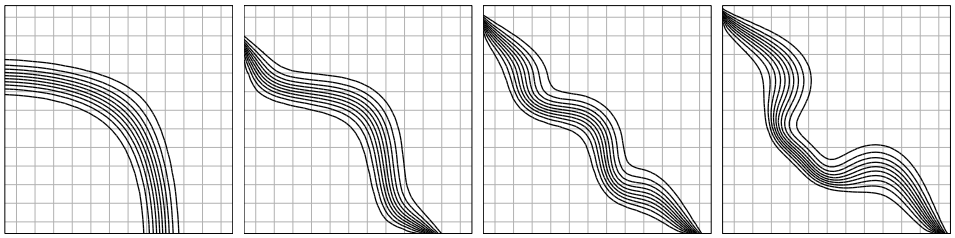

(a) SPU, $M = 1$, diagonal grid (b) SPU, $M = 5$, diagonal grid (c) SPU, $M = 10$, diagonal grid (d) SPU, $M = 20$, diagonal grid

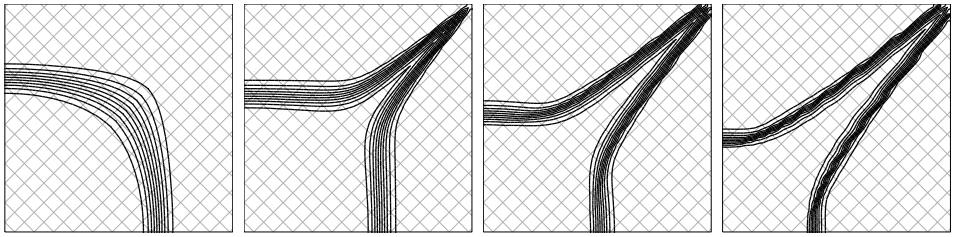

(e) SPU, $M = 1$, parallel grid (f) SPU, $M = 5$, parallel grid (g) SPU, $M = 10$, parallel grid (h) SPU, $M = 20$, parallel grid

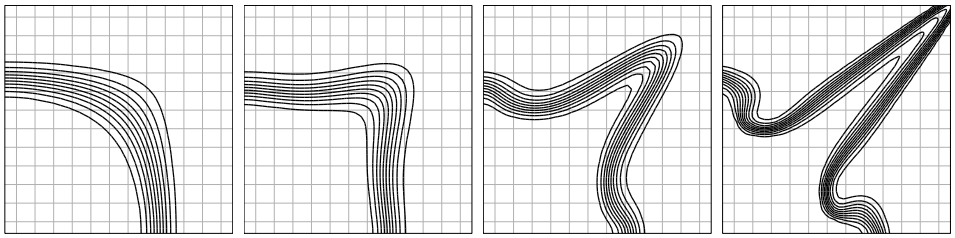

(i) Flat Scheme, $M = 1$, diagonal grid (j) Flat Scheme, $M = 5$, diagonal grid (k) Flat Scheme, $M = 10$, diagonal grid (l) Flat Scheme, $M = 20$, diagonal grid

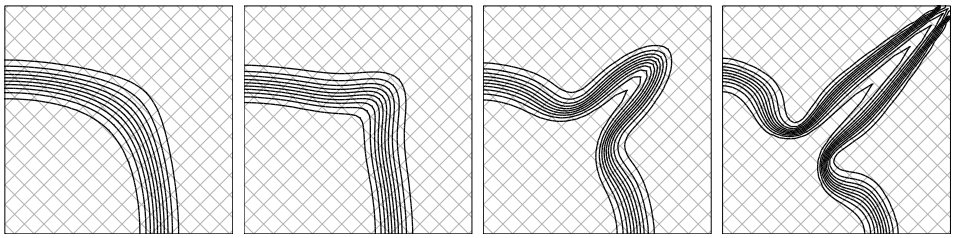

(m) Flat Scheme, $M = 1$, parallel grid (n) Flat Scheme, $M = 5$, parallel grid (o) Flat Scheme, $M = 10$, parallel grid (p) Flat Scheme, $M = 20$, parallel grid

Figure 5.2: Comparisons between SPU and the Flat scheme for a quarter five-spot displacement with increasing mobility ratios simulated on a 50×50 diagonal grid and 71×71 parallel grid.

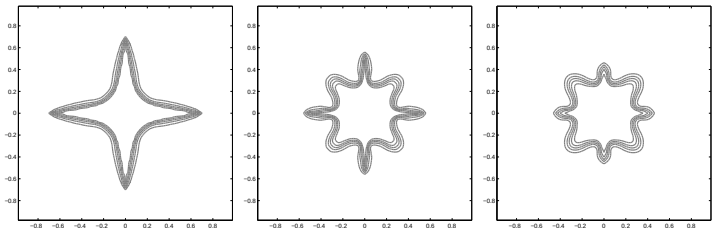

(a) SPU (b) N-scheme (c) Flat scheme

Figure 5.3: Radial test problem in a homogeneous media for $M = 30$ using a 99×99 computational grid. Results are shown for SPU, the N-scheme, and the Flat scheme.

Figure 5.4 shows results for the three schemes on one realization of the permeability field for each pair of λ and σ values. The plots show strong differences between the SPU solutions, the N-scheme, and Flat scheme solutions. The differences are particularly stark for $\sigma = 0.25$. Figure 5.5 presents the ensemble averaged results for the full set of realizations. The number of realizations is chosen so that the average displacement solution appears symmetric. Therefore, fewer simulations are required for the fields with weaker permeability variations. Clearly, the schemes introduce biases: on average, numerical errors trigger fingers in preferential directions. SPU suffers most from the grid orientation effect. Even for the large permeability contrasts, its solutions are clearly grid dependent. This bias does not show clearly for a single realization, which demonstrates the utility of ensemble averaging. The N-scheme and the Flat scheme both show strongly reduced biasing. The solutions have more preferential flow paths. This was expected as for these schemes, the numerical transverse diffusion averaged over all angles is less than half that of SPU. This is sufficiently low enough that fingers are triggered more easily by the permeability variations rather than grid dependent numerical errors.

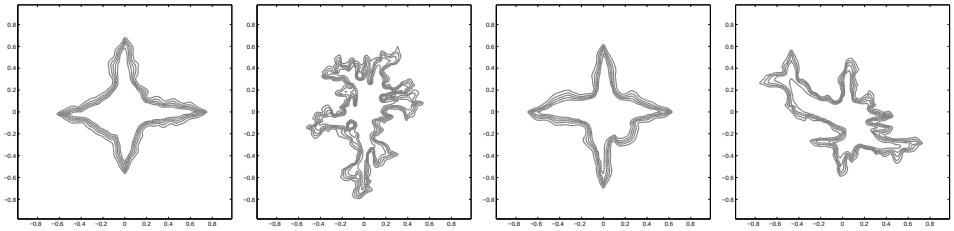

(a) SPU: 3 grid block correlation, $\sigma = 0.25$, $k_{\max}/k_{\min} = 6.5$

(b) SPU: 3 grid block correlation, $\sigma = 1.00$, $k_{\max}/k_{\min} = 1899$

(c) SPU: 10 grid block correlation, $\sigma = 0.25$, $k_{\max}/k_{\min} = 5.9$

(d) SPU: 10 grid block correlation, $\sigma = 1.00$, $k_{\max}/k_{\min} = 1232$

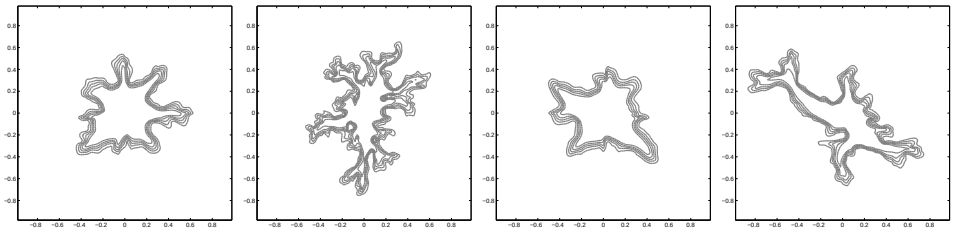

(e) N-Scheme: 3 grid block correlation, $\sigma = 0.25$

(f) N-Scheme: 3 grid block correlation, $\sigma = 1.00$

(g) N-Scheme: 10 grid block correlation, $\sigma = 0.25$

(h) N-Scheme: 10 grid block correlation, $\sigma = 1.00$

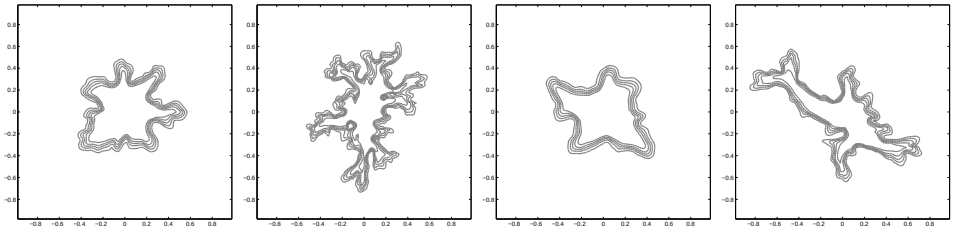

(i) Flat Scheme: 3 grid block correlation, $\sigma = 0.25$

(j) Flat Scheme: 3 grid block correlation, $\sigma = 1.00$

(k) Flat Scheme: 10 grid block correlation, $\sigma = 0.25$

(l) Flat Scheme: 10 grid block correlation, $\sigma = 1.00$

Figure 5.4: Radial test problem for a single realization of the permeability field with the parameters shown.

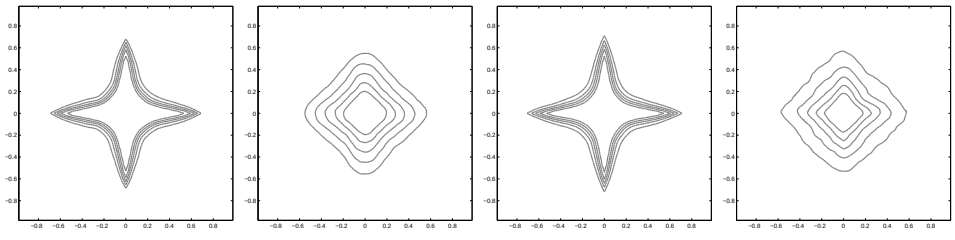

(a) SPU: 3 grid block correlation, $\sigma = 0.25$

(b) SPU: 3 grid block correlation, $\sigma = 1.00$

(c) SPU: 10 grid block correlation, $\sigma = 0.25$

(d) SPU: 10 grid block correlation, $\sigma = 1.00$

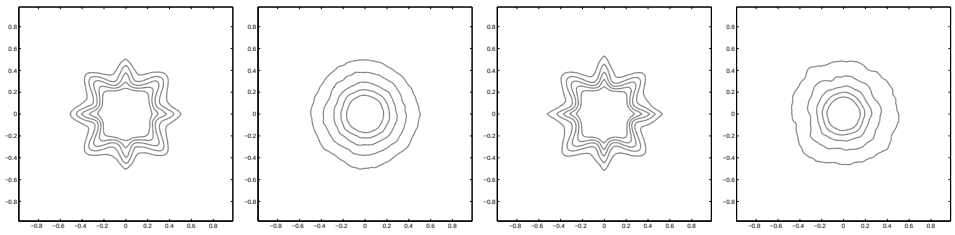

(e) N-Scheme: 3 grid block correlation, $\sigma = 0.25$

(f) N-Scheme: 3 grid block correlation, $\sigma = 1.00$

(g) N-Scheme: 10 grid block correlation, $\sigma = 0.25$

(h) N-Scheme: 10 grid block correlation, $\sigma = 1.00$

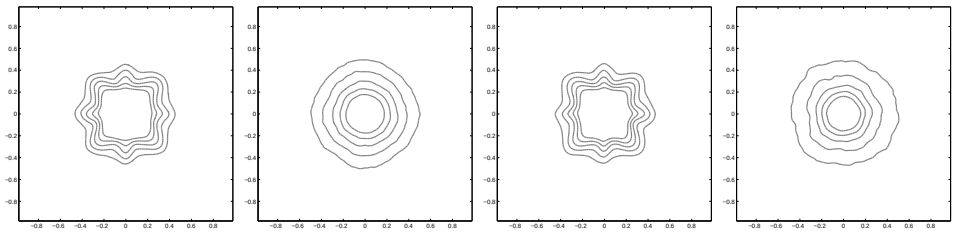

(i) Flat Scheme: 3 grid block correlation, $\sigma = 0.25$

(j) Flat Scheme: 3 grid block correlation, $\sigma = 1.00$

(k) Flat Scheme: 10 grid block correlation, $\sigma = 0.25$

(l) Flat Scheme: 10 grid block correlation, $\sigma = 1.00$

Figure 5.5: Ensemble averages of displacement fronts for multiple realizations of a heterogeneous permeability field for the radial test problem. The standard deviation of $\ln K$, σ, controls the permeability contrast of the individual permeability realizations: $k_{\max}/k_{\min} \sim 6$ for $\sigma = 0.25$ and $k_{\max}/k_{\min} \sim 10^3$ for $\sigma = 1.00$. 175 realizations were used for the correlation length of three grid blocks, and 330 were used for the 10 grid block correlation solutions.

Chapter 6

Nonlinear Framework and Simulation Results

For the case of scalar advection, the monotone schemes that we used were positive as was shown in chapter 4. This meant that when these schemes were applied to the miscible model in fractional flow form, the mass concentrations were provably bounded in $C^n_{i,j} \in [0,1]$. For nonlinear problems this is not the case. As we will see, monotonicity, along with certain physical assumptions on the mobility function, constrains the lower bound but not the upper bound of the updated mass concentrations. When discretized in a manner consistent with the transport equation, the pressure equation acts as a constraint equation bounding the upper value of the mass variables. For general mobility stencils, such as those arising from multi-D mobility weighting, it is impractical to fully reduce the pressure residual as this requires nonlinear iterations on the pressure equation. Thus before applying the multi-D methods to the nonlinear problem, we develop a volume relaxed framework for simulation. This framework will allow us to handle numerical errors in a consistent and robust manner and will ensure that the saturations remain physical.

6.1 Discrete Governing Equation Framework

Our first consideration is to present the finite volume framework with which we discretize Equations 2.6 and 2.7. Written in finite volume form, these equations become

$$0 = \sum_{\alpha=o,w} \left(\sum_{j \in neigh\{i\}} \frac{\mathcal{F}^n_{\alpha,i,j}}{\rho_\alpha} - \frac{Q^n_{\alpha,i}}{\rho_\alpha} \right),$$

$$C^{n+1}_{\alpha,i} = C^n_{\alpha,i} - \frac{\Delta t}{V_i} \sum_{j \in neigh\{i\}} \mathcal{F}^n_{\alpha,i,j} + \frac{\Delta t}{V_i} Q^n_{\alpha,i}, \qquad \alpha = o,w,$$

with the integral terms

$$\mathcal{F}_{\alpha,i,j} = -\rho_\alpha \int_{t^n}^{t^{n+1}} \iint_{\partial\Omega_{i,j}} \lambda(S_\alpha)\boldsymbol{K}\nabla(p_\alpha - \rho_\alpha g h)\cdot\widehat{n}_{i,j}\; ds\; dt, \tag{6.1}$$

$$Q^n_{\alpha,i} = \rho_\alpha \int_{t^n}^{t^{n+1}} \iiint_{\Omega_i} q_\alpha\; dV\; dt.$$

Assume that we have a discretization of Equation 6.1 of the form

$$\begin{aligned}
\mathcal{F}_{\alpha,i,j} &= \int_{t^n}^{t^{n+1}} \int_{\partial\Omega_{i,j}} \rho_\alpha \boldsymbol{u}_\alpha \cdot \widehat{n}_{i,j}\; ds\; dt \\
&= -\int_{t^n}^{t^{n+1}} \int_{\partial\Omega_{i,j}} \rho_\alpha \lambda_\alpha(S_\alpha)(\boldsymbol{K}\nabla(p - \rho_\alpha g h))\cdot\widehat{n}_{i,j}\; ds\; dt \\
&\approx \rho_\alpha \bar{\lambda}_{\alpha,i,j}\sigma_{\alpha,i,j},
\end{aligned}$$

where $\bar{\lambda}_{\alpha,i,j}$ is a face-based mobility value and $\sigma_{\alpha,i,j}$ is the discretization of the phase flux, not to be confused with the mass flux $\mathcal{F}_{\alpha,i,j}$ of phase α, that is,

$$\sigma_{\alpha,i,j} \approx -\int_{t^n}^{t^{n+1}} \int_{\partial\Omega_{i,j}} (\boldsymbol{K}\nabla(p - \rho_\alpha g h))\cdot\widehat{n}_{i,j}\; ds\; dt.$$

In this way we split the fluid properties, which are captured in $\bar{\lambda}_\alpha$, from the geometric properties, which are captured in σ_α. We call this latter term the geometric term because it is independent of the particular fluids present, depends purely on the rock properties (absolute permeability), and closely resembles the flux expression used in single-phase flow (Aziz and Settari, 1979). This splitting allows us to apply elliptic discretization principles to the phase flux terms σ_α and hyperbolic techniques to the phase mobility terms λ_α.

6.1.1 Discretization of the Geometric Properties

The phase flux terms are typically discretized as

$$\boldsymbol{\sigma}_\alpha = \boldsymbol{T}(\boldsymbol{p}^{n+1} - \rho_\alpha g \boldsymbol{H}),$$

where $\boldsymbol{p}$ is a vector of all the cell-centered pressures p_i, $\boldsymbol{\sigma}_\alpha$ is a vector of all $\sigma_{\alpha,i,j}$ values, $\boldsymbol{T}$ is a sparse transmissibility matrix with a zero row sum, and $\boldsymbol{H}$ is a vector of cell heights h_i. The

determination of the transmissibility matrix has been the subject of much research, especially for heterogeneous, full tensor permeability and nonorthogonal grids. It is generally assumed that $\boldsymbol{T}$ is independent of time and phase so that it can be determined prior to the simulation. For a two point flux approximation there are two non-zeros in each row of $\boldsymbol{T}$. For example, assume we have a two dimensional Cartesian grid with grid spacing Δx and Δy with thickness Δz and a pointwise isotropic permeability tensor $\boldsymbol{K}_{i,j} = K_{i,j}\boldsymbol{I}$. If $\boldsymbol{t}_l$ is row l of $\boldsymbol{T}$ corresponding to the face $i+1/2, j$, that is, the face between cells (i,j) and $(i+1,j)$, then

$$\sigma_{\alpha,i,j} = \boldsymbol{t}_l(\boldsymbol{p}^{n+1} - \rho_\alpha g \boldsymbol{H}) = -\frac{\Delta x \Delta y \Delta z}{\Delta x} \frac{2}{\frac{1}{K_{i,j}} + \frac{1}{K_{i+1,j}}}((p^{n+1}_{i+1,j} - \rho_\alpha g H_{i+1,j}) - (p^{n+1}_{i,j} - \rho_\alpha g H_{i,j})),$$

where $p_{i,j}$ and $H_{i,j}$ are the average pressure and height of cell (i,j), respectively, and we use harmonic averaging to determine the effective permeability of the face based on the cell permeabilities. Consistent extension of the two-point flux approximation can be constructed when the grid is K-orthogonal. If we consider a general grid with two neighboring cells i and j separated by face l then the grid is K-orthogonal when there exists a point on the face, or its extension, say $\bar{\boldsymbol{x}}_l$, such that $\boldsymbol{K}_i(\bar{\boldsymbol{x}}_l - \boldsymbol{x}_i)$ and $\boldsymbol{K}_j(\bar{\boldsymbol{x}}_l - \boldsymbol{x}_j)$ are orthogonal to the face where $\boldsymbol{x}_i$ and $\boldsymbol{x}_j$ are the cell centers and $\boldsymbol{K}_i$ and $\boldsymbol{K}_j$ are the permeability tensors for each cell. When the grid is not K-orthogonal, multi-point flux approximations are desirable which involve more than two neighboring cells in the determination of the phase flux (Aavatsmark, 2002; Edwards and Rogers, 1998). In the examples shown in section 6.2 we will use Cartesian grids and assume pointwise isotropic permeability tensors so that $\boldsymbol{K}_j = K_j\boldsymbol{I}$, where K_j is a scalar, so that the two-point flux approximation is valid. This is the same pressure discretization as was used in chapters 3 and 5.

6.1.2 Discretization of the Fluid Properties

In section 4.5 we developed monotone discretization methods for the equation

$$c_t + \nabla \cdot (\boldsymbol{\sigma}\zeta(C)) = 0.$$

Here we need to apply these methods to the system of equations

$$c_{\alpha,t} + \nabla \cdot (\rho_\alpha \boldsymbol{\sigma}_\alpha \lambda_\alpha(S_\alpha)) = 0, \tag{6.2}$$

where $\alpha = o, w$. We do this by applying the methods to each mass phase independently, that is, for each grid face a mobility value, $\bar{\lambda}_\alpha$, is calculated for each phase α. This will lead to methods that are monotone with respect to the phase being updated. So then for each phase

$$\bar{\boldsymbol{\lambda}}_\alpha = \boldsymbol{R}_\alpha \lambda(\boldsymbol{S}_\alpha),$$

where $\boldsymbol{R}_\alpha$ is the stencil matrix for phase α. In the absence of gravitational forces or capillary forces R_α is the same for both phases, since σ_α is the same for both phases. In general there will be a different stencil matrix for each phase.

In order to compute $\lambda_\alpha(\boldsymbol{S}_{\alpha,i})$, we will need to calculate the saturations from the mass concentrations. In the continuous case we took

$$S_{\alpha,i} = C_{\alpha,i}/\rho_\alpha, \tag{6.3}$$

but as noted above we have no upper bound for the discrete values of C_α, hence the saturations would not be bounded below unity. Due to this challenge, we use the discrete saturation definition

$$S_{\alpha,i}(C_{w,i}, C_{o,i}) = \frac{C_{\alpha,i}/\rho_\alpha}{C_{w,i}/\rho_w + C_{o,i}/\rho_o} = \frac{\text{volume of phase } \alpha \text{ in cell i}}{\text{total volume of fluid in cell i}}. \tag{6.4}$$

Assuming that $C_{w,i} \geq 0$ and $C_{o,i} \geq 0$, the definition of discrete saturations given in Equation 6.4 guarantees physical saturations, that is, $S_{w,i} + S_{o.i} = 1$ and $S_{\alpha,i} \geq 0$.

The discrete nonlinear update for phase α can be written as

$$C_{\alpha,i}^{n+1} = G_{\alpha,i}(\boldsymbol{C}_o^n, \boldsymbol{C}_w^n),$$

where $\boldsymbol{C}_\alpha^n$ is a vector of average mass values of phase α for the entire grid. The update depends on both mass variables due to the fact that saturation is a function of both masses. We say that the discretization in phase α is monotone if

$$\frac{\partial C_{\alpha,i}^{n+1}}{\partial C_{\alpha,j}^n} = \frac{\partial G_{\alpha,i}(\boldsymbol{C}_o, \boldsymbol{C}_w)}{\partial C_{\alpha,j}} \geq 0, \qquad \forall\ i, j,$$

where $0 \leq \boldsymbol{C}_\alpha \leq \boldsymbol{C}_\alpha^n$ ($\leq$ is computed pointwise). This above expression says that the update for phase α is a monotone function of the grid values. Note that the derivative in the above equation is only with respect to the phase that is being updated, not both phases. Note that this definition of monotonicity is slightly different than that used in the work of Crandall and Majda (1980) in that the upper bound is the current grid value and not a fix constant. We do this because we will not be explicitly imposing an upper bound on the mass concentrations. It is easily verified that if $C_{\alpha,j}^n \geq 0$ for all j, then monotonicity implies that $C_{\alpha,i}^{n+1} \geq 0$ for all i if the discretization is consistent (see appendix C). Hence, using a monotone discretization along with the discrete saturation definition yields physical saturations and masses.

We must verify that the discretization methods we developed in section 4.5 are still monotone under this modified definition of monotonicity. In this setting, the mobility function is now a function of both masses, since saturation is a function of both masses. Hence, when discretizing Equation

6.2 we have a $\zeta(C)$ which is a function of both masses,

$$\zeta_\alpha(C_o, C_w) = \rho_\alpha \lambda_\alpha \left(S_\alpha \left(C_o, C_w\right)\right). \tag{6.5}$$

If we take the derivative of this function with respect to C_α we have

$$\frac{\partial \zeta_\alpha(C_o, C_w)}{\partial C_\alpha} = \rho_\alpha \lambda'_\alpha \left(S_\alpha \left(C_o, C_w\right)\right) \frac{\partial S_\alpha \left(C_o, C_w\right)}{\partial C_\alpha} = \rho_\alpha \lambda'_\alpha \left(S_\alpha \left(C_o, C_w\right)\right) \frac{C_{\beta \neq \alpha}}{\left(C_w + C_o\right)^2}. \tag{6.6}$$

The last term in this equation

$$\frac{C_{\beta \neq \alpha}}{\left(C_w + C_o\right)^2} \geq 0,$$

if $C_o \geq 0$ and $C_w \geq 0$, so the sign of the Equation 6.6 is solely determined by the sign of $\lambda'_\alpha(S_\alpha)$.

If we write the mass update for the entire grid as

$$\boldsymbol{C}_\alpha^{n+1} = \boldsymbol{C}_\alpha^n - \Delta t \boldsymbol{V}^{-1} \left(\mathbf{Div}\left(\left(\rho_\alpha \bar{\boldsymbol{\lambda}}_\alpha(\boldsymbol{S}_\alpha^n, \boldsymbol{p}^{n+1})\right) \bullet \boldsymbol{\sigma}_\alpha(\boldsymbol{p}^{n+1})\right) - \boldsymbol{Q}_\alpha(\boldsymbol{S}_\alpha^n, \boldsymbol{p}^{n+1})\right), \tag{6.7}$$

then this suggests the following algorithm for calculating the face mobilities

Determine the discrete saturations $\boldsymbol{S}_w^n$ and $\boldsymbol{S}_o^n$ from $\boldsymbol{C}_w^n$ and $\boldsymbol{C}_o^n$ (Equation 6.4)
Using the discrete saturations, calculate the face mobilities $\bar{\boldsymbol{\lambda}}_\alpha$ using a scheme from section 4.6
Update the mass of phase α using Equation 6.7

This leads to a monotone methods as shown in section 4.5.

6.1.3 Development of the Mass Conservative Framework

As in the continuous case, the discrete pressure equation can be defined by summing the mass update equations for both phases scaled by the density,

$$\begin{aligned} &\sum_{\alpha=o,w} \frac{\boldsymbol{C}_\alpha^{n+1}}{\rho_\alpha} = \\ &\sum_{\alpha=o,w} \frac{\boldsymbol{C}_\alpha^n}{\rho_\alpha} - \Delta t \boldsymbol{V}^{-1} \sum_{\alpha=o,w} \left(\mathbf{Div}\left(\bar{\boldsymbol{\lambda}}_\alpha(\boldsymbol{S}_\alpha^n, \boldsymbol{p}^{n+1}) \bullet \boldsymbol{\sigma}_\alpha(\boldsymbol{p}^{n+1})\right) - \boldsymbol{Q}_\alpha(\boldsymbol{S}^n, \boldsymbol{p}^{n+1})\right). \end{aligned} \tag{6.8}$$

In section 2.3 we assumed

$$\sum_{\alpha=o,w} \frac{C_{\alpha,i}^{n+1}}{\rho_\alpha} = \sum_{\alpha=o,w} \frac{C_{\alpha,i}^n}{\rho_\alpha} = 1,$$

that is, we assumed that the total volume of fluid in each cell was constant. As noted above, we relax this in the nonlinear discrete case allowing for a volume residual in the pressure equation of

the form

$$\sum_{\alpha=o,w}\left(\frac{\boldsymbol{C}_\alpha^{n+1}}{\rho_\alpha}-\frac{\boldsymbol{C}_\alpha^{n}}{\rho_\alpha}\right).$$

When we solve Equation 6.8 we set

$$\sum_{\alpha=o,w}\frac{C_{\alpha,i}^{n+1}}{\rho_\alpha}=1,$$

in an attempt to achieve mass balance at time n+1. Given Equation 6.8 we can define the following implicit pressure explicit mass methods (IMPEM) with the discrete nonlinear system of equations

$$\boldsymbol{e}=\sum_{\alpha=o,w}\frac{\boldsymbol{C}_\alpha^{n}}{\rho_\alpha}-\Delta t\boldsymbol{V}^{-1}\sum_{\alpha=o,w}\left(\mathbf{Div}\left(\bar{\boldsymbol{\lambda}}_\alpha(\boldsymbol{S}_\alpha^n,\boldsymbol{p}^{n+1})\bullet\boldsymbol{\sigma}_\alpha(\boldsymbol{p}^{n+1})\right)-\boldsymbol{Q}_\alpha(\boldsymbol{S}_\alpha^n,\boldsymbol{p}^{n+1})\right), \tag{6.9}$$

$$\boldsymbol{C}_w^{n+1}=\boldsymbol{C}_w^{n}-\Delta t\boldsymbol{V}^{-1}\left(\mathbf{Div}\left(\rho_w\bar{\boldsymbol{\lambda}}_w(\boldsymbol{S}_w^n,\boldsymbol{p}^{n+1})\bullet\boldsymbol{\sigma}_w(\boldsymbol{p}^{n+1})\right)-\boldsymbol{Q}_w(\boldsymbol{S}_o^n,\boldsymbol{p}^{n+1})\right), \tag{6.10}$$

$$\boldsymbol{C}_o^{n+1}=\boldsymbol{C}_o^{n}-\Delta t\boldsymbol{V}^{-1}\left(\mathbf{Div}\left(\rho_o\bar{\boldsymbol{\lambda}}_o(\boldsymbol{S}_o^n,\boldsymbol{p}^{n+1})\bullet\boldsymbol{\sigma}_o(\boldsymbol{p}^{n+1})\right)-\boldsymbol{Q}_o(\boldsymbol{S}_w^n,\boldsymbol{p}^{n+1})\right), \tag{6.11}$$

where $\boldsymbol{e}$ is the vector of all ones and the saturations are defined for $\alpha=o,w$ as

$$\boldsymbol{S}_\alpha^n=\frac{\boldsymbol{C}_\alpha^n/\rho_\alpha}{\boldsymbol{C}_w^n/\rho_w+\boldsymbol{C}_o/\rho_o}.$$

Algorithmically the IMPEM method is

Initialize $\boldsymbol{C}_w^0$ and $\boldsymbol{C}_o^0$
for $n=1,2,\cdots$ **do**
  Define saturations $\boldsymbol{S}_w^n$ and $\boldsymbol{S}_o^n$ using $\boldsymbol{C}_w^n$ and $\boldsymbol{C}_o^n$ (Equation 6.4)
  Solve the nonlinear Equation 6.9 for $\boldsymbol{p}^{n+1}$ with fixed $\boldsymbol{S}_w^n$ and $\boldsymbol{S}_o^n$ (see subsection 6.1.4)
  Use $\boldsymbol{p}^{n+1}$ and $\boldsymbol{C}^n$ to update $\boldsymbol{C}_w^{n+1}$ (Equation 6.10)
  Use $\boldsymbol{p}^{n+1}$ and $\boldsymbol{C}^n$ to update $\boldsymbol{C}_o^{n+1}$ (Equation 6.11)
end for

In section 2.3 we had five unknowns determined by three differential equations and three constraint equations, where the constraint equations were used to resolve the overdetermined nature of the system. In the discrete system we have six unknowns determined by three difference equations and three constraint equations. The difference arises because we have relaxed the assumption that fluid volume and pore volume are the same, therefore adding an additional unknown to the system (volume of fluid).

If we use the definition of saturation given in Equation 6.3, then the above algorithm becomes an IMPES (implicit pressure, explicit saturation) method. The overdetermined nature of the system of equations must still be overcome. Updating both saturation variables would result in a relaxing of the constraint equation $S_o+S_w=1$, whereas updating one saturation, say water, and defining

the other as $S_o = 1 - S_w$ may relax the physical assumption $S_o \geq 0$, since monotonicity does not guarantee $S_w \leq 1$ only that $S_w \geq 0$. Also, even if saturation is used, the pressure equation would still be nonlinear in the mobility functions when multi-D weightings are used. Using the discrete definition of saturation given by Equation 6.4, we are guaranteed nonnegative masses and physical saturations. We have the added complication of needing to update both the mass of water and oil which may not be required in an IMPES method. However, this is not a significant burden since the stencil matrix used to update the masses is required for the next pressure solve, and we have the added benefit of a more robust simulation framework.

6.1.4 Solving the IMPEM Pressure Equation

In the proposed IMPEM method, Equation 6.9 is nonlinear in the pressure. The tolerance to which this equation is solved determines the size of the volume residual. Standard Newton's method works quite well for the schemes proposed in section 4.6, since the IMPEM time step is sufficiently small to result in fast convergence. Rewriting Equation 6.9 as a nonlinear equation results in the root finding system

$$\begin{aligned}&\boldsymbol{F}_p(\boldsymbol{p}) = \\ &\boldsymbol{e} - \sum_{\alpha=o,w} \frac{\boldsymbol{C}_\alpha^n}{\rho_\alpha} + \Delta t \boldsymbol{V}^{-1} \sum_{\alpha=o,w} \left(\mathbf{Div}\left(\bar{\boldsymbol{\lambda}}_\alpha(\boldsymbol{S}_\alpha^n, \boldsymbol{p}^{n+1}) \bullet \boldsymbol{\sigma}_\alpha(\boldsymbol{p}^{n+1})\right) - \boldsymbol{Q}_\alpha(\boldsymbol{S}_\alpha^n, \boldsymbol{p}^{n+1})\right),\end{aligned}$$

where we want to find a $\boldsymbol{p}^{n+1}$ such that $\boldsymbol{F}_p(\boldsymbol{p}^{n+1}) = 0$. Newton's method for this equation looks like

$k = 0$
$\boldsymbol{p}^k = \boldsymbol{p}^n$
while $|\boldsymbol{F}_p(\boldsymbol{p}^k)| > TOL$ **do**
  Solve: $\boldsymbol{J}_{pp}^T(\boldsymbol{p}^k)\boldsymbol{\delta}^k = -\boldsymbol{F}_p(\boldsymbol{p}^k)$
  $\boldsymbol{p}^{k+1} = \boldsymbol{p}^k + \boldsymbol{\delta}^k$
  $k := k + 1$
end while

$\boldsymbol{J}_{pp}^T(\boldsymbol{p}^k)$ is the Jacobian of $\boldsymbol{F}_p(\boldsymbol{p}^k)$ which can be expressed as

$$\begin{aligned}&\boldsymbol{J}_{pp}^T(\boldsymbol{p}^k) = \\ &\Delta t \boldsymbol{V}^{-1}\left(\mathbf{Div}\left(\operatorname{diag}(\bar{\boldsymbol{\lambda}}_\alpha(\boldsymbol{S}_\alpha^n, \boldsymbol{p}^k))\boldsymbol{T} + \operatorname{diag}(\boldsymbol{\sigma}_\alpha(\boldsymbol{p}^k))\left(\frac{\partial \bar{\boldsymbol{\lambda}}_\alpha}{\partial \boldsymbol{p}}\right)\Big|_{S_\alpha^n, p^k}^T\right) + \left(\frac{\partial \boldsymbol{Q}_\alpha}{\partial \boldsymbol{p}}\right)\Big|_{S_\alpha^n, p^k}^T\right).\end{aligned}$$

Here the operator diag(·) creates a diagonal matrix from a given vector. For SPU $\frac{\partial \bar{\boldsymbol{\lambda}}_\alpha}{\partial \boldsymbol{p}} = \mathbf{0}$, but for more general discretizations, which incorporate more characteristic flow information, it can be non-zero. Fortunately, for the family of schemes we propose in section 4.5, the derivatives can be computed with only minimal additional work as was shown in section 4.5.1.

Due to the relaxed volume property of the framework it is not necessary to solve this nonlinear system to a small tolerance (we used 10^{-3} in this work). On average the methods required about 1.1 and 1.5 Newton iterations depending on whether gravitational forces were included. Furthermore, when the mobility stencil was lagged or averaging was used to determine the mobility values for the pressure equation, the solutions were qualitatively the same except with larger volume residuals at any given time step.

6.2 Immiscible and Partially Miscible Results

To demonstrate the benefits of multi-D upstream weighting and the robustness of the volume relaxed framework we present several homogeneous and heterogeneous test problems. The first test is a linear pressure driven test to demonstrate the preferential flow directions for the methods. The second test is a symmetric three well problem (one injector, two producers). This problem is run with and without gravity for both homogeneous and heterogeneous permeability fields. For the heterogeneous problem we present solution fronts for a single permeability realization as well as an ensemble average of solution fronts for many permeability realizations.

For the immiscible test we will consider water displacing a heavy oil. Water is assumed to be less viscous and more dense than the oil, as captured by using the viscosity ratio $\mu_o/\mu_w = 100$ and density difference $\rho_o/\rho_w = 1/2$. The relative permeability functions used are

$$k_{rw} = S_w^2 \text{ and } k_{ro} = S_o^4.$$

These relative permeability functions are nondecreasing functions on $S_\alpha \in [0, 1]$ and have the property $k_{r\alpha}(0) = 0$.

In section 6.2.3 we present results for the three well problem with a partially miscible model which results in a more complex mobility function as previously noted in section 2.5. Here we will use Koval's (1963) value for the mixing parameter. We conclude with a discussion of using multi-D upstream weightings for fully implicit simulation, section 6.2.4.

6.2.1 Linear Pressure Driven

The first test problem that we consider is a homogeneous reservoir with no incline. The domain is $(-1, 1) \times (-1, 1)$ which is discretized uniformly by a 100×100 grid of control volumes, hence the

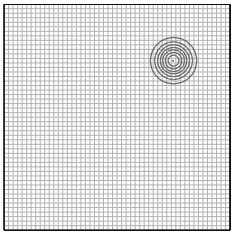

Figure 6.1: Initial water saturation for the pressure driven test, $S_w(x,y)$ =exp $\left[-200\left(x^2+y^2\right)\right]$. Contours are shown at 0.1, 0.2,. . . ,1.0.

spacing is $\Delta x = \Delta y = 1/100$. We start with initial masses of water and oil

$$M^0_{w,i,j} = \rho_w \exp\left[-200\left(((i-1/2)\ \Delta x)^2 + ((j-1/2)\ \Delta y)^2\right)\right],$$
$$M^0_{o,i,j} = \rho_o\left(1 - \exp\left[-200\left(((i-1/2)\ \Delta x)^2 + ((j-1/2)\ \Delta y)^2\right)\right]\right),$$

shown in Figure 6.1. Dirichlet pressure boundary conditions are used to create a preferential flow direction across the grid. The boundary cell pressures are set fixed at

$$p_{i,j} = 10 - (i-1/2)\ \Delta x\ \cos\theta - (j-1/2)\ \Delta y\ \sin\theta,$$

where θ defines the preferential flow direction. Hence $\theta = 0$ would result in flow in the negative x direction and $\theta = \pi/2$, flow in negative y direction. We set the CFL restriction for this test at 0.9 times the maximum allowed time step (Equation 4.15).

In Figure 6.2 we show the results for SPU, tight multi-D upstream weighting (TMU), and smooth multi-D upstream weighting (SMU), see section 4.6, for angles $\theta = 0$, $\pi/8$, and $\pi/4$. For the three different schemes we can make several observations. First, for $\theta = 0$ (Figures 6.2(a), 6.2(b), and 6.2(c)) all solutions are similar as the flow is close to grid aligned, and hence all three schemes closely resemble SPU.

For $\theta = \pi/8$ the effect of grid dependent differences becomes more apparent. SMU maintains an almost symmetric solution front with respect to the preferred flow direction though strong diffusive effects can be seen in the smoothing of the solution tip. For SPU (Figure 6.2(d)) and TMU (Figure 6.2(e)) solutions are not symmetric. SPU favors flow along the grid direction and TMU the diagonal to the grid lines, with the deviations of SPU being greater than TMU.

Finally, for $\theta = \pi/4$ all the methods again produce symmetric solutions. TMU shows strong preference for this flow angle, with SMU and SPU being significantly smeared. SPU shows a large amount of smearing in the cross-wind direction, whereas SMU is comparable to the solution front for $\theta = \pi/8$.

To summarize, this test demonstrates that SPU has a preferential flow direction along the grid

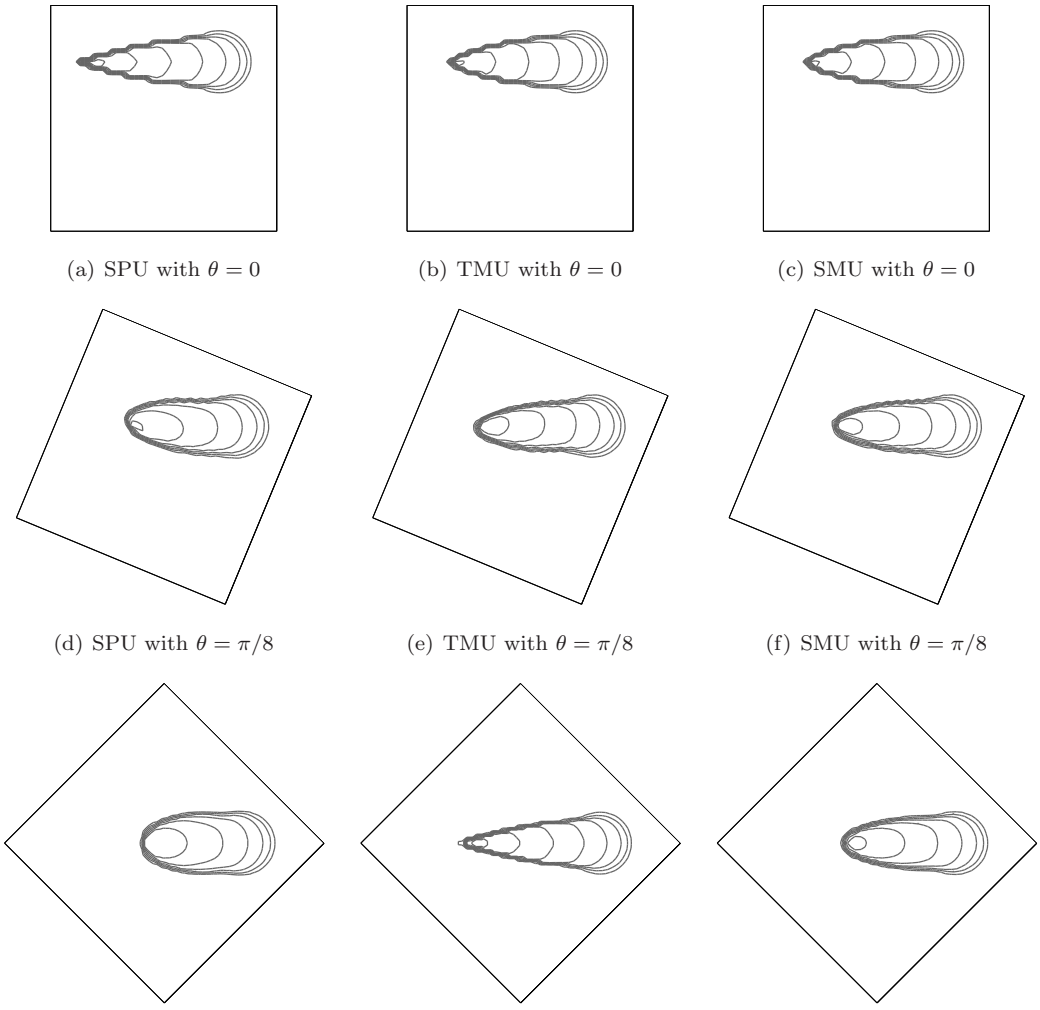

(a) SPU with $\theta = 0$ (b) TMU with $\theta = 0$ (c) SMU with $\theta = 0$

(d) SPU with $\theta = \pi/8$ (e) TMU with $\theta = \pi/8$ (f) SMU with $\theta = \pi/8$

(g) SPU with $\theta = \pi/4$ (h) TMU with $\theta = \pi/4$ (i) SMU with $\theta = \pi/4$

Figure 6.2: Immiscible linear pressure driven results for $\theta = 0$, $\pi/8$, and $\pi/4$ using SPU, TMU, and SMU. Results are computed on a 100×100 grid with the initial condition shown in Figure 6.1. Contours are shown at 0.025, 0.05, 0.075, ... 1.000. The portion of the domain shown is $x \in (-1/3, 2/3)$ and $y \in (-1/3, 2/3)$.

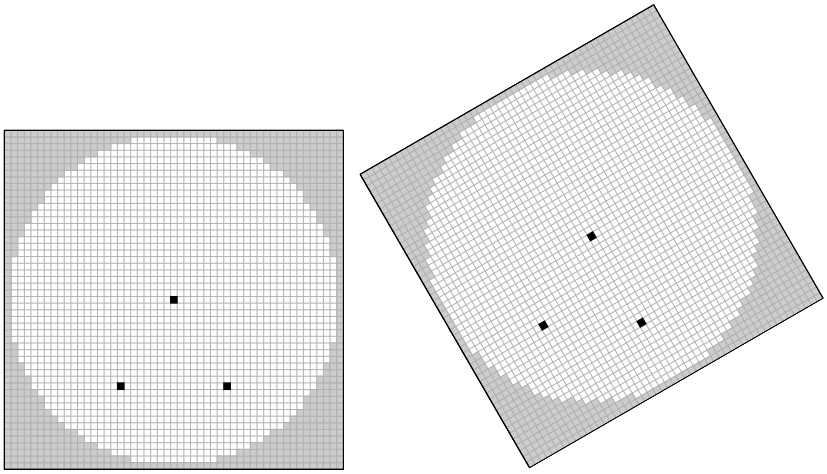

(a) $\theta = 0$ (b) $\theta = \pi/6$

Figure 6.3: Domain of the three well test problem for $\theta = 0$ and $\theta = \pi/6$. White cells are the interior region, the gray blocks are the boundary cells, and the black cells are the wells. The top well is the injection well, the bottom left production well one, and the bottom right production well two.

lines and TMU diagonal to the grid lines. SMU has a slight preference for flow along the grid directions, but maintains a largely symmetric front for non-grid aligned flow angles.

6.2.2 Three Well Test Problem

The next test we consider has one injector and two producers. The domain is $(-0.5, 0.5) \times (-0.5, 0.5)$ and is initially saturated with oil. This is discretized with a uniform 51×51 grid of control volumes. The grid spacing is $\Delta x = \Delta y = 1/51$ and the cell centers are located at $(x_{i,j}, y_{i,j}) = ((i-26)\Delta x, (j-26)\Delta y)$. The permeability field has two regions which we refer to as the interior and boundary regions with pointwise isotropic permeabilities K_{int} and K_{bound}. K_{int} can vary from grid block to grid block, whereas K_{bound} is constant for all boundary cells. Defining $r = \sqrt{x^2 + y^2}$, the interior region is all cells with cell centers $r < r_o$ and the exterior cells with $r \geq r_o$ where $r_o = (1 - \Delta x)/2$. The permeability field K_{int} can either be homogeneous or heterogeneous and the boundary permeability K_{bound} is homogeneous with permeability value $K_{bound} = 10^{-6} \min_{i,j}(K_{int})_{i,j}$. The two regions along with the grid are shown in Figure 6.3.

The wells are placed with respect to a secondary coordinate system defined as $(x', y') = (x \cos\theta + y \sin\theta, -x \sin\theta + y \cos\theta)$. The injection well is at $(x', y') = 0$, the first production well at $(x', y') = (0.3 \cos\psi, -0.3 \sin\psi)$, and the second production well at $(x', y') = (-0.3 \cos\psi, -0.3 \sin\psi)$, hence both production wells are equidistant from the injector at angle of ψ from the y' coordinate axis;

we use $\psi = \pi/6$. A fixed rate condition is used for the injection well, with rates $Q_{w,inj} = Q_{inj}$ and $Q_{r,inj} = 0$ (hence we inject only water or gas). For the production wells we use a fixed pressure condition and produce with rates proportional to the mobility of the fluid

$$Q_{\alpha,prod} = -Q_{prod}\frac{\lambda_\alpha}{(\lambda_o + \lambda_w)},$$

where Q_{prod} is obtained from the divergence of the pressure field in the well blocks. In Figure 6.3 the upper well is the injection well, the lower left production well one and lower right production well two.

For some tests we will also introduce an incline to the reservoir so that gravity forces affect the flow. To maintain the symmetry of the flow the gravitation force is oriented between the two production wells. This is done by setting the height of each control volume to

$$H_{i,j} = (1 - y'_{i,j}) \sin\zeta,$$

where $y'_{i,j} = -x_{i,j} \sin\theta + y_{i,j} \cos\theta$ corresponds to the grid block cell centers in the (x', y') coordinate system and ζ is the angle of the incline.

Homogeneous Test Without gravity

We begin by presenting results for a homogeneous interior region without gravity. The simulation is run for grid rotations of $\theta = 0$, $\pi/12$, $\pi/8$, $\pi/6$, and $\pi/4$. For the angles used in our tests, production well two is more aligned with the y-axis, and production well one is more aligned with the diagonal to the grid lines. The angle $\theta = \pi/12$ is chosen so that the line connecting the injector and production well one is exactly diagonal to the grid lines, a preferential flow direction for TMU. The angle $\theta = \pi/6$ was chosen to align the grid with the line connecting the injector and production well two, a preferential flow directions for SPU. Figure 6.4 shows the solution fronts at 0.1 pore volumes injected (PVI) for all the angles. The water cut, that is, the saturation of the water produced by a particular well, is shown in Figure 6.5.

From Figure 6.4 we see that SPU strongly prefers flow along the grid directions, which is particularly noticeable in the region above the injection well. TMU, on the other hand, prefers flow along the diagonal to the grid lines. SMU produces much more symmetric solution fronts over all the grid angles. These preferential directions are similar to what was observed in the simpler pressure driven test.

Typically in a field setting it is not the profiles of the fronts that are of most interest, but the integrated production data. This is the motivation for considering the water cut plots in Figure 6.5. The dashed line in the figures is the water cut for production well one and the solid line for production well two. The different shades of gray correspond to the angles, with black being $\theta = 0$ and the lightest gray for angle $\theta = \pi/4$. First observe that the spread of the results is greatest for SPU and

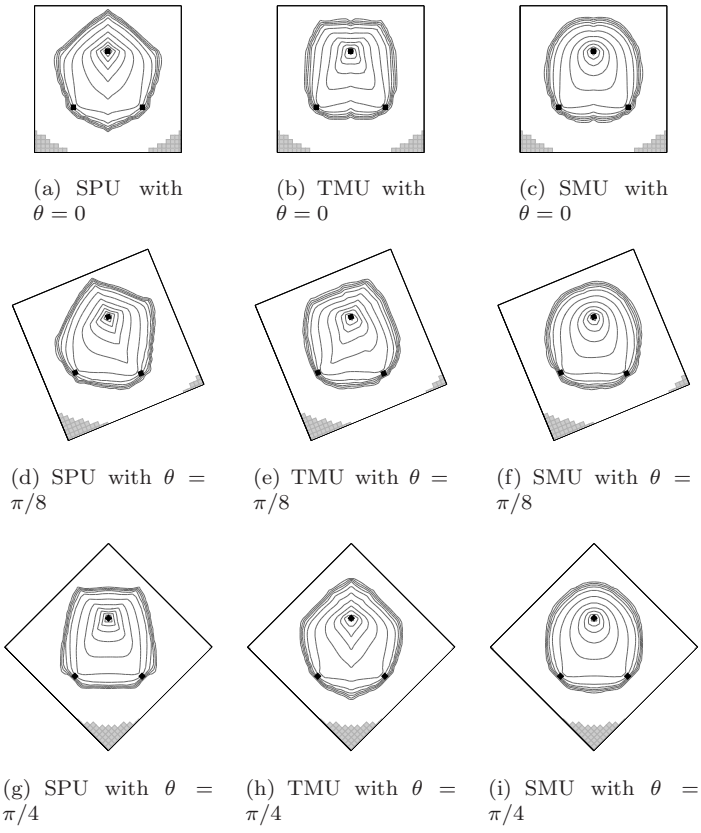

(a) SPU with $\theta = 0$

(b) TMU with $\theta = 0$

(c) SMU with $\theta = 0$

(d) SPU with $\theta = \pi/8$

(e) TMU with $\theta = \pi/8$

(f) SMU with $\theta = \pi/8$

(g) SPU with $\theta = \pi/4$

(h) TMU with $\theta = \pi/4$

(i) SMU with $\theta = \pi/4$

Figure 6.4: Results for the homogeneous three well problem for an immiscible displacement without gravity for SPU, TMU, and SMU. Fronts are shown at PVI = 0.1 over the region $x \in (x_0 + 1/3, x_0 - 1/3)$ and $y \in (y_0 + 1/3, y_0 - 1/3)$ where $(x_0, y_0) = (-1/10 \ \sin\theta, -1/10 \ \cos\theta)$. Solid gray grid cells are the boundary cells with low permeability.

least for SMU. This suggests that SMU is least affected by grid orientation for this test problem. Another observation is that SPU production well two, the more grid aligned production well, always breaks through before production well one, the production well more aligned to diagonal, except for the symmetric cases $\theta = 0$ and $\pi/4$ where the lines collapse onto one another. The opposite is true of TMU and SMU with production well one breaking through before production well two.

Homogeneous Test With gravity

In this test we add a gravitation force to problem, by introducing an incline in the domain at an angle of $\zeta = \pi/4$. Due to the density differences, the more buoyant phase (oil) will rise and the heavier phase (water) will sink. The gravitational force may act against the pressure force due to the wells causing the phases to move in different directions across a grid face. This is known as

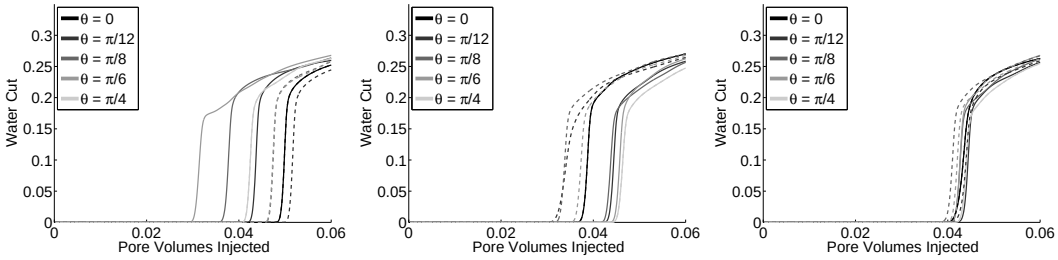

(a) SPU (b) TMU (c) SMU

Figure 6.5: Results for the homogeneous three well problem for an immiscible displacement without gravity for SPU, TMU, and SMU. The dashed line is production well one and the solid line production well two. The different line shades correspond to different angles, as indicated in the legend. For $\theta = 0$ the gridding leads to an exactly symmetric solution hence the two well plots lie directly on top of one another. This is also the case for $\theta = \pi/4$.

countercurrent flow. The balance between the injection and the gravitational force can be measured through the definition of the non-dimensional gravity number

$$N_G = \frac{(\rho_w - \rho_o) g \sin \zeta}{(\mu_o + \mu_w) q_{inj}}.$$

In our work we let $N_G \approx 1.6803$. The higher N_G the more important gravitational forces are as opposed to viscous and well forces.

We run this test with the same angles as in the previous test: $\theta = 0$, $\pi/12$, $\pi/8$, $\pi/6$, and $\pi/4$. Regardless of the angle θ, the gravitational force always acts directly between the two production wells along the y'-axis. Solution fronts for select angles are presented in Figure 6.6. The Figure shows that, as in the non-gravity case, SPU prefers the directions corresponding to the grid lines. The artificial updip kink in the solution front for SPU is more significant for the grid direction most aligned with the gravitational field and less so for the other grid direction. Also, the fluid flows further downdip along the grid direction most aligned with the gravitation force. TMU strongly prefers the diagonal to the grid directions. The preference is most significant downdip. The updip kink in TMU results shows less preference than SPU. SMU shows the most isotropic results. This is similar to the previously presented results.

We present the water cut plots for all the angles in Figure 6.7. Once again the spread of the curves is greatest for SPU with production well two always breaking through before production well one. TMU always leads to production well two breaking through before production well one. SMU shows the tightest clustering of the curves with production well two breaking through before production well one.

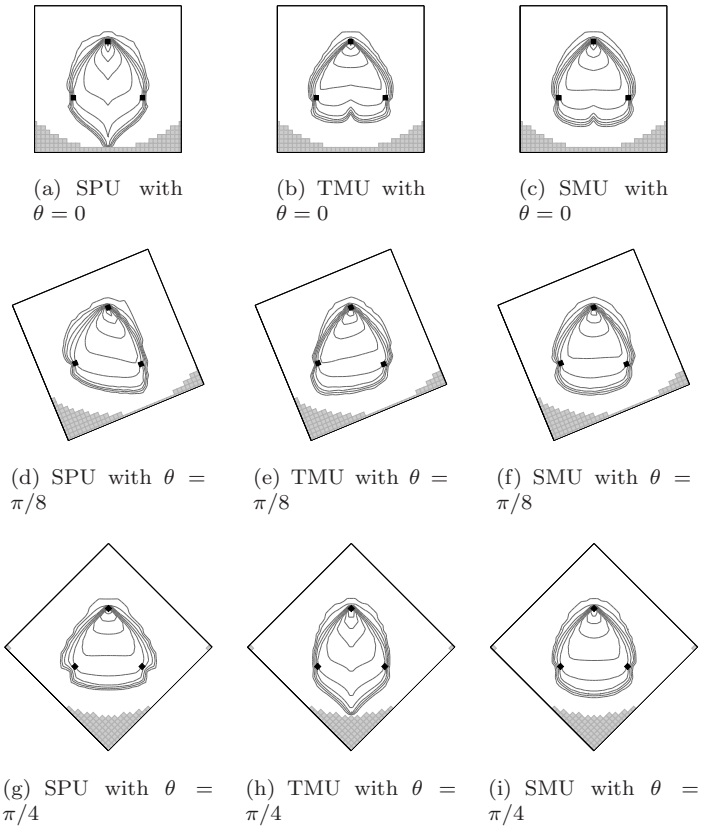

(a) SPU with $\theta = 0$ (b) TMU with $\theta = 0$ (c) SMU with $\theta = 0$

(d) SPU with $\theta = \pi/8$ (e) TMU with $\theta = \pi/8$ (f) SMU with $\theta = \pi/8$

(g) SPU with $\theta = \pi/4$ (h) TMU with $\theta = \pi/4$ (i) SMU with $\theta = \pi/4$

Figure 6.6: Results for the homogeneous three well problem for an immiscible displacement including gravity for SPU, TMU, and SMU. Fronts shown at PVI = 0.06 over the region $x \in (x_0+1/3, x_0-1/3)$ and $y \in (y_0+1/3, y_0-1/3)$ where $(x_0, y_0) = (-3/40\ \sin\theta, -3/40\ \cos\theta)$. Solid gray grid cells are the boundary cells with low permeability.

Heterogeneous Three Well Problem

In the presence of heterogeneity, it is less clear how numerical errors contribute to biasing of the schemes. This is due to the presence of preferential flow paths defined by the permeability field. To understand how the numerical errors affect the solutions in the presence of heterogeneity, we simulate this same displacement with random permeability fields and compute an ensemble average of the results. We use sequential Gaussian simulation (Deutsch and Journel, 1998) to generate log-normally distributed permeability fields of dimensions 51×51 on a unit square. The dimensionless correlation length is set at $\lambda = 5/51$, corresponding to a correlation length of 5 grid blocks. The mean of $\ln K$ is fixed at 3.0. The standard deviation, σ, of the $\ln K$ is $\sigma = 0.5$, corresponding to a permeability contrast of approximately $\min(K)/\max(K) \sim 3 \times 10^{-2}$. The grid angle is $\theta = \pi/8$ and 100 solution realizations are used for the ensemble average.

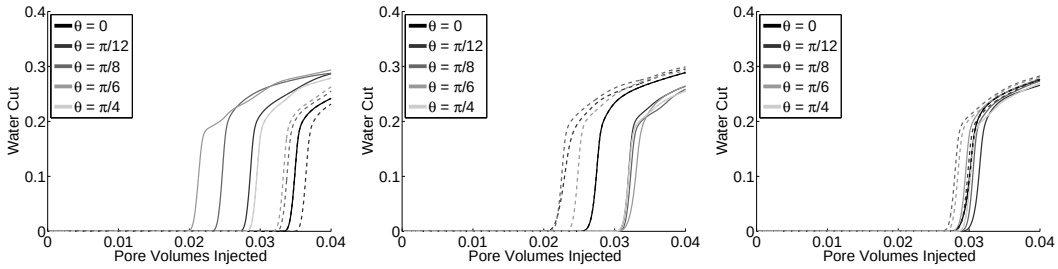

(a) SPU (b) TMU (c) SMU

Figure 6.7: Results for the homogeneous three well problem for an immiscible displacement with gravity for SPU, TMU, and SMU. The dashed line is production well one and the solid line production well two. Different line shades correspond to different angles, as indicated in the legend.

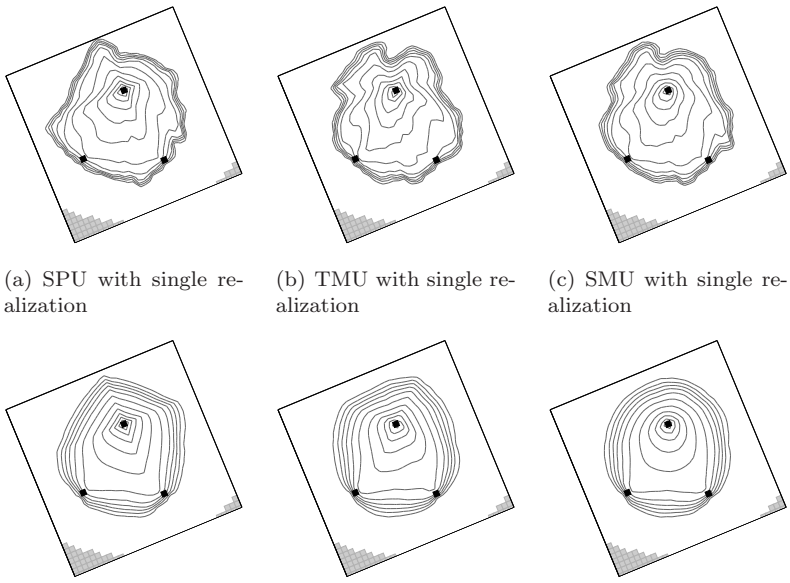

(a) SPU with single realization (b) TMU with single realization (c) SMU with single realization

(d) ensemble average of SPU solutions (e) ensemble average of TMU solutions (f) ensemble average of SMU solutions

Figure 6.8: Results for the heterogeneous three well problem for an immiscible displacement without gravity for SPU, TMU, and SMU and permeability contrast $k_{\min}/k_{\max} = 3 \times 10^{-2}$. The grid rotation angle is $\theta = \pi/8$. Fronts shown at PVI $= 0.1$ over the region $x \in (x_0 + 1/3, x_0 - 1/3)$ and $y \in (y_0 + 1/3, y_0 - 1/3)$ where $(x_0, y_0) = (-1/10 \ \sin\theta, -1/10 \ \cos\theta)$. Solid gray grid cells are the boundary cells with low permeability.

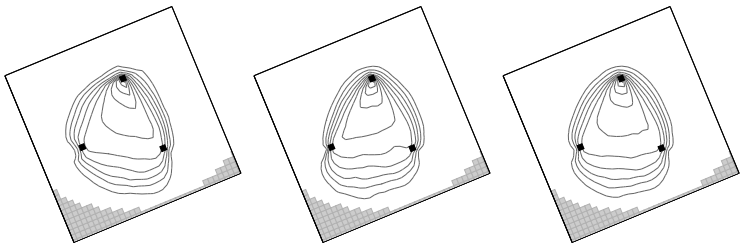

(a) SPU average (b) TMU average (c) SMU average

Figure 6.9: Ensemble average of 100 solution fronts for the heterogeneous three well problem with permeability contrast is $k_{\min}/k_{\max} = 3 \times 10^{-2}$. The displacement is immiscible and includes gravity. The schemes used are SPU, TMU, and SMU. The grid rotation angle is $\theta = \pi/8$. Fronts shown at PVI = 0.1 over the region $x \in (x_0 + 1/3, x_0 - 1/3)$ and $y \in (y_0 + 1/3, y_0 - 1/3)$ where $(x_0, y_0) = (-1/10 \ \sin\theta, -1/10 \ \cos\theta)$. Solid gray grid cells are the boundary cells with low permeability.

The solution fronts with no gravitational force, $\zeta = 0$, at 0.1 PVI for both a single permeability realization and the ensemble average are shown in Figure 6.8. For the single permeability realization it is difficult to see the affect of the computational grid and the numerical errors. This is due to the preferential nature expected from the permeability field. The utility of ensemble averaging is that it can reveal these affects, since if the number of realizations is sufficiently large, the average converges to a (potentially biased) solution.

The averaged results for SPU and TMU are similar to the homogeneous results. SPU is strongly preferring flow along the grid directions and TMU diagonal to the grid lines. SMU, on the other hand, seems less sensitive to the grid in the presence of heterogeneity, as was the case for the homogeneous test. For other angles the results are similar. If the permeability contrast is increased, the results show less bias, with SPU continuing to show the strongest bias.

The ensemble average with gravity, using the same gravity number as in section 6.2.2, at 0.06 PVI is shown in Figure 6.9. The average shows strong dependence for SPU along the grid directions and diagonal to the grid directions for TMU, which is similar to what was seen in the homogeneous test with gravity. The biasing near the injector is more apparent updip. SMU shows less sensitivity to grid orientation, as in the previous tests. Similar results are seen for other grid angles.

6.2.3 Partially Miscible Model

As shown in section 4.7, the developed methods extend to general mobility functions. To demonstrate that the methods perform well with more general mobility functions, we run the three well test again for a homogeneous permeability with a gravity number of $N_G \approx 0.45$. We show the solution fronts and gas/oil ratios in Figures 6.10 and 6.11, respectively. The method maintains monotonicity and physical saturations, as expected, with both nonconvex mobility functions and countercurrent flow.

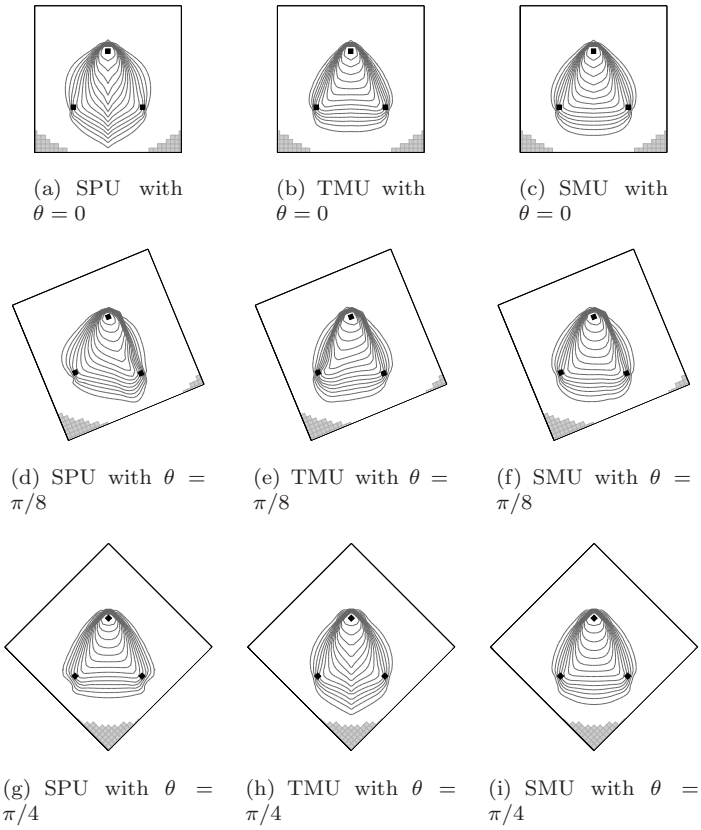

(a) SPU with $\theta = 0$ (b) TMU with $\theta = 0$ (c) SMU with $\theta = 0$

(d) SPU with $\theta = \pi/8$ (e) TMU with $\theta = \pi/8$ (f) SMU with $\theta = \pi/8$

(g) SPU with $\theta = \pi/4$ (h) TMU with $\theta = \pi/4$ (i) SMU with $\theta = \pi/4$

Figure 6.10: Results for the homogeneous three well problem with gravity using the partially miscible model for SPU, TMU, and SMU. Fronts are shown at PVI = 0.1 over the region $x \in (x_0 + 1/3, x_0 - 1/3)$ and $y \in (y_0 + 1/3, y_0 - 1/3)$ where $(x_0, y_0) = (-1/10 \ \sin\theta, -1/10 \ \cos\theta)$. Solid gray grid cells are the boundary cells with low permeability.

The results are comparable to the previous immiscible results with SPU showing strong bias along the grid lines and TMU diagonal to the grid lines. SMU still produces rather isotropic solution fronts and gas/oil ratios.

6.2.4 Fully Implicit Simulation

We close this chapter by demonstrating how multi-D upstream weightings can be used for fully implicit simulation, that is, solving for both the pressure and mass concentrations variable implicitly in time. Here we wish to show that the multi-D weightings at the same rate, or faster, than SPU even with the more complex weightings. We therefore will not be using the volume relaxed framework as we did in the explicit case and instead will define the saturation of water as $S_w = C_w/\rho_w$ and the saturation of oil as $S_o = 1 - S_w$. Other variable choices are possible (Aziz and Wong, 1989)

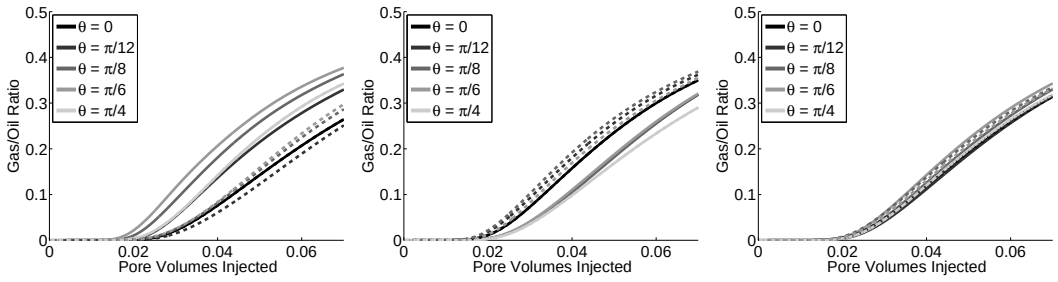

(a) SPU (b) TMU (c) SMU

Figure 6.11: Results for the homogeneous three well problem with gravity using the partially miscible model for SPU, TMU, and SMU. The dashed line is production well one and the solid line production well two. The different line shades correspond to different angles, as indicated in the legend.

and could be explored in future work. An advantage of the fully implicit framework is that it allows for unrestricted time steps assuming that the necessary nonlinear iterations converge. Here we only explore the most straightforward implementation of Newton's method, but more complex iteration strategies are possible, such as those described by Appleyard and Cheshire (1982), Kwok and Tchelepi (2007), and Younis et al. (2009).

For our variable choice we have the nonlinear system of equations

$$\boldsymbol{F}(\boldsymbol{P}, \boldsymbol{C}_w) = \begin{pmatrix} \boldsymbol{F}_p(\boldsymbol{P}, \boldsymbol{C}_w) \\ \boldsymbol{F}_w(\boldsymbol{P}, \boldsymbol{C}_w) \end{pmatrix} = \begin{pmatrix} \sum_{\alpha=o,w} \left(\mathbf{Div} \left(\bar{\boldsymbol{\lambda}}_\alpha(\boldsymbol{S}_w, \boldsymbol{P}) \bullet \boldsymbol{\sigma}_\alpha \right) - \boldsymbol{Q}_\alpha \right) \\ \boldsymbol{C}_w - \boldsymbol{C}_w^n + \Delta t \boldsymbol{V}^{-1} \rho_w \left(\mathbf{Div} \left(\bar{\boldsymbol{\lambda}}_w(\boldsymbol{S}_w, \boldsymbol{P}) \bullet \boldsymbol{\sigma}_w \right) - \boldsymbol{Q}_w \right) \end{pmatrix},$$

where we are trying to find values for $\boldsymbol{P}^{n+1}$ and $\boldsymbol{C}_w^{n+1}$ such that $\boldsymbol{F}(\boldsymbol{P}^{n+1}, \boldsymbol{C}_w^{n+1}) = \mathbf{0}$. The Jacobian matrix of this system is

$$\boldsymbol{J}(\boldsymbol{P}, \boldsymbol{C}_w)^T = \begin{pmatrix} \boldsymbol{J}_{pp}(\boldsymbol{P}, \boldsymbol{C}_w)^T & \boldsymbol{J}_{cp}(\boldsymbol{P}, \boldsymbol{C}_w)^T \\ \boldsymbol{J}_{pc}(\boldsymbol{P}, \boldsymbol{C}_w)^T & \boldsymbol{J}_{cc}(\boldsymbol{P}, \boldsymbol{C}_w)^T \end{pmatrix},$$

where

$$\boldsymbol{J}_{pp}(\boldsymbol{P},\boldsymbol{C}_w)^T = \sum_{\alpha=o,w}\left(\mathbf{Div}\left(\operatorname{diag}\left(\bar{\boldsymbol{\lambda}}_\alpha(\boldsymbol{S}_\alpha,\boldsymbol{P})\right)\boldsymbol{T} + \operatorname{diag}\left(\boldsymbol{\sigma}_\alpha(\boldsymbol{P})\right)\left(\frac{\partial\bar{\boldsymbol{\lambda}}_\alpha}{\partial\boldsymbol{P}}\right)\Big|^T_{(\boldsymbol{P},\boldsymbol{C}_w)}\right) - \left(\frac{\partial\boldsymbol{Q}_\alpha}{\partial\boldsymbol{P}}\right)\Big|^T_{(\boldsymbol{P},\boldsymbol{C}_w)}\right),$$

$$\boldsymbol{J}_{cp}(\boldsymbol{P},\boldsymbol{C}_w)^T = \sum_{\alpha=o,w}\left(\mathbf{Div}\left(\operatorname{diag}\left(\boldsymbol{\sigma}_\alpha(\boldsymbol{P})\left(\frac{\partial\bar{\boldsymbol{\lambda}}_\alpha}{\partial\boldsymbol{C}_\alpha}\right)\Big|^T_{(\boldsymbol{P},\boldsymbol{C}_w)}\right) - \left(\frac{\partial\boldsymbol{Q}_\alpha}{\partial\boldsymbol{C}_\alpha}\right)\Big|^T_{(\boldsymbol{P},\boldsymbol{C}_w)}\right),$$

$$\boldsymbol{J}_{pc}(\boldsymbol{P},\boldsymbol{C}_w)^T = \Delta t\boldsymbol{V}^{-1}\mathbf{Div}\left(\operatorname{diag}\left(\bar{\boldsymbol{\lambda}}_w(\boldsymbol{S}_w,\boldsymbol{P})\right)\boldsymbol{T} + \operatorname{diag}\left(\boldsymbol{\sigma}_w(\boldsymbol{P})\right)\left(\frac{\partial\bar{\boldsymbol{\lambda}}_w}{\partial\boldsymbol{P}}\right)\Big|^T_{(\boldsymbol{P},\boldsymbol{C}_w)}\right),$$

$$\boldsymbol{J}_{cc}(\boldsymbol{P},\boldsymbol{C}_w)^T = I + \Delta t\boldsymbol{V}^{-1}\left(\mathbf{Div}\left(\operatorname{diag}\left(\boldsymbol{\sigma}_w(\boldsymbol{P})\left(\frac{\partial\bar{\boldsymbol{\lambda}}_w}{\partial\boldsymbol{C}_w}\right)\Big|^T_{(\boldsymbol{P},\boldsymbol{C}_w)}\right) - \left(\frac{\partial\boldsymbol{Q}_w}{\partial\boldsymbol{C}_w}\right)\Big|^T_{(\boldsymbol{P},\boldsymbol{C}_w)}\right).$$

Here the additional terms that arise due to the more complex stencil are $\frac{\partial\bar{\boldsymbol{\lambda}}_\alpha}{\partial\boldsymbol{p}}$. These terms are zero for SPU but must be included for more general schemes. For our proposed multi-D schemes, the derivatives can be computed with only minimal additional work, as shown in subsection 4.5.1.

To test the fully implicit method (FIM) with multi-D upwinding we run the three well test for an immiscible waterflood. We inject 0.01 PVI in every time step and call this the global time step. If Newtons method fails to converge within 10 iterations or if the saturation of water becomes greater than 2 or less that -1, we cut the time step in half. When a sufficient number of cut time steps are taken so that the simulation reaches the point that the global time step would have reached, we try the global time step again. In Figure 6.12 we show solution fronts for SPU, TMU, and SMU for angle $\theta = \pi/6$ both with and without gravitational forces to demonstrate the FIM suffers from the same grid dependent effects as the IMPEM method. The FIM method introduces increased amounts of longitudinal, or streamline, diffusion but these are not sufficient to remove the biasing of the solution. Other angles show similar behavior.

In Tables 6.1 and 6.2 we show the nonlinear iteration information. The results indicate that the multi-D methods perform as well or better than SPU in all the tests both in terms of total number of iterations and number of time step cuts. The average number of iterations for a convergent step is fairly consistent over all the methods, but in the case without gravity, the TMU and SMU schemes do better. In the case with gravity the SMU scheme does slightly worse than SPU in terms of average number of iterations but still has less total iterations because of the decreased number of time step cuts.

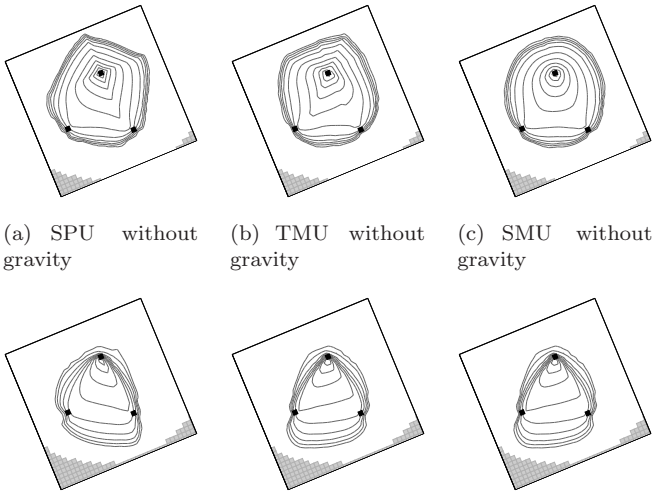

(a) SPU without gravity (b) TMU without gravity (c) SMU without gravity

(d) SPU with gravity (e) TMU with gravity (f) SMU with gravity

Figure 6.12: Immiscible three well problem results for $\theta = \pi/8$ using SPU, TMU, and SMU. Fronts are shown at PVI = 0.1 over the region $x \in (x_0 + 1/3, x_0 - 1/3)$ and $y \in (y_0 + 1/3, y_0 - 1/3)$ where $(x_0, y_0) = (-1/10\ \sin\theta, -1/10\ \cos\theta)$. Solid gray grid cells are the boundary cells with low permeability.

	SPU			TMU			SMU		
θ	Number of cuts	Average iterations	Total iterations	Number of cuts	Average iterations	Total iterations	Number of cuts	Average iterations	Total iterations
0	7	10.2	117	3	8.5	80	3	8.2	79
$\pi/12$	8	10.1	131	2	8.3	72	4	8.8	91
$\pi/8$	8	10.6	122	3	9.1	87	3	8.3	77
$\pi/6$	6	10.7	113	4	8.7	88	3	8.5	80
$\pi/4$	4	9.5	98	3	8.4	82	3	8.5	80

Table 6.1: Iteration counts for FIM without gravity. Average iterations are for converged time step (does not include cuts); total iterations includes time step cuts.

	SPU			TMU			SMU		
θ	Number of cuts	Average iterations	Total iterations	Number of cuts	Average iterations	Total iterations	Number of cuts	Average iterations	Total iterations
0	9	15.5	138	7	15.8	103	7	16.1	108
$\pi/12$	8	15.1	122	8	16.9	127	7	16.3	111
$\pi/8$	10	17.1	143	8	14.7	120	7	16.4	112
$\pi/6$	9	15.7	134	7	16.1	109	7	16.3	111
$\pi/4$	6	14.7	101	5	12.5	86	7	16.0	110

Table 6.2: Iteration counts for FIM with gravity. Average iterations are for converged time step (does not include cuts); total iterations includes time step cuts.

Chapter 7

Future Work

7.1 Forcing Methods

The forcing methods developed in chapter 3 show considerable promise in reducing GOE. There is still interesting work to be done. Stability analysis of the LETIS method would be a useful contribution, and similar analysis has been done for related immersed boundary methods (Gustafsson, 2007; Mittal and Iaccarino, 2005). As noted in the text, we found that the LETIS methods did not impact the time step selection. This is likely due to the fact that the well terms tend to be the controlling factor in time step selection for our problems, but in other applications this may not be the case. More detailed analysis of the method may reveal this.

The development of near-well models is something being pursued by many researchers (Mascarenhas and Durlofsky, 2000; Muggeridge et al., 2002). This is important for the forcing methods because the analytic models we have assumed only hold for a homogeneous porous medium. To robustly incorporate these methods, coupling methods will need to be developed between the near-well and interior regions. The coupling methods will need to incorporate the proper boundary conditions and transfer between the possibly different physics in the two regions. Though this work will need to draw upon methods from the multiscale modelling literature, our problems, as we have seen, can be very unstable and sensitive to errors. New techniques will thus be needed. The coupling and imposed boundary conditions will be different for both methods. Continued research may also lead to a conservative formulation of the well-sponge method which may allow for a larger coupling region and hence less grid sensitivity.

SBAV performed very well with both of the well modelling methods, but is not applicable for general reservoir simulation. This suggests that the truly multi-D methods that we have developed in this thesis should perform favorably when combined with the well forcing methods. The question of how to trace the characteristics for interaction regions close to the near-well region needs to be addressed, but as noted above, there has been some work in the immersed boundary literature which

can help to address these open problems (Helzel et al., 2005; LeVeque, 2003).

7.2 Multi-D Transport

There are several extensions of this work that can be pursued in the future. First, the results of chapters 5 and 6 apply to general grid topologies, but the methods have only been implemented for Cartesian grids. An efficient and robust implementation of the methods on general grid topologies, perhaps coupled with a general MPFA framework, would be a significant contribution. Lamine and Edwards (2008) have recently proposed a different class of multi-D transport methods for multi-phase flow in porous media with particular emphasis on unstructured grids. An implementation of the interaction region framework for transport has been developed for Cartesian adaptive meshes and has been coupled with the VCMP method, and the results were favorable(Lambers et al., 2009). An extension to 3-D could be done by using multi-D in the areal and SPU in the vertical, but it is possible to develop a fully coupled interaction region based method for 3-D transport. In this case there would be more flow directions to consider as well as more choices of interpolation points since there are more degrees of freedom. Even for the 3-D constant velocity problem there is not a single parameter family of schemes but a three (coupled) parameter family of schemes (Roe and Sidilkover, 1992; Van Ransbeeck and Hirsch, 1997).

Another interesting topic would be to investigate why the seemingly "optimal" scheme for the scalar advection framework and the nonlinear model are different. To do this it will be necessary to more completely understand the differences between tracing on the total velocity field as opposed to the phase flux field. Performing fluid stability analysis in a manner similar to that done by (Riaz and Meiburg, 2004) using the phase flux field instead of the total velocity field may also be necessary.

The schemes presented in chapter 6 extend in a fairly straightforward manner to n_p-phase flow problems assuming no mass transfer between the phases. The incorporation of mass transfer, even for the two-phase case, could introduce complications since phase interactions may make the definition of a monotone multi-D upwind state more difficult. Continued use a phase-based upstream weighting strategy will likely reduce these complications as it avoids the need to do characteristic decomposition, and is commonly used in practice (Sammon, 1988; Brenier and Jaffré, 1991). A natural place to start a study of this would be to look at the three-phase, three-component (water, oil, gas) black oil model. In this model, the oil and water components only exist in their respective phases, and the gas component can exist in the gas and oil phases, but with the gas solubility of the oil phase strictly a function of the gas pressure (Aziz and Settari, 1979). Compositional extensions should be considered as these are the class of problems that will be most unstable. The inclusion of capillary effects should not introduce any major complications for the nonlinear framework in Darcy form, as these effects would only effect the σ_α values, and hence would not effect the monotonicity of the schemes outline in section 4.6. If the fractional flow form of the equations is used, capillary effects

have a similar effect as gravity (Aziz and Settari, 1979) and hence the methods multi-D methods developed in chapter 4, such as tight multi-D upstream weighting and smooth multi-D upstream weighting, are not appropriate.

More work might also be invested in developing a multi-D method for more general scalar non-linear equations, that is, equations of the form

$$\frac{dc}{dt} + \nabla \cdot \begin{pmatrix} f(c) \\ g(c) \end{pmatrix} = 0,$$

where it is not assumed that $f'(c)/g'(c)$ is a constant independent of c. Also, higher-order methods should be investigated. It is not apparent how to construct and limit slopes for interaction based methods. LeVeque's (1997) work on wave oriented methods as well as the residual distribution literature (Deconinck and Koren (1997); Deconinck et al. (2003); and the references therein) will likely inform this work.

Chapter 8

Conclusions

The primary goal of this work has been to lessen the grid dependent nature of important numerical errors, whether these errors arose from the initial near-well flow or the interior discretization used for transport. Numerical simulations of adverse mobility ratio flows are highly sensitive to numerical errors, as these errors can trigger unstable modes in the solution. Therefore, numerical solutions may change significantly with grid refinement or changes in the orientation of the computational grid with respect to the primary flow direction. In this work we do not seek to remove the physical instability present in the system, as doing this would require adding an unreasonably large amount of grid independent physical diffusion (Tan and Homsy, 1997; Riaz and Meiburg, 2004) and thus drastically change the physics of the displacement. Instead, we want to allow the underlying rock properties to trigger the physical instability instead of the numerical errors.

Throughout this work we have aimed to develop practical methods which can be used with a variety of simulation strategies, gridding systems, and discretizations. We have exclusively used Cartesian grids as they allow for easy comparison of the methods and understanding of the impact of the various numerical errors. Furthermore, as noted in the introduction, many applications within reservoir simulation require the use of structured, or nearly-structured grids, so we do not want our gridding strategy to be determined in order to eliminate grid dependency. Unless otherwise noted in the text, we expect no trouble in extending the outlined methods to more general grid topologies.

We have established that the grid orientation effect and other grid dependencies largely arise from:

- an underlying physical instability in high mobility ratio flows
- the flow in the immediate vicinity of the injection well
- errors in the transport discretization that are largely grid dependent.

This thesis was split into two parts: the development of methods to force solutions around the

injection well and multi-D transport discretizations which control the structure of the first order numerical errors.

In order to reduce errors around the injection well we developed two forcing methods: the well-sponge and LETIS (chapter 3). In the well-sponge method cell averages were forced using a penalty method. Though not completely non-intrusive, the well-sponge method did not require the modification of the flux calculation and was implemented as a correction step on top of the original time stepping methodology. The drawback of the well-sponge was that it was not conservative, so we also developed LETIS, or local embedding through immersed structures. In this method the near-well region defined cut faces. On these cut faces a portion of the flux came from the assumed near-well solution, and the other portion of the flux came from the numerical method used for transport or flow. This was more intrusive than the well-sponge method in that it required modification of the flux calculation and the pressure discretization, but it had the added benefit of being fully mass conservative. Both methodologies drastically reduced GOE caused by the injection well as was demonstrated for two miscible gas injection problems. Both of these strategies increased the simulation cost only during the initial injection period because once the front had passed through the near-well region the integrals became constant in time.

In order to control the errors in the interior of the simulation domain, multi-D transport methods were developed in chapter 4. While single point upstream weighting (SPU) is popular within reservoir engineering for its simplicity, it results in numerical errors which are strongly correlated with the computational grid. We began by presenting modified equations analysis for a family multi-D schemes (Roe and Sidilkover, 1992; Van Ransbeeck and Hirsch, 1997). This analysis showed that incorporation of flow information into the computational stencil changed the first order diffusive error. In multiple dimensions there is not a scalar first order error, but a numerical diffusion tensor whose structure depends on the discretization and local flow information. For miscible displacements in the fractional flow framework, the structure of the error tensor in the flow aligned coordinate system largely predicted the structure of the grid dependency.

In chapter 4 we also developed a new framework that generalized the family of multi-D finite difference schemes to rough velocity fields and a class of nonlinear equations. The generalization was based on a local coupling through interaction regions which maintained as much flow information in the scheme as possible. This local coupling allowed us to rigorously prove and ensure that the methods remained monotone and fully generalized to arbitrary grid topologies in 2-D. We proposed two purely upstream multi-D schemes: tight multi-D upstream weighting (TMU) and smooth multi-D upstream weighting (SMU). The two limiting members of the purely upstream family of discretizations were SPU and TMU with SMU existing in between the limits. The equivalence of TMU to the N-scheme (Roe and Sidilkover, 1992) and SMU to Koren's methods (Koren, 1991) was shown for constant scalar advection. As all of these methods are phase based methods, they are directly usable within the current reservoir methodology (Aziz and Settari, 1979). The methods

also assumed nothing about the underlying pressure discretization, making them usable with the multi-point flux approximations which are becoming increasingly important.

A novel method called the Flat Scheme was also introduced in this thesis. This method is for scalar advection, is positive for arbitrary divergence free velocity fields, and has minimal constant transverse diffusion. The effect of this diffusion property is that the strength of the preferential flow directions are reduced for the unstable flow problems as the strength of the instability is largely related to the transverse diffusion (Riaz and Meiburg, 2004).

For both scalar (chapter 5) and nonlinear (chapter 6) problems the use of multi-D methods was shown to reduce grid dependency over SPU. This was demonstrated for a number of homogeneous as well as heterogeneous problems. For heterogeneous problems it was necessary to consider an ensemble average of many simulation results to properly assess the effects of the numerics. As the permeability contrast was increased, the average solution showed less dependence on the grid. For the scalar problem TMU performed most favorably of all the purely upstream schemes, and the Flat Scheme, TMU with an additional numerical diffusion term, performed even more favorably. For the nonlinear problems SMU performed most favorably, but it is our opinion that this is a model and a formulation dependent result which requires more study (see chapter 7). One possible method to initially assess whether GOE is a concern for a given simulation project would be to run the problem with both SPU and one or more of the multi-D methods. Drastically different results would suggest that some method of assessing and handling modelling error must be used.

In order to increase the robustness of multiphase simulation, a relaxed volume framework was developed in chapter 6. The key property of this framework was that it robustly handled volume errors in the pressure equation so as to preserve both physical mass and saturation values. This was necessary as more complex transport schemes result in a more nonlinear discrete pressure equation, and inconsistency between the transport and pressure discretizations can result in nonphysical grid values. This framework was only used when handling the transport equation in an explicit manner. Finally, we also demonstrated how multi-D discretizations can be used for fully implicit simulation. Multi-D discretizations seemed to increase the speed and domain of convergence for Newton's method, though this is certainly something that warrants further analysis and work.

In summary this Ph.D. work has provided the following specific contributions:

- Grid orientation effects are largely caused by the interaction of a physically unstable flow with grid dependent numerical errors. These errors arise from both perturbations set up by the handling of the injection well and the numerical discretization used in the interior.

- A combination of reducing the rotational sensitivity of numerical errors in the finite difference scheme and forcing the flow in the immediate neighborhood of the injection well was shown to reduce or remove grid orientation effects.

- Two forcing methods, the well-sponge and LETIS, were proposed that significantly reduced

grid orientation effects. This was demonstrated for a homogeneous miscible model problem. The LETIS method maintains conservation to round-off error.

- A general framework for multi-D schemes, for both scalar advection and a class of scalar nonlinear equations, with local stability constraints, can be formulated using interaction regions.
- Modified equations analysis can be used in a predictive manner for determining preferential flow angles on structured grids for the presented miscible model within the scalar advection framework.
- Two purely upstream biased multi-D schemes were presented, tight multi-D upstream weighting and smooth multi-D upstream weighting. Both methods significantly reduce grid orientation effects and numerical biasing over the commonly used single point upstream weighting method.
- The Flat scheme was also introduced in this thesis for scalar advection problems. The scheme is positive, has minimal constant transverse diffusion, and reduces the strength of the preferential flow directions.
- A volume relaxed framework for nonlinear simulation was introduced. This framework handled volume errors in the pressure equation to preserve physical mass and saturation values.

There are several areas in which this work should be continued, for a more detailed discussion see chapter 7. More complex near-well models should be explored for use with the forcing methods. This will require the development of coupling methods for enforcing boundary conditions. The multi-D upstream weighting methods should also be incorporated into the forcing methods. Development of a simulator using multi-D upstream weightings along with more general pressure discretizations and grid toplogies would be a significant contribution. Extension of the multi-D schemes to systems of equations which model more complex physics, such as the black oil model, compositional simulation, and steam injection problems, should also be considered. Finally, the development of higher-order multi-D methods based on multi-D limiters may help to reduce grid orientation even further and are therefore worth exploring.

Appendix A

Positivity of the Flat Scheme

In this appendix we demonstrate that the Flat scheme as defined in section 4.8 and Table 4.2 is a positive scheme. Recall that the Flat scheme is for scalar advection in a divergence free velocity field. We represent this as

$$c_t + \nabla \cdot (\boldsymbol{u}c) = 0 \tag{A.1}$$

where $\nabla \boldsymbol{u} = 0$. Since we will only be considering scalar advection, we do not use the σ and ζ notation as in chapter 4, but instead use U and C.

Given the definition of the Flat scheme, we first note that a half-face k can only have a diffusive flux correction if $U_{k-1} \geq 0$ and $U_{k+1} \leq 0$. This means that at most two half-faces of the interaction region can have a diffusive flux correction. Of the 16 possible volumetric flux sign configurations, four will have two diffusive flux corrections and eight will have one diffusive flux correction. For this reason, without loss of generality, we can consider the case $U_2 \geq 0$, $U_1 \geq 0$, $U_3 \leq 0$, and hence there is a diffusive correction on half-face 2. If $U_4 \leq 0$, then there is also a diffusive correction on half-face 3 and otherwise there is no other diffusive correction for the interaction region. All other cases are handled by symmetry or admit no diffusive correction thus reducing the Flat scheme to the N-scheme which has already been shown to be positive.

For the case that $U_4 > 0$ there is only a diffusive correction on half-face 2 and hence the only (a_k, b_k) pair which is potentially non-zero is (a_2, b_2). It will be seen that in the case when $U_4 \leq 0$, and thus (a_3, b_3) may be non-zero, we need only consider (a_2, b_2) since the constraints on the values of (a_2, b_2) and (a_3, b_3) are not coupled. To do this we derive constraints on the values of (a_2, b_2), as well as (a_3, b_3) when necessary, so that the method is positive and then show that the definitions of (a_2, b_2) given in Table 4.2 satisfy these constraints. We explicitly derive constraints on the values for the case where $U_4 \leq 0$ as this is the more complex case since (a_3, b_3) may not be zero. It can be easily verified that the same constraints are sufficient for (a_2, b_2) when $U_4 > 0$.

With the assumption that $U_1 \geq 0$, $U_2 \geq 0$, $U_3 \leq 0$ and $U_4 \leq 0$ we have that

$$\begin{aligned}
\bar{C}_1 &= C_1, \\
\bar{C}_2 &= (1-\omega_2)C_2 + \omega_2 C_1, \\
\bar{C}_3 &= (1-\omega_3)C_4 + \omega_3 C_1, \\
\bar{C}_4 &= C_1.
\end{aligned}$$

This leads to the flux expressions

$$\begin{aligned}
\mathcal{F}_1 &= U_1 C_1, \\
\mathcal{F}_2 &= [U_2\omega_2 + a_2(1-\omega_3) - b_2]C_1 + [U_2(1-\omega_2) + b_2]C_2 - [a_2(1-\omega_3)]C_4, \\
\mathcal{F}_3 &= [U_3\omega_3 - a_3(1-\omega_2) + b_3]C_1 + [a_3(1-\omega_2)]C_2 + [U_3(1-\omega_3) - b_3]C_4, \\
\mathcal{F}_4 &= U_4 C_4.
\end{aligned}$$

Recall that we can write the flux expression as $\mathcal{F}_k = \sum_{j=1}^{4} r_{k,j} C_j$, so that the update to subcell k is

$$\varphi_k = \mathcal{F}_k - \mathcal{F}_{k-1} = \sum_{j=1}^{4} (r_{k,j} - r_{k-1,j}) C_j = \sum_{j=1}^{4} \delta r_{k,j} C_j,$$

where we define $\delta r_{k,j} = r_{k,j} - r_{k-1,j}$. Hence the scheme is positive if $\delta r_{k,j} \leq 0$ for $k \neq j$. Now, $\delta r_{1,j}$, $j = 1, ..., 4$ do not depend on a_2, a_3, b_2 or b_3. Therefore, these terms need not be considered. In addition, the flux expressions do not depend on C_3. Hence, $\delta r_{k,3} = 0$ for all k. The remaining terms are given by

$$\begin{aligned}
\delta r_{2,1} &= U_2\omega_2 - U_1 + a_2(1-\omega_3) - b_2, \\
\delta r_{2,2} &= U_2(1-\omega_2) + b_2, \\
\delta r_{2,4} &= -a_2(1-\omega_3), \\
\delta r_{3,1} &= U_3\omega_3 - U_2\omega_2 - a_2(1-\omega_3) - a_3(1-\omega_2) + b_2 + b_3, \\
\delta r_{3,2} &= (a_3 - U_2)(1-\omega_2) - b_2, \\
\delta r_{3,4} &= (a_2 + U_3)(1-\omega_3) - b_3, \\
\delta r_{4,1} &= U_4 - U_3\omega_3 + a_3(1-\omega_2) - b_3, \\
\delta r_{4,2} &= -a_3(1-\omega_2), \\
\delta r_{4,4} &= -U_3(1-\omega_3) + b_3.
\end{aligned}$$

It can be verified that for the range of velocities that $(a_2, b_2) \neq (0,0)$ and/or $(a_3, b_3) \neq (0,0)$ that

$\delta r_{k,j}$ satisfy the conditions of positivity provided

$$0 \le a_2 \le \min(-U_3, U_1 - U_2\omega_2), \qquad 0 \le b_2 \le \min(U_1, U_2),$$
$$0 \le a_3 \le \min(U_2, -U_4 + U_3\omega_3), \qquad 0 \le b_3 \le \min(-U_4, -U_3).$$

As mentioned above it can be easily verified that the same constraints are sufficient for a_2 and b_2 when $U_4 \ge 0$ (in which case $(a_3, b_3) = (0, 0)$ according to Table 4.2).

Since the constraints are not coupled, we only need to show that these hold for (a_2, b_2). We do this in two parts $b_2 = 0$ ($0 \le \tilde{\theta}_2 \le \theta^*$) and separately $a_2 = 0$ ($\theta^* \le \tilde{\theta}_2 \le \frac{\pi}{2} - \theta^*$), see Table 4.2, which is possible since a_2 and b_2 cannot simultaneously be nonzero. For the remaining range, $\pi/2 - \theta^* \le \tilde{\theta}_2 \le \pi/2$, $(a_2, b_2) = (0, 0)$ so there is no affect on positivity. According to the definitions in the table $a_2 \ge 0$ and $b_2 \ge 0$ so the first inequality is satisfied for both cases.

As a reminder we restate several relevant definitions from the text

$$\tilde{\theta}_2 = \arctan(U_2/U_1), \qquad \tilde{U}_2 = 2/(1/U_1 - 1/U_3),$$
$$\tilde{V}_2 = \tilde{U}_2 \tan\tilde{\theta}_2, \qquad \tilde{\gamma}_2 = \sqrt{\tilde{U}_2^2 + \tilde{V}_2^2} = \tilde{U}_2\sqrt{1 + \tan^2\tilde{\theta}_2},$$
$$\theta^* = \arctan\left(\frac{3 - \sqrt{5}}{2}\right), \qquad \psi = \frac{1}{2}\left(|\cos\tilde{\theta} - \sin\tilde{\theta}|\sin\tilde{\theta}\cos\tilde{\theta}\right) \approx 0.1925.$$

1. $0 \le \tilde{\theta}_2 \le \theta^*$ hence $a_2 \ge 0$ and $b_2 = 0$:

   In this case given the definition of a_2, we have that

$$\begin{aligned} a_2 &= \tilde{\gamma}_2\left(\frac{\psi - \sin\tilde{\theta}_2\cos\tilde{\theta}_2|\cos\tilde{\theta}_2 - \sin\tilde{\theta}_2|}{\cos\tilde{\theta}_2(\cos\tilde{\theta}_2 - \sin\tilde{\theta}_2)}\right) \\ &\le \tilde{\gamma}_2\psi \\ &= \psi\tilde{U}_2\sqrt{1 + \tan^2\tilde{\theta}_2} \\ &\le 2\psi\min(U_1, -U_3)\sqrt{1 + \tan^2\tilde{\theta}_2} \\ &\le (1 - \tan\tilde{\theta}_2)\min(-U_3, U_1) \\ &\le \min(-U_3, U_1(1 - \tan\tilde{\theta}_2)) \\ &= \min(-U_3, U_1 - U_2) \\ &= \min(-U_3, U_1 - U_2\omega_2). \end{aligned}$$

   The first inequality is due to

$$\max_{0\le\varphi\le\theta^*}\left(\frac{\psi - \sin\varphi\cos\varphi|\cos\varphi - \sin\varphi|}{\cos\varphi(\cos\varphi - \sin\varphi)}\right) = \psi$$

and the second inequality follows the basic property of harmonic averages that

$$\tilde{U}_2 = \frac{2}{\frac{1}{U_1} - \frac{1}{U_3}} \leq 2\min(U_1, -U_3).$$

The final two inequalities are easily verified to hold over the range $0 \leq \tilde{\theta}_2 \leq \theta^*$, and $\omega_2 = 1$ in this range.

2. $\theta^* \leq \tilde{\theta}_2 \leq \frac{\pi}{2} - \theta^*$ hence $a_2 = 0$ and $b_2 \geq 0$:
In this case given the definition of b_2 we have that

$$\begin{aligned} b_2 &= \tilde{\gamma}_2 \left(\frac{\psi - \sin\tilde{\theta}_2 \cos\tilde{\theta}_2 |\sin\tilde{\theta}_2 - \cos\tilde{\theta}_2|}{2\sin\tilde{\theta}_2\cos\tilde{\theta}_2} \right) \\ &\leq 2U_1\sqrt{1+\tan^2\tilde{\theta}_2} \left(\frac{\psi - \sin\tilde{\theta}_2 \cos\tilde{\theta}_2 |\sin\tilde{\theta}_2 - \cos\tilde{\theta}_2|}{2\sin\tilde{\theta}_2\cos\tilde{\theta}_2} \right) \\ &\leq 2U_1\sqrt{1+\tan^2\tilde{\theta}_2}\psi \\ &\leq U_1 \min(1, \tan\tilde{\theta}) \\ &= \min(U_1, U_2). \end{aligned}$$

The first inequality is a result of the harmonic average definition of $\tilde{U}_2$ which implies that $\tilde{U}_2 \leq 2U_1$, and the last two can be verified over the range $\theta^* \leq \tilde{\theta} \leq \frac{\pi}{2} - \theta^*$.

Appendix B

Monotonicity of Multi-D Schemes for General Mobility Functions

For general mobility functions the upwind state C_i^* is defined as

$$\mathcal{F}_i^* = f_i(C_i^*) = \begin{cases} \max_{C_i \le c \le C_{i+1}} f_i(c), & \text{if } C_i \le C_{i+1} \\ \max_{C_{i+1} \le c \le C_i} f_i(c), & \text{if } C_i > C_{i+1} \end{cases},$$

with the property that

$$C_i^* = \begin{cases} C_i, & \text{if } f_i'(C_i^*) \ge 0 \\ C_{i+1}, & \text{if } f_i'(C_i^*) \le 0 \\ C_s, & \text{if } f_i'(C_i^*) = 0 \end{cases}.$$

The point C_s is a point such that $f_i'(C_s) = 0$. The multi-D mobility weighting is then defined as

$$\bar{\zeta}_i = \begin{cases} (1-\omega_i)\bar{\zeta}_i - \omega_i \bar{\zeta}_{i-1}, & \text{if } f_i'(C_i^*) > 0,\ f_{i+1}'(C_{i-1}^*) > 0 \\ (1-\omega_i)\bar{\zeta}_{i+1} - \omega_i \bar{\zeta}_{i+1}, & \text{if } f_i'(C_i^*) < 0,\ f_{i+1}'(C_{i+1}^*) < 0 \\ \bar{\zeta}(C_i^*), & \text{otherwise} \end{cases},$$

where ω_i^* is

$$\omega_i^* = \begin{cases} \max\left(0, \frac{\sigma_{i-1}}{\sigma_i}\right), & \text{if } f_i'(C_i^*) > 0,\ f_{i+1}'(C_{i-1}^*) > 0 \\ \max\left(0, \frac{\sigma_{i+1}}{\sigma_i}\right), & \text{if } f_i'(C_i^*) < 0,\ f_{i+1}'(C_{i+1}^*) < 0 \\ 0, & \text{otherwise} \end{cases}. \tag{B.1}$$

These mobility weightings can be rewritten in vector form as

$$\begin{aligned}\boldsymbol{A}\bar{\boldsymbol{\zeta}} &= \boldsymbol{B}\boldsymbol{\zeta} + \boldsymbol{B}_s\zeta(C_S),\\ \bar{\boldsymbol{\zeta}} &= \boldsymbol{A}^{-1}\boldsymbol{B}\boldsymbol{\zeta} + \boldsymbol{A}^{-1}\boldsymbol{B}_s\zeta(C_S)\\ &= \boldsymbol{R}\boldsymbol{\zeta} + \boldsymbol{R}_s\zeta(C_S),\end{aligned}$$

where $\boldsymbol{A}$ is an M-matrix and $\boldsymbol{B}$ as well as $\boldsymbol{B}_s$ are non-negative matrices. Hence $\boldsymbol{R}$ and $\boldsymbol{R}_s$ are non-negative stencil matrices.

We make the following assumptions:

- non-negative discrete masses, $C \geq 0$
- an interpolation, parameters $\omega = \omega(\omega^*)$ with ω^* defined by B.1 and $0 \leq \omega(\omega^*) \leq \min(1, \omega^*)$
- $\omega_l < 1$ for at least one $l \in \{1, 2, \ldots, n_{ir}\}$

We will check monotonicity for a subcell k and need to check the three analogous cases to those in Theorem 1: (1) $C_k^* = C_k$ and $C_{k-1}^* = C_k$, (2) $C_k^* = C_k$ and $C_{k-1}^* = C_{k-1}$, (3) $C_k^* = C_{k+1}$ and $C_{k-1}^* = C_{k-1}$. (4) $C_k^* = C_k$ and $C_{k-1}^* = C_s$, (5) $C_k^* = C_{k+1}$ and $C_{k-1}^* = C_s$.

1. $C_k^* = C_k$ and $C_{k-1}^* = C_k$:
   The accumulation term is

$$\begin{aligned}\varphi_k &= \bar{\mathcal{F}}_k - \bar{\mathcal{F}}_{k-1}\\ &= \sigma_k\zeta_k - \sigma_{k-1}\zeta_k.\end{aligned}$$

   Hence the derivative with respect to $C_{j\neq k}$ is

$$\frac{\partial\varphi_k}{\partial C_j} = 0.$$

2. $C_k^* = C_k$ and $C_{k-1}^* = C_{k-1}$:
   The accumulation term is

$$\begin{aligned}\varphi_k &= \bar{\mathcal{F}}_k - \bar{\mathcal{F}}_{k-1}\\ &= \sigma_k\bar{\zeta}_k - \sigma_{k-1}\bar{\zeta}_{k-1}\\ &= \sigma_k(1-\omega_k)\zeta_k - (\sigma_{k-1} - \sigma_k\omega_k)\bar{\zeta}_{k-1}\\ &= \sigma_k(1-\omega_k)\zeta_k - (\sigma_{k-1} - \sigma_k\omega_k)\sum_{j=1}^{n_{ir}} r_{k-1,j}\zeta_j.\end{aligned}$$

Taking the derivative of the accumulation term with respect to $C_{j\neq k}$ gives

$$\frac{\partial \varphi_k}{\partial C_j} = -(\sigma_{k-1} - \sigma_k \omega_k) r_{k-1,j} \zeta'(C_j).$$

The construction of the face mobilities means that for each j such that $r_{k-1,j} \neq 0$, $f'_j(C_j) = \sigma_j \zeta'(C_j) \geq 0$ and also $\text{sign}(\sigma_j) = \text{sign}(\sigma_{j+1})$. By the properties of ω_k it is easily shown that either

$$\text{sign}(\sigma_{k-1} - \sigma_k \omega_k) = \text{sign}(\sigma_k) \qquad \text{or} \qquad \sigma_{k-1} - \sigma_k \omega_k = 0.$$

This means that for each j such that $r_{k-1,j} \neq 0$

$$\text{sign}\left((\sigma_{k-1} - \sigma_k \omega_k) r_{k-1,j} \zeta'(C_j)\right) = \text{sign}\left(\sigma_{k-1} \zeta'(C_j)\right) = \text{sign}\left(\sigma_j \zeta'(C_j)\right).$$

Hence

$$(\sigma_{k-1} - \sigma_k \omega_k) r_{k-1,j} \zeta'(C_j) \geq 0$$

and $\frac{\partial \varphi_k}{\partial C_j} \leq 0$ for $j \neq k$.

3. $C^*_k = C_{k+1}$ and $C^*_{k-1} = C_{k-1}$:
   The accumulation term

$$\begin{aligned} \varphi_k &= \bar{\mathcal{F}}_k - \bar{\mathcal{F}}_{k-1} \\ &= \sigma_k \bar{\zeta}_k - \sigma_{k-1} \bar{\zeta}_{k-1} \\ &= \sum_{j=1}^{n_{ir}} (\sigma_k r_{k,j} - \sigma_{k-1} r_{k-1,j}) \zeta_j. \end{aligned}$$

   Taking the derivative with respect to $C_{j\neq k}$ gives

$$\frac{\partial \varphi_k}{\partial C_j} = (\sigma_k r_{k,j} - \sigma_{k-1} r_{k-1,j}) \zeta'(C_j).$$

   By similar arguments to those above, if $r_{k,j} \neq 0$ then $\sigma_k \zeta'(C_j) \leq 0$ and if $r_{k-1,j} \neq 0$ then $\sigma_{k-1} \zeta'(C_j) \geq 0$. Hence overall we have that $\frac{\partial \varphi_k}{\partial C_j} \leq 0$ for $j \neq k$.

4. $C^*_k = C_k$ and $C^*_{k-1} = C_s$:
   The accumulation term is

$$\begin{aligned} \varphi_k &= \bar{\mathcal{F}}_k - \bar{\mathcal{F}}_{k-1} \\ &= \sigma_k \zeta_k - \sigma_{k-1} \zeta(C_s) \end{aligned}$$

Hence the derivative with respect to $C_{j\neq k}$ is

$$\frac{\partial \varphi_k}{\partial C_{j\neq k}} = 0.$$

5. $C_k^* = C_{k+1}$ and $C_{k-1}^* = C_s$:
   The accumulation term is

$$\begin{aligned}\varphi_k &= \bar{\mathcal{F}}_k - \bar{\mathcal{F}}_{k-1} \\ &= \sum_{j=1}^{n_{ir}} \sigma_k r_{k,j} - \sigma_{k-1}\zeta(C_s).\end{aligned}$$

   Taking the derivative with respect to $C_{j\neq k}$ gives

$$\frac{\partial \varphi_k}{\partial C_j} = \sigma_k r_{k,j} \zeta'(C_j).$$

   By similar arguments to those above, if $r_{k,j} \neq 0$ then $\sigma_k \zeta'(C_j) \leq 0$. Hence overall we have that $\frac{\partial \varphi_k}{\partial C_j} \leq 0$ for $j \neq k$.

Appendix C

Lower Bound on the Mass Variables

In section 4.2 we assumed that we had a discretization of the form

$$C_{\alpha,i}^{n+1} = G_{\alpha,i}(\boldsymbol{C}_o^n, \boldsymbol{C}_w^n),$$

where $\boldsymbol{C}_\alpha^n$ is a vector of average mass values of phase α for the entire grid. Furthermore, we assumed that the discretization had the property that

$$\frac{\partial C_{\alpha,i}^{n+1}}{\partial C_{\alpha,j}^n} = \frac{\partial G_{\alpha,i}(\boldsymbol{C}_o, \boldsymbol{C}_w)}{\partial C_{\alpha,j}} \geq 0, \qquad \forall\ i, j,$$

where $0 \leq \boldsymbol{C}_\alpha \leq \boldsymbol{C}_\alpha^n$ ($\leq$ is computed pointwise). We now prove the claim that this property along with consistency leads to $C_{\alpha,i}^{n+1} \geq 0$ if $C_{\alpha,j}^n \geq 0$ for all j. For convenience we will prove this for $\alpha = w$ in the absence of source terms.

One of the implications of consistency of the discretization is that if $\boldsymbol{C}_w \equiv \boldsymbol{0}$ then $G_{w,i}(\boldsymbol{0}, \boldsymbol{C}_o^n) = 0$. We now define another *vector* function $\boldsymbol{C}_{w,j}^n(c)$ such that

$$\boldsymbol{C}_{w,j}^n(c) = \left(C_{w,1}^n,\ C_{w,2}^n,\ \cdots,\ C_{w,j-1}^n,\ c,\ 0,\ \cdots,\ 0\right)^T.$$

Now we can write the update as

$$\begin{aligned} C_{w,i}^{n+1} &= G_{w,i}(\boldsymbol{C}_w^n, \boldsymbol{C}_o^n) \\ &= \underbrace{G_{w,i}(\boldsymbol{0}, \boldsymbol{C}_o^n)}_{0} + \sum_{j=1}^{N} \left(\int_0^{C_{w,j}^n} \frac{\partial G_{w,i}\left(\boldsymbol{C}_{w,j}^n(c), \boldsymbol{C}_o^n\right)}{\partial C_{w,j}}\, dc \right). \end{aligned}$$

Now they quantities in the integrals are all non-negative by the monotonicity assumption, this implies that $C_{w,i}^{n+1} \geq 0$. The only complications that source terms adds to this argument is that if there is an injector in a cell then $G_{w,i}(\mathbf{0}, \boldsymbol{C}_o^n) \neq 0$ but some positive value.

Bibliography

J E. Aarnes. On the use of a mixed multiscale finite element method for greaterflexibility and increased speed or improved accuracy in reservoir simulation. *Multiscale Modeling and Simulation*, 2(3):421–439, 2004.

I. Aavatsmark. An introduction to multipoint flux approximations for quadrilateral grids. *Computational Geosciences*, 6(3-4):405–432, 2002.

J.R. Appleyard and I.M. Cheshire. The cascade method for accelerated convergence in implicit simulators. In *European Petroleum Conference*, pages 113–111, 1982.

K. Aziz and A. Settari. *Petroleum Reservoir Simulation*. Applied Science Publishers, 1979.

K. Aziz and T.W. Wong. Considerations in the development of multipurpose reservoir simulation models. In *proceedings of the 1st and 2nd International Forum on Reservoir Simulation, Alpbach, Austria, September 12-16, 1988 and September 4-8, 1989*, 1989.

M.J. Blunt and B. Rubin. Implicit flux-limiting schemes for petroleum reservoir simulation. In *2nd European Conference on the Mathematics of Oil Recovery*, pages 131–138, November 1990.

D.J. Bodony. Analysis of sponge zones for computational fluid dynamics. *Journal of Computational Physics*, 212(2):681–702, 2006.

C.W. Brand, J.E. Heinemann, and K. Aziz. The grid orientation effect in reservoir simulation. In *SPE Paper 21228 presented at the SPE Reservoir Simulation Symposium, Anaheim, California*, 17-20 February 1991.

Y. Brenier and J Jaffré. Upstream differencing for multiphase flow in reservoir simulation. *SIAM J. Numer. Anal.*, 28(3):685–696, 1991.

J. Caers. *Petroleum Geostatistics*. Society of Petroleum Engineers, 2005.

W.H. Chen, L.J. Durlofsky, B. Engquist, and S. Osher. Minimization of grid orientation effects through use of higher-order finite difference methods. *SPE Advanced Technology Series*, 1(2): 43–52, 1993.

Zhiming Chen and Thomas Y. Hou. A mixed multiscale finite element method for elliptic problems with oscillating coefficients. *Math. Comp*, 72(242):541–576, 2003.

M.A. Christie. Upscaling for reservoir simulation. *Journal of Petroleum Technology*, 48:1004–1110, 1996.

M.A. Christie, J. Glimm, J.W. Grove, D.M. Higdon, D.H. Sharp, and M.M. Wood-Schultz. Error analysis and simulations of complex phenomena. *Los Alamos Science*, 29:6–25, 2005.

M.A. Christie, V. Demyanov, and D. Erbas. Uncertainty quantification for porous media flows. *Journal of Computational Physics*, 217(1):143–158, 2006.

P. Colella. Multidimensional upwind methods for hyperbolic conservation laws. *Journal of Computational Physics*, 87(1):171–200, 1990.

A.T. Corey. The interrelation between gas and oil relative permeabilities. *Producers Monthly*, 19 (1):38–41, 1954.

M. G. Crandall and A. Majda. Monotone difference approximations for scalar conservation laws. *Mathematics of Computation*, 34:1–21, 1980.

H. Deconinck and B. Koren, editors. *Euler and Navier-Stokes Solvers Using Multi-Dimensional Upwind Schemes and Multigrid Acceleration*. Vieweg, 1997.

H. Deconinck, M. Ricchiuto, and K. Sermeus. Introduction to residual distribution schemes and comparison with stabilized finite elements. In H. Deconinck, editor, *33rd computational fluid dynamics - Novels Methods for solving convection dominated systems*. von Karman Institute for Fluid Dynamics, 2003.

C.V. Deutsch and A.G. Journel. *GSLIB: Geostatistical Software Library and Users Guide*. Oxford Univsity Press, 1998.

M.G. Edwards. Multi-dimensional wave-oriented upwind schemes with minimal cross-wind diffusion. In *SPE Paper 79689 presented at the SPE Reservoir Simulation Symposium, Houston, Texas*, 3-5 February 2004.

M.G. Edwards and C.F. Rogers. Finite volume discretization with imposed flux continuity for the general tensor pressure equation. *Computational Geosciences*, 2(4):259–290, 1998.

C.L. Farmer. Upscaling: A review. *International Journal for Numerical Methods in Fluids*, 40(1-2): 63–78, 2002.

M. Gerritsen and L. Durlofsky. Modeling fluid flow in oil reservoirs. *Annual Review of Fluid Mechanics*, 37:211–238, 2005.

B. Gustafsson. *High Order Difference Methods for Time Dependent PDE*. Springer, 2007.

Z.E. Heinemann, C.W. Brand, M. Munka, and Y.M. Chen. Modeling reservoir geometry with irregular grids. *SPE Reservoir Engineering*, 6(2):225–232, 1991.

C. Helzel, M.J. Berger, and R.J. LeVeque. A high-resolution rotated grid method for conservation laws with embedded geometries. *SIAM Journal on Scientific Computing*, 26(3):785–809, 2005.

T.Y. Hou and XH Wu. A multiscale finite element method for elliptic problems in composite materials and porous. *Journal of Computational Physics*, 134(1):169–189, 1997.

K. Jessen, M.G. Gerritsen, and B.T. Mallison. High-resolution prediction of enhanced condensate recovery processes. *SPE Journal*, 13(2):257–266, 2008.

B. Koren. Low-diffusion rotated upwind schemes, multigrid and defect corrections for steady, multi-dimensional euler flows. *International Series of Numerical Mathematics*, 98:265–276, 1991.

E.J. Koval. A method for predicting the performance of unstable miscible displacements in heterogeneous media. *SPE Journal*, 3:145–154, 1963.

S. Krishnamurthy. *Relaxation schemes for multiphase, multicomponent for in gas injection processes*. PhD thesis, Stanford University, Stanford, California, 2008.

F. Kwok and H. Tchelepi. Potential-based reduced newton algorithm for nonlinear multiphase flow in porous media. *Journal of Computational Physics*, 227(1):706–727, 2007.

L.W. Lake. *Enhanced Oil Recovery*. Prentice-Hall, Englewood Cliffs, NJ, 1989.

J.V. Lambers, M.G. Gerritsen, and D. Fragola. Multiphase, 3-d flow simulation with integrated upscaling, mpfa discretization, and adaptivity. In *SPE Paper 118983 presented at the SPE Reservoir Simulation Symposium, The Woodlands, Texas*, 2-4 February 2009.

S. Lamine and M.G. Edwards. Higher-dimensional wave oriented upwind convection schemes for flow in porous media on structured and unstructured grids. In *Advanced Computational Methods in Engineering*, May 2008.

R. J. LeVeque. Wave propagation algorithms for multidimensional hyperbolic systems. *Journal of Computational Physics*, 131(2):327–353, 1997.

R.J. LeVeque. *Finite Volume Methods for Hyperbolic Problems*. Cambridge Univsity Press, 1st. edition, 2003.

K. Liu, G. Subramanian, D.I. Dratler, J. Lebel, and J. Yerian. A general unstructured grid, EOS based, fully implicit thermal simulator for complex reservoir processes. In *SPE Paper 106073 presented at the SPE Reservoir Simulation Symposium, Houston, Texas*, 26-28 February 2007.

O. Mascarenhas and L.J. Durlofsky. Coarse scale simulation of horizontal wells in heterogeneous reservoirs. *Journal of petroleum science and engineering*, 25(3-4):135–147, 2000.

R. Mittal and G. Iaccarino. Immersed boundary methods. *Annual Review of Fluid Mechanics*, 37 (1):239–261, 2005.

A.H. Muggeridge, M. Cuypers, C. Bacquet, and J.W. Barker. Scale-up of well performance for reservoir flow simulation. *Petroleum Geoscience*, 8:133–139, 2002.

A. O'Sullivan and M. Christie. Simulation error models for improved reservoir prediction. *Reliability Engineering and System Safety*, 91(10-11):1382–1389, 2006.

A. O'Sullivan and M A. Christie. Error models for reducing history match bias. *Computational Geosciences*, 9(2-3):125–153, 2005.

T. Potempa. An improved implementation of the mccracken and yanosik nine point finite difference procedure. Technical Report 83-14, Rice University, 1983.

K. Pruess and G.S. Bodvarsson. A seven-point finite difference method for improved grid orientation performance in pattern steamfloods. In *SPE Paper 12252 presented at the SPE Reservoir Simulation Symposium, San Francisco, California*, 15-18 November 1983.

P. Renard and G. de Marsily. Calculating effective permeability: a review. *Advances in Water Resources*, 20:253–278, 1997.

A. Riaz and E. Meiburg. Linear stability of radial displacements in porous media: Influence of velocity-induced dispersion and concentration-dependent diffusion. *Phys. Fluids*, 16(10):3592, 2004.

G.E. Robertson and P.T. Woo. Grid-orientation effects and the use of orthogonal curvilinear coordinates in reservoir simulation. *SPE Journal*, 18(1):13–19, 1978.

P.L. Roe and D. Sidilkover. Optimum positive linear schemes for advection in two and three dimensions. *SIAM Journal of Numerical Analysis*, 29(6):1542–1568, 1992.

T.F. Russell and M. F. Wheeler. *The Mathematics of Reservoir Simulation*, volume 1 of *Frontier in Applied Mathematics*, chapter Finite Element and Finite Difference Methods for Continuous Flows in Porous Media, pages 35–106. SIAM, 1984.

P.H. Sammon. An analysis of upstream differencing. *SPE Reservoir Engineering*, 3(3):1053–1056, 1988.

P.S. Sarathi. In-situ combustion handbook - principles and practices. Technical report, Department of Energy, DOE/PC/91008-0374, 1999.

G.S. Shiralkar. Reservoir simulation of generally anisotropic system. *SPE Reservoir Engineering*, 5 (4):409–414, 1990.

G.R. Shubin and J.B. Bell. An analysis of the grid orientation effect in numerical simulation of miscible displacement. *Computer methods in applied mechanics and engineering*, 47(1-2):47–71, 1984.

J. C. Strikwerda. *Finite Difference Schemes and Partial Differential Equations*. SIAM, 2nd. edition, 2004.

C.T. Tan and G.M. Homsy. Stability of miscible displacements in porous media: Radial source flow. *Physics of Fluids*, 30(5):1239–1245, 1997.

M.R. Todd and W.J Longstaff. The development, testing and application of a numerical simulator for predicting miscible flood performance. *Trans. AIME*, 253:874–882, 1972.

M.R. Todd, P.M. ODell, and G.J. Hiraski. Methods for increased accuracy in numerical reservoir simulators. *SPE Journal*, 12(6):515–530, 1972.

P. Van Ransbeeck and Ch. Hirsch. A general analysis of 2d/3d multidimensional upwind convection schemes. In H. Deconinck and B. Koren, editors, *Euler and Navier-Stokes Solvers Using Multi-Dimensional Upwind Schemes and Multigrid Acceleration*. Vieweg, 1997.

XH Wen and J. J. Gmez-Hernndez. Upscaling hydraulic conductivities in heterogeneous media: An overview. *Journal of Hydrology*, 183(1-2):ix–xxxii, 1996.

D.S. Wolcott, H. Kazemi, and R.H. Dean. A practical method for minimizing the grid orientation effect in reservoir simulation. In *SPE Paper 36723 presented at the SPE Annual Technical Conference and Exhibition, Denver, Colorado*, 6-9 October 1996.

J.L. Yanosik and T.A. McCracken. A nine-point, finite difference reservoir simulator for realistic prediction of adverse mobility ratio displacements. *SPE Journal*, 19(4):253–262, 1979.

R.M. Younis, H.A Tchelepi, and K. Aziz. Adaptively-localized-continuation-newton: Reservoir simulation nonlinear solvers that converge all the time. In *SPE Paper 119147 presented at the SPE Reservoir Simulation Symposium, The Woodlands, Texas*, 2-4 February 2009.